Photoinduced Hole Transfer and Recombination Dynamics of a CdS Quantum Dot Sensitized Mononuclear Water Oxidation Catalyst

by

Orion Magruder Pearce

B.S., Beloit College, 2013

A thesis submitted to the

Faculty of the Graduate School of the

University of Colorado in partial fulfillment

of the requirement for the degree of

Doctor of Philosophy

Department of Chemistry and Biochemistry

2019

This thesis entitled:

Photoinduced Hole Transfer and Recombination Dynamics of a CdS Quantum Dot Sensitized Mononuclear Water Oxidation Catalyst

written by Orion Magruder Pearce

has been approved for the Department of Chemistry by:

_____

Niels Damrauer

_____

Garry Rumbles

Date _____

The final copy of this thesis has been examined by the signatories, and we find that both the content and the form meet acceptable presentation standards of scholarly work in the above mentioned discipline.

Pearce, Orion Magruder (Ph.D., Chemistry)

Photoinduced Hole Transfer and Recombination Dynamics of a CdS Quantum Dot Sensitized Mononuclear Water Oxidation Catalyst

Thesis directed by Associate Prof. Gordana Dukovic and Associate Prof. Niels Damrauer

Artificial photosynthesis represents a promising strategy to capture and store solar energy through the production of carbon neutral fuels. This process begins with absorption of a photon by a semiconductor creating an electron-hole pair which are then separated and used to drive reduction and oxidation reactions. CdS nanostructures are model light absorbers for studying these charge transfer reactions and have already demonstrated photoinduced electron transfer to drive a variety of reactions. However, there has been comparatively little progress in understanding how CdS nanostructures may be used to sensitize oxidation reactions such as water oxidation. To this end, we undertook a thorough study of the excited state charge transfer behavior of a model system consisting of a mononuclear Ru water oxidation catalyst attached to the surface of a CdS quantum dot. Through careful analysis of the electron and hole sensitive measurements, we were able to determine parameters relevant for successful water oxidation. The first part of this dissertation consists of a study on the rate and efficiency of hole transfer to the catalyst. By modelling time resolved and steady state emission data it was discovered that the catalyst strongly binds to the quantum dot and engages in rapid photoinduced-hole transfer. The efficiency of hole transfer is limited only by competition with the tendency of holes to localize to quantum dot surface trap states. The second part of this dissertation determines the fate of the electron and hole following hole trapping or transfer. The population of quantum dots that transferred holes was found to decay to the ground state over the course of nanoseconds, while hole trapping appears to facilitate electron transfer to the catalyst. The final part of this dissertation explores the binding between

quantum dot and catalyst using NMR spectroscopy. The two bind in a specific orientation which appears to facilitate hole transfer by provide a charge transfer pathway between the electronic states of the catalyst and quantum dot. This work establishes data analysis methods and design principles which may be leveraged in the development of future catalyst/quantum dot systems.

Acknowledgements

In the process of writing this dissertation I have had the pleasure of looking back over my time at the University of Colorado and recognizing the many people who have supported me during my development as a scientist. I've endeavored to make this text a smoothly flowing narrative leading from one idea to another, but the friends and family members who went on this journey with me know that progress was hardly straightforward. I am immensely thankful for the many people who have supported me through the many dead ends, wrong directions, and outright mistakes which I had to make to get to this point.

First, I would like to thank my advisors, Prof. Gordana Dukovic and Prof. Niels Damrauer. Gordana, thank you for providing a fruitful environment for research, and for taking care of the funding so that I was free to work on science; a Ph.D. using such a variety of techniques would not even be conceivable without you. Niels, thank you for listening when I needed to talk through research challenges and for your hands-on approach to problem-solving, even when you had a busy schedule. Thank you both for your guidance and patience, especially when I was most lost and frustrated with my data. I would also like to thank my undergraduate mentors, Prof. George Lisensky and Prof. Ranjan Roy for sparking my nascent enthusiasm for science and mathematics.

I have been fortunate to get to know many brilliant research group members and fellow scientists while working on this project. I am incredibly grateful for the contributions of Prof. Jeremiah Duncan, Dr. Richard Shoemaker, and Dr. Bimala Lama for their assistance is acquisition and interpretation of the NMR data described in Chapter 4. I would like to thank Dr. Hayden Hamby, Dr. Amanda Grennell, Dr. Steve Fatur, Sam Shepard, Steven Sartor, Dr. James Utterback, Jesse Ruzicka, and Leah Hall for many productive trips to the coffee shop and for tolerating my skepticism about your various research projects. I've had the pleasure to work in two groups with extremely talented people, and would like to thank Dr. Katherine Shinopoulos, Dr. Chi-Hung

Chuang, Dr. Yinggang Lu, Dr. Pornthip Tongying, Prof. Molly Wilker, Prof. Kyle Schnitzenbaumer, Dr. Kyureon Lee, Master Hiroko Nakao, Dr. Tais Labrador, Marta Sulima, Kristina Vrowenvelder, Shelby Beer, Nicholas Pogranichniy, Helena Keller, Lauren Pellows, Madison Jilek, and Benjamin Hohman from the Dukovic group and Dr. Dylan Arias, Dr. Karen Spettel, Dr. Jamie Snyder, Dr. Jessica Ramirez, Dr. Thomas Carey, Ryan Dill, Alex Gilligan, Ethan Miller, Nick Pompetti, and Robyn Sjovold from the Damrauer lab. Thank you to my friends Dr. Dylan Mori and Dr. Jasmine Wallas for your sympathy and support throughout our time together at the University of Colorado in Boulder.

Finally, I'd like to thank my family for your love and support throughout my research career. Thank you to my amazing wife Christina who tolerated my absence from home for so many days so that I could pursue my dream of one day being a professor. Thank you to my daughter Shea for being her wonderful, beautiful, joyous self; meeting you is the best thing that has ever happened to me. I'm grateful for my sister Ali for her help in trying times and for letting me and Christy get out of the house occasionally. Big shout out to Stefan Tschimben as well for all of the times he helped watch Shea while I was recovering from my broken ankle. An extra special thank you to my mom and dad for your support and for telling me that I could do anything I wanted to do.

I would also like to recognize the sources of funding which enabled me to perform this research. Thank you for funding from the University of Colorado, from NSF CAREER award (no. CHE-1151151), and from the U.S. Department of Education Graduate Assistantship in Areas of National Need program.

Contents

Chapter 1 Introduction 1

1.1. Motivation 1

1.2. Background 4

1.2.1. CdS Quantum Dots 4

1.2.2. Redox Co-Catalysts 5

1.2.3. Catalytically Relevant Parameters 8

1.3. Summary 9

Chapter 2 Ultrafast Hole Transfer from CdS Quantum Dots to a Water Oxidation Catalyst 11

2.1. Introduction 11

2.2. Materials and Methods 13

2.2.1. CdS QD Synthesis 13

2.2.2. Ligand Exchange 14

2.2.3. WOC Synthesis 15

2.2.4. Steady-State Spectroscopy 15

2.2.5. TA Spectroscopy 16

2.2.6. PL Upconversion. 17

2.3. Results and Discussion 18

2.3.1. Kinetic Analysis of Electron and Hole Dynamics 20

2.3.2. Construction of PL Quenching Model 27

2.3.3. Quantitative Analysis of Steady State PL 29

2.4. Conclusions 33

Chapter 3 The Hole Picture: A Comprehensive Description of Carrier Dynamics for Two CdS Quantum Dot/Water Oxidation Catalyst Systems 35

3.1. Introduction 35

3.2. Materials and Methods 36

3.2.1. CdS QD Synthesis and Characterization 36

3.2.2. Ruthenium Catalyst Synthesis and Characterization 37

3.2.3. Steady-State Spectroscopy (UV-Vis, PL, PLE) 37

3.2.4. Cyclic Voltammetry and Spectroelectrochemistry 38

3.2.5. Visible TA Spectroscopy 39

3.2.6. NIR TA Spectroscopy 39

3.2.7. PL Upconversion Spectroscopy 40

3.2.8. TCSPC and TRES Spectroscopy 40

3.3. Results and Discussion 41

3.3.1. Steady-State QD PL Quenching by Catalyst 1 44

3.3.2. TCSPC Kinetics of Catalyst 1 50

3.3.3. TA Spectra and Kinetics of CdS + Catalyst 1 52

3.3.4. Summary and Construction of Kinetic Model for CdS Catalyst 1/QD 56

3.3.5. Decay Pathways and Kinetics of Catalyst 2 64

3.3.6. TCSPC and TA Kinetics of Catalyst 2 67

3.3.7. Comparison of Systems and Final Remarks 73

3.4. Conclusions 75

Chapter 4 Binding Orientation of a Ruthenium Based Water Oxidation Catalyst on a CdS QD Surface Revealed through NMR Spectroscopy 77

4.1. Introduction 77

4.2. Materials and Methods 79

4.2.1. CdS QD Synthesis and Ligand exchange 79

4.2.2. Ruthenium Complex Synthesis 80

4.2.3. NMR Spectroscopy 80

4.3. Results and Discussion 81

4.3.1. Assignment of WOC NMR Peaks 82

4.3.2. Effects of Binding on WOC Chemical Shift and Relaxation Time 88

4.3.3. Determination of WOC Orientation and Implications for Catalysis 92

Chapter 5 Conclusions and Outlook 98

Chapter 6 Bibliography 100

List of Tables

Table 1 Fit parameters from multiexponential fits to TA and TCSPC kinetic data 57
Table 2 Catalyst Loadings and Lifetimes for Estimation of Energy Transfer Rate Constant 70
Table 3 Fit to TA Decay of 25:1 Catalyst 2 72
Table 4 Peak positions and T_2 lifetimes for WOC protons 88
Table 5 Comparison between calculated and measured linewidths for selected protons in QD/WOC mixture. 92

List of Figures

Figure 1.1 Three approaches to photoinduced water splitting. (a) Photovoltaic electrolysis, in which light is absorbed by a semiconductor photovoltaic material which separates charges and uses them to drive water splitting on submerged electrodes. (b) In photoelectrochemical cells light is absorbed by a submerged semiconductor or dye sensitized semiconductor. Oxidative catalysis is performed on the semiconductor surface while electrons are directed through a wire to a reductive electrode. (c) Homogeneous photocatalytic water splitting, in which light is absorbed by a dispersed semiconductor particle and both reductive and oxidative catalysis are performed on the particle surface. 3

Figure 1.2 Proposed catalytic mechanism for light-driven water oxidation in the QD/catalyst 1 system. The mechanistic steps for water oxidation are based upon the mechanism of a related catalyst driven by a chemical oxidant.[36] The first charge transfer step consists of several processes, outlined in red in this diagram. 7

Figure 1.3 Catalytically relevant processes studied in this work. Rapid and efficient hole transfer (gray arrow), rate of recombination (black arrow), and strong binding of the catalyst to the surface (blue arrow) are all important to catalytic performance in sequential charge transfer reactions. 8

Figure 2.1 Comparison of uncorrected, absorbance corrected, and short path length PL quenching data. © Copyright 2018 American Chemical Society. 16

Figure 2.2 Transient absorption kinetics of methanol with a 440 nm pump observed at 598 nm. Fitting this response gives an IRF full width at half maximum of 0.18 ps. © Copyright 2018 American Chemical Society. 17

Figure 2.3 (a) UV-Vis absorption spectra of CdS QDs (100 nM), catalyst (2 μM), and their mixture at a 20:1 WOC:QD ratio. (Inset) chemical structure of catalyst and TEM image of CdS QDs. (b) PL spectra of CdS QDs with increasing amounts of catalyst. © Copyright 2018 American Chemical Society. 20

Figure 2.4 PL Upconversion spectrum of 440 nm excited QDs collected using a spectrograph/CCD camera. The x-axis has been converted from detected wavelength to emission wavelength through subtraction of the energy of one photon from the fundamental (12500 cm^{-1}). The peaks seen here correspond to 4 features: upconversion of the pump beam generated as a fourth harmonic of the idler (1760 nm idler, 440 nm fourth harmonic), upconversion of the sum frequency of the fundamental and the signal (1467 nm signal, 518nm SFI), Raman scattering from the solvent (~507 nm), and emission from the nanocrystal (centered at 458, but attenuated by long pass filter and by the phase matching angle of the crystal). The nanocrystal spectrum was identified by taking a scan of pure solvent, and the crystal angle optimized to maximize this feature while minimizing pump related features. © Copyright 2018 American Chemical Society. 22

Figure 2.5 (a) PL and TA spectra of CdS QD with no added catalyst. (b) TA (454 nm) and PL kinetics (averaged across emission feature shown in Figure 2.4). These kinetics indicate that the

hole trapping is the limiting process for band edge emission, and occurs with a time constant of 0.21 ± 0.01 ps. © Copyright 2018 American Chemical Society. 23

Figure 2.6 (a) TA spectrum collected 1 ns after excitation. Inset: Broadband photoinduced absorption (PA) feature. (b) Comparison of PL upconversion decay kinetics of the CdS band edge emission compared to the rise of the PA feature in the TA spectra, averaged from 520-650 nm. Both kinetics are fit to exponentials convoluted with the IRF of their respective experiments (fits shown in dashed lines). © Copyright 2018 American Chemical Society. 24

Figure 2.7 (a) Comparison of electron and hole signals in the presence and absence of catalyst. The TA dynamics are unaffected by the presence of catalyst on this timescale, implying that the PL dynamics are entirely due to holes. The decrease in PL lifetime from 0.21 ± 0.01 ps to 0.18 ± 0.01 ps (fits to upconversion data are shown in the figure using solid lines) indicates that hole transfer to the catalyst is competitive with the hole trapping process. (b) TA kinetics of the bleach feature for the first 50 ps for 0:1 and 10:1 samples. The catalyst does induce a slight decay on this time window, possibly recombination following hole transfer to the catalyst as was previously hypothesized for the ethyl ester system.[35] We disregard this decay in our analysis as it is well separated in time from hole transfer. © Copyright 2018 American Chemical Society. .25

Figure 2.8 Distributions in fitted lifetime obtained through resampling of 0:1 and 7:1 WOC:QD mixtures. Histograms were generated from bootstrap Monte Carlo analysis of both data sets over 1000 different fits. Gaussian fits to the distributions established a peak of 0.21 ps at 0:1 and 0.18 ps at 7:1 with standard deviations of 0.01 ps for each. © Copyright 2018 American Chemical Society. 26

Figure 2.9 Fractional quenching of band-gap PL as a function of ratio of WOC to QD. The data is fit to (2.9) to measure both the competitive quenching and trapping efficiency and Langmuir binding equilibrium. © Copyright 2018 American Chemical Society. 30

Figure 3.1 TEM micrograph of CdS QDs. 37

Figure 3.2 (a) Band potentials of CdS QD and redox potentials of catalyst 1 and 2. (b) UV-Vis spectra of CdS QD and both catalysts. (c) PL spectra of CdS QD (0.07 μM), catalyst 1 (5 μM), and catalyst 2 (11 μM). The QD sample was excited at 360 nm, and catalysts 1 and 2 were excited at their respective MLCT maxima. 42

Figure 3.3 (a) Steady state PL quenching of CdS QD, by catalyst 1. The ratios indicated are catalyst 1:QD. The weak solvent background fluorescence has been subtracted from each PL scan. (b) Quenching of band edge and trap PL by catalyst 1 fit to a model accounting for catalyst binding and charge transfer efficiency. Quenching of the band edge emission was measured from (a) by spectrally fitting of the band edge emission feature, whereas quenching of the trap emission was directly determined by the intensity at 620 nm. 44

Figure 3.4 Hole trapping time constant measurement from PL upconversion, NIR TA, and TA of the broadband photoinduced absorption (PA) feature. All scans were obtained using a 440 nm excitation wavelength. PL upconversion kinetics were averaged across the observable emission feature (460-480 nm) and fit to a single exponential convoluted with the instrument response function (IRF). The PA feature was averaged from 550-700 and fit with an exponential rise convoluted with the IRF. The NIR TA feature was averaged from 1350-1450 and fit to a single exponential with a y-offset convoluted with the IRF. 49

Figure 3.5 (a) TRES of CdS QD showing shifting and narrowing occurring during decay. The spectra shown here were rebinned from linearly spaced time-points (26 ps/bin) to the times indicated in the legend and normalized to the peak. (b) Kinetics of the trap emission at 590 nm and 710 compared to the amplitude of a gaussian spectral global fit. 51

Figure 3.6 Kinetics of trap emission from samples containing QDs and a 25:1 ratio of catalyst 1/QD. Kinetics have been normalized to highlight their similarity at late times. The data are fit to multiexponential decay functions convoluted with the TCSPC IRF 52

Figure 3.7 (a) Oxidative spectroelectrochemistry of catalyst 1 in acetonitrile. Blue spectra are the initially acquired spectra and yellow are following over time following application of a 1.4 V potential vs NHE. (b) Reductive spectroelectrochemistry of catalyst 1. Blue spectra are the initially acquired spectra and yellow are following application of a -1.0 V potential vs NHE. (c) Difference spectra following reduction or oxidation, showing the relative change in absorbance features. 53

Figure 3.8 (a) TA spectra of CdS QD and 25:1 catalyst 1/QD in two time windows. The picosecond spectra are averaged from 10 to 20 ps while the nanosecond spectrum was taken by averaging TA spectra from 20 to 500 ns. Inset: Zoom-in view of (a), showing the changes in the region of the catalyst MLCT absorption. (b) TA kinetics of the QD bleach showing faster decay upon addition of catalyst 1. All kinetics were taken at 456 nm. 54

Figure 3.9 Rise of the TA signal of the reduced catalyst (averaged from 540-660 nm) and decay of the band edge electron signal (456 nm) 56

Figure 3.10 TCSPC (710 nm), smoothed TCSPC data, and TA kinetics (456 nm) of CdS QDs, normalized to highlight the similarity of the decay at late times 57

Figure 3.11 (a) Decay of the TA signal of the reduced catalyst through trapped-hole diffusion-limited recombination. TA kinetics were averaged from 550-570 nm to isolate the reduced catalyst decay (see Figure 3.8). The fit to the data uses a multiexponential model for diffusion limited recombination derived below. (b) Illustration of coordinate system used in the derivation of a model of the recombination kinetics of a stationary reduced catalyst with a mobile trapped hole. 61

Figure 3.12: Kinetic scheme for the decay of catalyst 1/QD mixture. The arrows (in descending order by associated constant) indicate hole trapping, valence band hole transfer to catalyst 1, recombination of the transferred hole, electron transfer to catalyst 1, trapped hole recombination, and trapped-hole diffusional recombination with a reduced catalyst. The width of the arrows indicate the efficiency of each process for high-loading conditions. Angled brackets indicate an average rate constant. 63

Figure 3.13 (a) Steady state PL quenching of CdS QD, by catalyst 2. The ratios indicated are catalyst2:QD. (b) Quenching of band edge and Trap PL by catalyst 2 fit to the model used in fitting of Figure 3.3 64

Figure 3.14 (a) Emission scans of QD, catalyst 2, and their mixture when exciting at 2 different wavelengths. (b) UV-Vis and PLE scans of QD, catalyst 2, and a 5:1 mixture. The PLE scans were achieved through global fitting of a 2D excitation/emission scan using the emission spectra of QD and catalyst 2 shown in the left frame. PLE were converted to a logarithmic y-scale before being normalized. 65

Figure 3.15 (a) TCSPC decay of the trap emission of QD and 20:1 catalyst 2/QD mixture measured at 710 nm. (b) TRES of these samples averaged from 45 to 55 ns. Due to energy transfer, the emission of the Catalyst 2/QD mixture resembles emission from the catalyst rather than the nanocrystal. 67

Figure 3.16: Decay kinetics of directly photoexcited catalyst 2, as measured by TA and TCSPC. TA kinetics were measured at the MLCT maximum (496 nm) following excitation at 400 nm. TCSPC was measured exciting with a 402 nm excitation source and observing emission at 720 nm with a 32 nm monochromator bandpass and a 420 nm longpass filter to remove scattered excitation light. 68

Figure 3.17 (a) Late time emission kinetics for different mixing ratios with catalyst 2 showing quenching on a nanosecond timescale. (b) Lifetime quenching as a function of number of bound catalyst 2 per nanocrystal for the data shown in (a), and a fit to the quenching model derived below. 69

Figure 3.18 (a) TA spectra of CdS QD and 25:1 catalyst 2/QD solution averaged from 10 to 20 ps. Inset: Zoom-in view of (a), showing the changes in the region of the catalyst 2 MLCT absorption. (b) Kinetics of TA samples from (a) taken at 456 nm. The 25:1 sample was fit using the kinetics of the QDs combined with a biexponential fit. 71

Figure 3.19 Kinetic scheme for the decay of catalyst 2/QD mixture. The arrows (in decending order by rate constant) indicate hole trapping, valence band hole transfer to catalyst 2, recombination of the transferred hole, recombination across the MLCT state of catalyst 2, trapped hole recombination, and energy transfer to catalyst 2. The width of the arrows indicate the efficiency of each process for high-loading conditions. Angled brackets indicate an average rate constant. 73

Figure 4.1 (a) TEM micrograph of CdS QDs. (b) UV-Visible absorption spectra of CdS QDs... 79

Figure 4.2 ^{1}H NMR spectrum of CdS QD with a 3-MPA surface in MeOD. This spectrum exhibits peaks characteristic of bound and free 3-MPA, as well as solvent peaks, TMA counterion peaks, and an aliphatic impurity from synthesis. This spectrum was acquired on a 300 MHz NMR spectrometer. 82

Figure 4.3 ^{1}H NMR spectrum of the WOC. These data were acquired on a 300 MHz NMR spectrometer. 83

Figure 4.4 COSY of the WOC in acetone-d6. 84

Figure 4.5 HSQC spectra of the WOC in acetone-d6. 85

Figure 4.6 HMBC Spectrum of the WOC in acetone-d6. The highlighted peaks are correlations between protons c, d, and f with carbons 2 and 2″ in terpyridine. 85

Figure 4.7 NMR spectra of the aromatic region of the WOC with and without QD added. 86

Figure 4.8 TOCSY of 10:1 WOC/QDs in MeOD. Diagonal and cross-peaks were color coded based upon their correlations, with peaks belonging to the terpyridine highlighted in green and brown and peaks from the bipyridine in blue and teal. Based upon the similar COSY of the WOC shown in Figure 4.4, we have assigned each NMR peak of the mixed QD/WOC system to a proton. 87

Figure 4.9 Assignments of proton resonances in the ^{1}H NMR spectrum of WOC + QDs based on analysis of the TOCSY spectrum shown in Figure 4.8. Lines between the spectra indicate the change in chemical shift upon addition of the QDs. 88

Figure 4.10 Procedure for measurement of T_2 using spin echo, as viewed from the rotating frame, based on similar illustrations from Carr et al.[129] (a) Prior to excitation, the ensemble of spins produces a net magnetization, M_0, aligned with the external magnetic field. (b) An RF pulse tips the net magnetization into the x-y plane. (c) Due to inhomogeneities in the magnetic field, some protons precess faster or slower than the central frequency. Simultaneously, homogeneous T_2 shortening leads to irreversible loss of phase information and attenuation of all magnetization components. These two effects are allowed to occur for a fixed delay. (d) An RF pulse is used to tip the overall magnetization by 180°. (e) A delay of equal duration to the one used in (c) is allowed. During this time, the protons with difference B_{eff} experience an equal and opposite phase shift to the phase shift accrued during the previous delay, leading to recoherence. As occurred during (c), homogeneous T_2 relaxation irreversibly removes magnetization. (f) After recoherence the FID is acquired, and the resonance integrated to measure the homogeneously lost magnetization as a function of delay time. 90

Figure 4.11 (a) T_2 relaxation lifetime of each peak in the proton NMR of a WOC/QD solution. The terpyridine resonances (green highlight) tend to have shorter T_2 lifetimes than the dmcbpy resonances (blue highlight). (b) The correlation in absolute change in chemical shift with relaxation rate (T_2^{-1}). 91

Figure 4.12 (a) Effect of WOC terpyridine and QD surface angle on the distance between dmcbpy protons and QD surface. The orientation shown on the left leads to an equal distance from the QD for both rings of the dmcbpy, while the orientation on the right places one side of the dmcbpy significantly closer to the surface. (b) Visualization of the change in chemical shift and T_2 lifetime of protons in the WOC. Proton radius indicates the absolute change in chemical shift or T_2 lifetime. The catalyst is oriented to provide uniform trends in T_2 and absolute change in shift with distance from the nanocrystal surface. Proton coordinates are based on a related catalyst.[38] 94

Copyright

Chapter 1 Introduction

1.1. Motivation

Understanding and mitigating the effects of anthropogenic climate change is a vitally important area of scientific investigation. The negative effects of climate change are already occurring and will continue to worsen without drastic efforts to curb emissions of greenhouse gases (GHGs) such as CO_2.[1-2] A promising strategy to reduce GHG emissions is to replace the existing energy infrastructure based on fossil fuel combustion with new infrastructure based on solar energy. Solar energy harvests photons produced by the sun, which deliver enough energy to the earth's surface every two hours to meet humanity's energy needs for an entire year.[3] One strategy to capture and store this energy is through artificial photosynthesis, in which the energy of solar photons is captured and stored in chemical bonds.[1, 3] There are a number of targets for artificial photosynthesis including water splitting to form hydrogen fuel, fixation of carbon dioxide to produce liquid fuels and decrease atmospheric CO_2, and solar N_2 reduction to replace the energy intensive Haber-Bosch process.[1, 4-6] Advancements in artificial photosynthesis of these products could be directly applied to mitigate or prevent the effects of climate change.

Artificial photosynthetic reactions utilize redox chemistry at semiconductor interfaces to store photon energy in chemical potential. This process involves three steps: absorption of a solar photon to generate an electron-hole pair, separation and transport of charges to reaction centers, and use of the electron and hole to drive reductive and oxidative chemical reactions. For most reactions several charges must accumulate in order to complete a catalytic cycle. Both reductive and oxidative half-reactions are crucial for photocatalytic success, as buildup of charges leads to

bleaching of the light absorber and possible damage from unwanted side reactions.[6-7] In natural photosynthesis holes are removed by the oxidation of water.[8-9] The half reaction for this process is

$$2H_2O + 4\,h^+ \rightarrow 4H^+ + O_2$$

which consumes four holes per reaction. Water oxidation represents a highly desirable oxidation reaction for artificial photosynthesis owing to the low cost and high abundance of water.

Use of the water oxidation reaction as a terminal hole acceptor is as challenging as it is desirable. For each water molecule produced, four holes must be sequentially transferred to a single catalytic site. The coulombic repulsion which must be overcome to concentrate multiple charges into a single molecule creates activation barriers which limit reaction efficiency.[1, 9] These barriers are reduced through the use of water oxidation catalysts (WOCs) which stabilize the high energy intermediates produced during water oxidation. In nature, the catalyst used for this process is photosystem II, an enzyme with a tetramanganese cluster active site.[10] It was originally believed active sites containing multiple metal centers were essential to stabilize the charged intermediates involved in water oxidation, but it was later shown that single metal sites in coordination complexes were also catalytically active for water oxidation.[11-12] More recent developments in WOCs have allowed electrochemical water oxidation to be performed nearer to the thermodynamic potential and at higher turnover rates, even approaching the activity of photosystem II.[12-13] However, these systems have been primarily studied under chemical or electrochemical oxidation conditions and must be adapted to a photoelectrochemical reaction scheme.[14]

There exist several strategies to incorporate water splitting[6] into artificial photosynthesis, each with advantages and drawbacks. In photovoltaic driven electrolysis, light is absorbed by a

semiconductor photovoltaic material which separates charges and uses them to drive water splitting on electrodes in solution (Figure 1.1a). Photoelectrochemical cells modify this by submerging the light absorbing element and performing oxidative catalysis on its surface as shown in Figure 1.1b. Electrons are removed from the system through a wire and used to drive reductive reactions at a counter electrode. To further simplify the both reductive and oxidative catalysis can be performed directly on the surface of dispersed semiconductor particles (Figure 1.1c). This approach has certain practical advantages, as such particles could be simply scattered into a pool of sunlit water and begin producing hydrogen.[15] This simpler system is also ideal for studying the process of charge transfer at semiconductor interfaces and may lead to useful insights for other water-splitting geometries. In this dissertation we focus on CdS nanostructures, which are excellent model light absorbers for homogeneous photocatalytic water splitting.

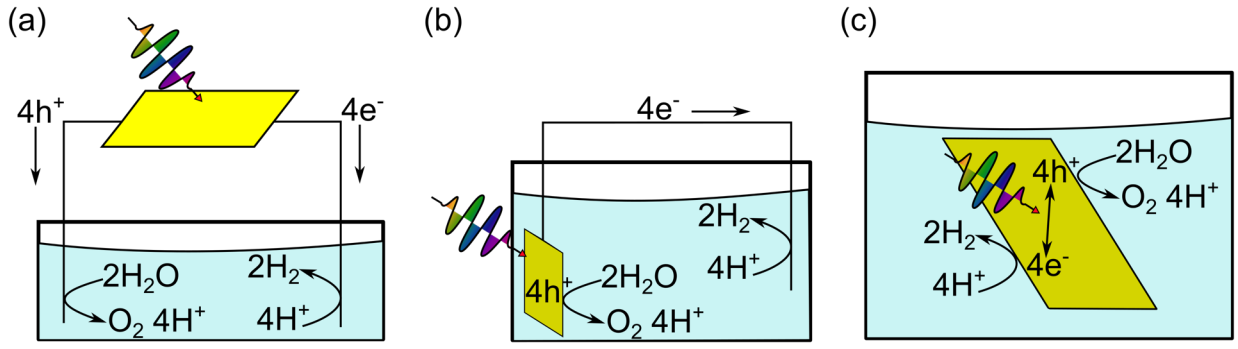

Figure 1.1 Three approaches to photoinduced water splitting. (a) Photovoltaic electrolysis, in which light is absorbed by a semiconductor photovoltaic material which separates charges and uses them to drive water splitting on submerged electrodes. (b) In photoelectrochemical cells light is absorbed by a submerged semiconductor or dye sensitized semiconductor. Oxidative catalysis is performed on the semiconductor surface while electrons are directed through a wire to a reductive electrode. (c) Homogeneous photocatalytic water splitting, in which light is absorbed by a dispersed semiconductor particle and both reductive and oxidative catalysis are performed on the particle surface.

1.2. Background

1.2.1. CdS Quantum Dots

The light absorber utilized in this work is a CdS quantum dot (QD) which is a type of quantum-confined semiconductor nanocrystal (NC). Quantum confinement is a perturbation of the electronic structure of semiconductors by confining the charge carriers into a limited volume.[16-17] Localization of the charge carriers within a small semiconductor particle leads to an increase in the energy of both electron in hole, similarly to the quantum mechanical "particle in a box".[18] This has a number of effects on the charge carriers, such as increased electron affinity and ionization potential as well as higher surface density of the carriers.[16] Quantum confinement has been demonstrated in structures of different morphologies, including semiconductor spheres (QDs) and nanorods (NRs).[17]

NCs have a number of benefits for studies in artificial photosynthesis. They are potent light absorbers with molar absorptivities ranging from $10^5 – 10^7$ $M^{-1}cm^{-1}$.[7] The small size of NCs results in high surface to volume ratios, facilitating charge transfer to surface bound species. The quantum confinement effect also leads to a significant surface density of the wavefunction which improves electronic coupling for charge transfer.[7, 16] The surface chemistry of these particles can be easily adjusted by substitution of the bound surfactant molecules, to tailor the polarity of the surface and interaction with molecular species.[7, 19] CdS nanocrystals are particularly attractive for solar fuel applications as they have valence and conduction band potentials well positioned to drive both proton reduction and water oxidation,[20] although special care must be taken to avoid oxidation of the sulfur lattice sites under water splitting conditions.[20-21]

1.2.2. Redox Co-Catalysts

Although NCs meet the energetic requirements to drive photocatalysis, the process is most efficient when NCs are coupled to co-catalysts.[7] Co-catalysts act to reduce the energy barriers of redox reactions, which are manifested as overpotentials in electrochemical catalysis.[1, 22] A variety of co-catalysts have shown success in reductive photocatalysis when sensitized by NCs and in the presence of sacrificial scavengers to remove holes. Catalysts based on noble metal particles and metal complexes attached to NC surfaces have exhibited efficient photoinduced H_2 production.[23-25] Enzymes have also been shown to be effective co-catalysts for many reactions including H_2 production, CO production, nicotinamide cofactor reduction, and N_2 reduction.[5, 26-31] There have also been a small number studies demonstrating photocatalytic water oxidation with CdS NC sensitizers.[32-34] These reports have demonstrated the feasibility of water oxidation using CdS as a light absorber but have also highlighted problems due to extremely slow catalytic oxygen production and sacrificial oxidation of lattice sulfides and surface ligands.[21] Addressing these issues will require a detailed study of the individual steps of photocatalytic water oxidation.

Prior work from Damrauer and Dukovic groups had demonstrated the potential for photoinduced charge transfer from CdS NRs to a WOC [Ru(deeb)(tpy)Cl]PF_6 (deeb = diethyl 2,2′-bipyridine-4,4′-dicarboxylate, tpy = 2,2′:6′,2″-terpyridine) upon mixing of the two chemicals in methanol.[35] The observations of photoluminescence quenching and shortened electron lifetimes suggested that the catalyst associated with the nanocrystal surface and altered the carrier dynamics of the CdS NRs.[35] However, the system suffered from colloidal stability issues, and it was later discovered that the catalyst partially transesterified in methanol over time.

To expand upon these initial findings, we modified this previously studied system by substituting the WOC for [Ru(dmcbpy)(tpy)Cl]PF_6 (dmcbpy =4,4′-dimethylcarboxylate-2,2′-

bipyridine), hereafter referred to as catalyst 1, to improve stability in methanol. We also used CdS QDs in place of NRs due to their superior colloidal stability in methanol. We propose a catalytic cycle for our system in Figure 1.2, based upon the mechanism determined for mononuclear WOCs similar to catalyst 1.[36] The initial state of the catalyst considered here contains a Ru^{II} center and bound aqua ligand. Although the catalyst used in this work initially has a bound chloro ligand rather than an aqua ligand, it has been shown that the chloro ligand is quickly displaced in the presence of water.[37] Each catalytic step begins with the photoexcitation of the QD and scavenging of the electron to generate a photoexcited hole. In the first step of the cycle, a proton-coupled hole transfer oxidizes catalyst 1 from Ru^{II} to Ru^{III} This process is then repeated to produce a Ru^{IV} center with the loss of another proton. Following this, two steps occur involving another photoinduced hole transfer, the formation of an oxygen-oxygen single bond, and the removal of another hydrogen. These are depicted in Figure 1.2 as distinct kinetic events although the exact process is still a matter of debate.[38] A final proton-coupled hole transfer produces a bound superoxide species (O_2^{2-}) on a Ru^{IV} center. This bound oxygen is oxidatively cleaved by coordination of a new aqua ligand, restoring the initial Ru^{II} catalyst.

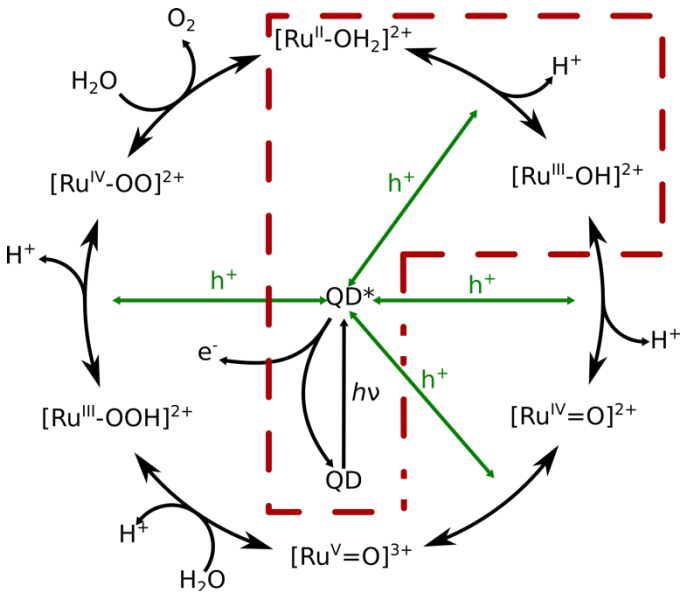

Figure 1.2 Proposed catalytic mechanism for light-driven water oxidation in the QD/catalyst 1 system. The mechanistic steps for water oxidation are based upon the mechanism of a related catalyst driven by a chemical oxidant.[36] The first charge transfer step consists of several processes, outlined in red in this diagram.

Replacing the chemical oxidants used in the original determination of this mechanism with photochemical oxidation introduces additional complications in the catalytic cycle. Photoexcited electron-hole pairs undergo a number of photophysical processes within the QD, such as cooling of hot carriers to the band gap energy, charge trapping to surface sites, and excited state decay through charge recombination.[39] Each of these represents an energy-loss pathway within the system. These losses can be avoided if photochemical processes such as hole transfer and electron scavenging are accomplished before energy loss through photophysical mechanisms can occur. By understanding the rates of both photoinduced hole transfer and excited state relaxation, we hope to gain insights into the fundamental limits of charge transfer efficiency.

To lay a foundation on which to study photocatalytic hole transfer, focus on several key processes involved in the first step of the catalytic cycle. The first of these processes is hole transfer to the catalyst. Following hole transfer, it is essential to know the timescale of electron-hole recombination, as this sets the time window for electron scavenging or reductive catalysis to

prevent energy loss through backwards reactions. The final parameter under investigation is the binding between the nanocrystal and catalyst, as charge transfer was hypothesized to occur to surface bound catalysts.

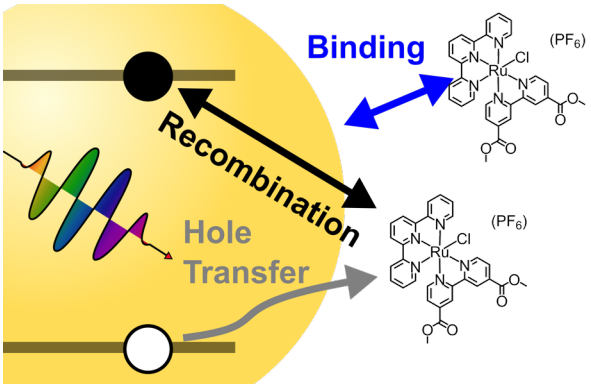

Figure 1.3 Catalytically relevant processes studied in this work. Rapid and efficient hole transfer (gray arrow), rate of recombination (black arrow), and strong binding of the catalyst to the surface (blue arrow) are all important to catalytic performance in sequential charge transfer reactions.

1.2.3. Catalytically Relevant Parameters

The rate and efficiency of hole transfer are the upper limits on the rate and efficiency of the overall catalytic reaction. These two are related, as faster hole transfer competes more efficiently with energy loss pathways. By measuring both, information can also be obtained about the nature of the competing processes. In the prior work with the ethyl-ester catalyst, hole transfer was initially estimated as occurring in 0.1 – 1 ns following photoexcitation, although this measurement was made through indirect observations of the hole. In our work described in Chapter 2, we found that hole transfer in our system was very fast, occurring on a picosecond timescale. We also determined that the efficiency of hole transfer was limited by the sub-picosecond hole trapping process which occurs in CdS NCs.[40]

The processes which occur following hole transfer are of equal importance to study, especially the decay of the transferred hole to the ground state. If the system is to undergo catalytic turnover, it is crucial to know the rate of this backwards process, as this sets the rate at which

electrons must be removed from the system. In the ethyl-ester catalyst the electron was shown to decay on the timescale of 10 – 100 ns, although the mechanism of this decay was not clear from the existing data.[35] The work in Chapter 3, describing the characterization of the kinetic pathways that occur following excitation, shows that the transferred hole recombination occurs on a 10 ns timescale as part of a complete characterization of the kinetic pathways which occur following excitation.

In Chapter 2, we found that the binding interaction between catalyst and QD was essential to the initial hole transfer process, as hole transfer was occurring to surface-bound catalysts. The experiments in Chapter 2 as well as prior work with the ethyl-ester catalyst had found that the equilibrium between bound and unbound catalysts strongly favored the bound form of the catalyst.[35, 41] The rapid rate of charge transfer also implied strong electronic communication between charge acceptor and donor, although the source of this coupling was unclear. The catalyst 1/QD binding was further explored in Chapter 4, wherein NMR spectroscopy revealed that the catalyst bound to the QD surface with a preferred orientation. This additional information on catalyst binding improves our understanding of the mechanism of hole transfer this system, as well as suggesting design principles to engineer electronic coupling in future catalyst/nanocrystal systems.

1.3. Summary

Achieving efficient water oxidation with semiconductor NC sensitizers is a crucial step to unlocking their potential for artificial photosynthesis. The challenges involved are substantial due to the mechanistic complexity of the water oxidation reaction. Although the recombination and trapping pathways are known in these systems, the importance of each is poorly understood without a quantitative framework in which to evaluate them. Foundational work to quantify charge

separation and recombination in well behaved model systems is required to isolate the factors relevant for effective photooxidative catalysis.

The primary goal of this research is to investigate the photoinduced charge transfer and binding interactions which take place in our WOC/QD model system. Chapter 2 is based on a 2018 publication in the Journal of Physical Chemistry C and characterizes the rate constant for hole transfer from the nanocrystal to surface bound catalysts, finding that hole transfer occurs quickly from the valence band to the WOC but that this process is limited by trapping of the holes to the QD surface. Chapter 3 determines the processes which occur following either hole transfer to the WOC or hole trapping. A related catalyst is investigated to build a case for the effects of catalyst energetics on charge transfer behavior. Chapter 4 focuses on use of NMR spectroscopy to determine the orientation the catalyst takes when binding to the NC, and how this orientation may inform our understanding of the charge transfer processes. By understanding the hole transfer characteristics of this WOC/QD system we elucidated the factors influencing charge transfer and recombination in this system, as well as identified key design principles for improvement of charge transfer rate and efficiency in future water oxidation systems.

Chapter 2 Ultrafast Hole Transfer from CdS Quantum Dots to a Water Oxidation Catalyst[†]

2.1. Introduction

Semiconductor nanocrystals have the potential to excel as light absorbers for photochemical transformations due to their strong absorptivity and tunable energy levels arising from size-dependent quantum confinement effects. CdS, in particular, has favorable bulk band potentials for oxidative and reductive half reactions such as water oxidation and proton reduction. Furthermore, facile modifications of surface chemistry enable coupling of colloidal CdS nanocrystals with a variety of redox catalysts, including nanoscale heterogeneous catalysts,[23, 32] inorganic complexes,[42-43] and enzymes.[5, 26] A number of studies have characterized the excited state dynamics in systems that use CdS nanocrystals to drive reductive photochemistry using reduction co-catalysts and sacrificial hole acceptors.[24, 44-47] In those systems, removal of photoexcited holes is crucial for supplying electrons, limiting recombination, and preventing photocorrosion.[45, 48-50] Ideally, hole scavenging would be non-sacrificial with use of water oxidation catalysts such that the rate of product (fuel) formation is only dependent on photon flux. However, our understanding of the dynamics of oxidative processes involving CdS nanocrystals is limited.[45, 51-52] In contrast to the variety of systems that couple these nanostructures to multi-electron reduction catalysts, there are remarkably few systems that transfer photoexcited holes from CdS nanocrystals to water oxidation catalysts (WOCs).[32, 35, 53] The discrepancy between progress in reductive and oxidative multi-electron photochemistry can be attributed to challenges

[†] Adapted from Pearce, O. M.; Duncan, J. S.; Damrauer, N. H.; Dukovic, G., Ultrafast Hole Transfer from CdS Quantum Dots to a Water Oxidation Catalyst. *J. Phys. Chem. C* **2018,** *122*, 17559-17565. (© Copyright 2018 American Chemical Society)

associated with observing hole populations using ultrafast spectroscopic techniques,[54-55] the tendency of photoexcited holes to trap on CdS nanocrystal surfaces complicating hole dynamics[56-57] and in the specific case of water oxidation, the mechanistic complexity of the catalysis.[9, 58-60]

Transfer of a photoexcited hole from a CdS nanocrystal to a WOC is the first step required for the multi-electron water oxidation reaction and the efficiency of that step defines the upper limit on the performance of the system. While dynamics associated with photoexcited electrons in CdS nanocrystals can be monitored with strong bleach signals in visible transient absorption (TA) spectra, those of photoexcited holes are harder to observe directly as they lack sharp and distinct spectral signatures.[39, 61] Previously, our group reported on coupling of CdS nanorods to a molecular WOC and described indirect estimates of dynamics of hole transfer from CdS nanocrystals to a WOC using the delayed onset of electron transfer to the catalyst as a proxy for the hole transfer that occurs before it.[35] This estimate placed the hole transfer lifetime on the timescale of 100 ps, but this value combined the dynamics of both the valence band and trapped holes. A measurement of the rate constant and efficiency of hole transfer from a CdS nanocrystal to a molecular WOC has not been reported to date.

In this letter, we report the *direct* measurement of valence band hole transfer kinetics from a CdS quantum dot (QD) to a ruthenium-based WOC. To probe valence band holes and deconvolute their kinetics from those of photoexcited electrons, we combine hole-sensitive photoluminescence (PL) upconversion with electron-sensitive TA spectroscopy, both of which have sub-picosecond time resolution. We then analyze the quenching of the QD PL by developing a model that takes into account both the nanocrystal-WOC binding interaction and kinetic competition with carrier trapping, which allows us to determine the rate constant for hole transfer, the equilibrium constant for nanocrystal-catalyst binding, and the maximum number of catalyst

binding sites. Together, the measurements and their analysis reveal design principles to improve the efficiency of valence band hole transfer and approach turnover conditions.

2.2. Materials and Methods

2.2.1. CdS QD Synthesis

We synthesized and purified CdS QDs following the method of Peterson et al.[62] All steps were performed under an inert argon atmosphere using standard Schlenk line or glovebox techniques. Prior to use, 1-octadecene (ODE; Sigma Aldrich, 90%) was evacuated at 90 °C in the reaction flask. A 0.10 M sulfur solution was prepared in 1-octadecene (ODE; Sigma Aldrich, 90%) several hours ahead of time (typical amounts: 0.028 g S_8, 7.11 g ODE). A 0.10 M solution of cadmium oleate was produced by heating 0.128 g of CdO, 6.85 mL of ODE, and 3.2 mL of oleic acid (OA; Sigma Aldrich, 90%) to 250 °C in a 3-neck round-bottom flask fitted with a reflux condenser. Once the solution turned clear, the heat source was removed, and the solution was allowed to cool to 60 °C. A second 3-neck flask was fitted with reflux condenser and charged with 3 mL of ODE. After evacuation, this solution was heated to 260 °C, 1 mL of 0.10 M sulfur solution was injected, and the solution was allowed to cool to 220 °C. After 3 min, 0.5 mL of 0.10 M cadmium oleate precursor was injected. Six subsequent 0.5 mL additions of precursors, alternating between sulfur and cadmium oleate solutions, were performed at 1 min intervals, while attempting to maintain a temperature of 220 °C. To monitor reaction progress, a minimal amount of reaction solution was removed via syringe after each injection, added to 2 mL of ODE in an air-free cuvette and analyzed by UV-Vis spectroscopy. After the final cadmium oleate injection, the solution was rapidly cooled by immersing in a room temperature oil bath. The crude reaction mixture was moved into an Ar-filled glovebox. CdS QDs were purified from the reaction mixture using a liquid-liquid extraction with a 3:1 ratio of methanol to reaction mixture, with several drops of isopropanol

added to encourage mixing. The milky white methanol layer was removed, and 1.5 volume equivalents of acetone were added to the yellow ODE layer to precipitate the CdS QDs. After centrifuging, the supernatant was decanted, and the yellow pellet was dissolved in a minimal amount of toluene (~1.5 mL). This precipitation / dispersion purification process was repeated 1 – 2 times, until no signs of cadmium oleate remained (indicated by a milky white, gelatinous precipitate and a peak in the UV-Vis spectrum at 320 nm). The size distribution of QDs was further narrowed using a sequential precipitation. This involved adding isopropanol dropwise just until a precipitate formed, followed by centrifuging and decanting. This process was repeated 1 – 3 times, while the size of the QDs in the supernatant was checked by UV-Vis spectroscopy. The QDs were precipitated by addition of ~ 1 mL methanol. Following centrifugation and decantation, the sample was redispersed in a minimal volume of toluene, and the concentration determined using the absorption spectrum and sizing curves found in Yu et al.[63]

2.2.2. Ligand Exchange

All experiments were performed on nanocrystals functionalized with 3-mercaptopropanoic acid (3-MPA) suspended in methanol. The native oleic acid ligands were replaced with 3-mercaptopropionic acid following a previously reported procedure.[23, 26] 3- MPA (Strem Chemicals, ≥99%) was vacuum distilled to remove impurities and stored under argon. A 70 mM solution of 3-MPA in methanol was prepared and its pH was raised to 11 with tetramethylammonium hydroxide pentahydrate (Sigma, ≥97%). The as-synthesized nanocrystals in toluene were precipitated using methanol, and then vigorously mixed with 1 mL of 3-MPA solution and allowed to sit until it was no longer cloudy. Toluene was added to precipitate the 3-MPA-capped nanocrystals and the resulting particles were collected and re-dissolved in methanol.

2.2.3. WOC Synthesis

The WOC was first synthesized as an ethyl-ester ([Ru(deeb)(tpy)Cl](PF$_6$) deeb = diethyl 2,2'-bipyridine-4,4'-dicarboxylate, tpy = 2,2':6',2"- terpyridine) according to a previously published procedure.[5] The complex was dissolved in methanol with a catalytic amount of triethylamine. The solution reacted for 24 hours, after which the ^{1}H NMR peaks corresponding to the alkyl protons of ethyl esters had completely disappeared and two new peaks corresponding to the methyl esters had formed. The product was vacuum dried and stored under argon. The molar absorptivity of this complex was found to be 16000 M^{-1} cm^{-1} at 518 nm. ^{1}H NMR (300 MHz acetone-d6): δ 10.6 (dd, 1H), 9.3 (s, 1H), 9.1 (s, 1H), 8.8 (d, 2H), 8.66 (d, 2H), 8.52 (dd, 1H), 8.32 (t, 1H), 8.13 (ddd, 2H), 7.96 (d, 1H), 7.83 (dt, 2H), 7.55 (dd, 1H), 7.4 (ddd, 2H), 4.3 (s, 3H), 3.8 (s, 3H). Acc. Mass: found 642.0486 $[M]^+$ calc 642.0486

2.2.4. Steady-State Spectroscopy

UV-visible absorption spectra were recorded using an Agilent 8453 spectrophotometer utilizing tungsten and deuterium lamps at room temperature sealed under Ar in 10 mm quartz cuvettes. CdS QD concentration was 0.3 μM for these experiments as well as steady state PL experiments. PL spectra were obtained at room temperature using a PTI fluorometer with an Ushio UXL-75XE xenon short arc lamp and a Hamamatsu R1527P PMT tube operating at −1000 V DC. The sample was sealed under Ar in a 1 cm x 1 cm quartz cuvette and excited at 360 nm. The emission from 420 nm to 700 nm was recorded at 90° relative to the excitation. Emission spectra were corrected for wavelength dependence of the instrument response. CdS QD concentration was 0.3 μM. The quantum yield of band edge emission was estimated to be on the order of 0.001% using Coumarin 480 (Exciton) excited at 365 nm as a reference (Φ_f = 0.766).[64]

Steady state PL experiments were conducted with highly concentrated samples to maximize the total number of photons detected in each experiment and to make samples more comparable to TA experiments. An undesirable side-effect of this is that the fluorescent emission is filtered by the absorbance of the catalyst while passing through the sample. We correct for these inner filter effects by using Beer's law to calculate the fluorescence intensity prior to attenuation.

$$I_{PL}(R) = I_{Measured}(R) \times 10^{\epsilon_{458} \times 0.3\ \mu M \times R \times 0.5\ cm} \quad (2.1)$$

where ε_{458} = 8000 cm^{-1} M^{-1} is the molar absorptivity of the catalyst at 458 nm (wavelength of the collected PL). We see similar PL quenching behavior using a 3 mm × 3 mm cuvette, where the inner filter effects are weaker, and the uncorrected quenching with the shorter path length overlaps with the corrected quenching in the 1 cm × 1 cm cuvettes.

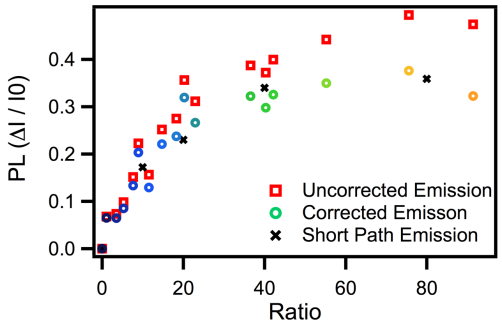

Figure 2.1 Comparison of uncorrected, absorbance corrected, and short path length PL quenching data. © Copyright 2018 American Chemical Society.

2.2.5. TA Spectroscopy

The complete experimental set-up for TA measurements is described in Tseng et al.[35] The concentration of CdS QDs was 4 µM. TA measurements were made with samples sealed under Ar in 2 mm quartz cuvettes at room temperature (293 K). The solutions were stirred continuously with a magnetic stirrer. The pump pulse was passed through a depolarizer and the power was controlled with neutral density filters. The pump beam had a beam waist of ~240 µm, pulse

duration of ~150 fs and pulse energy of ~10 nJ per pulse for the 440 nm excitation of the QDs. The pump powers in all cases were chosen such that the TA decay-trace kinetics were independent of pump power.

Due to the fast decay processes we were examining, it was essential to characterize the instrument response of our TA experiment. This was done as previously described using the solvent response of a 2 mm cuvette of neat methanol.[65-66] Briefly, the methanol sample was placed in the TA spectrometer and pumped with 400 microwatts of 440 nm light to induce stimulated Raman signals. These signals were fit to the sum of a Gaussian with its first and second derivatives, with the width of these features determining the time resolution of the instrument. This scan was also used to correct for the chirp of the white light probe used in the experiment.

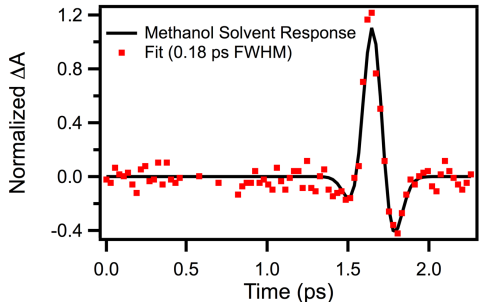

Figure 2.2 Transient absorption kinetics of methanol with a 440 nm pump observed at 598 nm. Fitting this response gives an IRF full width at half maximum of 0.18 ps. © Copyright 2018 American Chemical Society.

2.2.6. PL Upconversion.

PL upconversion was performed using a Halcyone MC multichannel fluorescence upconversion spectrometer with 150 fs temporal resolution (Ultrafast Systems). A fraction (270 µJ/pulse) of the output of our regeneratively amplified Ti:sapphire laser (Solstice, Spectra-Physics, 800 nm, 1 kHz, 100 fs, 3.5 mJ/pulse) was directed into the upconversion system to be used as a gate pulse. The pump pulse for upconversion was produced using an optical parametric amplifier (TOPAS-C, Light Conversion) as previously described.[35] The pump polarization was rotated to

magic angle using a half-wave plate, attenuated, and directed through a 440 nm band pass filter. The pump was then focused to a 35 μm spot and used to excite a sample containing 4 μM QDs in methanol in a 2mm cuvette. Fluorescence was collected in the forward propagating direction and collimated using an off-axis parabolic mirror, then sent through a 470 nm long pass filter to remove residual pump photons. The fluorescence was then focused using another off-axis parabolic mirror into a 0.5 mm thick Type II BBO crystal cut at 46.2 degrees. The delayed gate pulse was mixed with this fluorescence to produce upconverted photons, which were selected using a broad UV-bandpass filter, directed into a spectrograph, and spread onto the pixels of a CCD camera.

The time resolution of the upconversion was determined via upconversion of the residual pump beam. The crystal was rotated to the angle at which the intensity of the sum frequency signal from the pump and gate pulses was maximized. The resulting time resolved signal had a gaussian width of 0.180 ps.

2.3. Results and Discussion

The system under investigation consists of CdS QDs coupled to a mononuclear ruthenium WOC in methanol. The QDs are synthesized using a hot injection method[57, 62] and their surfaces functionalized with 3-mercaptopropionate providing an anionic ligand shell. This ligand exchange allows the QDs to be soluble in the same polar solvents as the WOC, enabling the interaction between the two. They have a 2.76 eV first-exciton absorption feature corresponding to a crystal diameter of 5.2 nm.[63] The WOC is [Ru(dmcbpy)(tpy)Cl]PF_6 (dmcbpy = 4,4′-dimethylcarboxylate-2,2′-bipyridine, tpy = 2,2′:6′,2′′-terpyridine).[11] In methanol the PF_6^- counterion dissociates, enabling a coulombic attraction between the cationic complex and the anionic QD surface.

Charge transfer reactions require a suitable driving for the reaction, which can be determined if the energy levels of the donor and acceptor are known. To examine the energy level

alignment between CdS QDs and the WOC, we estimate the band potentials of the QDs and WOC separately following the approach previously used in a similar system that uses CdS nanorods rather than QDs.[35] The CdS bulk band gap energy (2.5 eV), valence band energy on the vacuum scale (-6.26 eV), conversion from vacuum to NHE scales (-4.4 eV vacuum ≈ 0V NHE) and effective masses of the electron (0.2 m_0) and hole (0.7 m_0) were all used as in Tseng et al.[35] The CdS quantum dots used in this study have an optical band gap of 2.76 eV. The Brus equation was used to calculate the confined electron and hole energies, which were 1.9 V vs NHE and -0.8 V vs NHE, respectively.[16] We anticipate that the redox potentials of the methyl ester versus ethyl ester catalyst derivatives are nearly identical due to the subtle nature of the alkyl perturbation on the ester functionality. These potentials occur at -0.9 V vs NHE (2+/1+) and 1.2 V vs NHE (3+/2+).[11] Comparing the valence band of the QD with the HOMO of the WOC we find that the system has favorable energy level alignment for hole transfer from the photoexcited QD to the WOC, with a large driving force of 700 meV, comparable to what was shown for an analogous ethyl ester functionalized WOC coupled with CdS nanorods.[35]

We briefly note the reasons for modifications to the previously studied system. First, changing the CdS nanocrystal from nanorod to QD enhances the colloidal stability from hours to days, enabling experiments of longer duration, such as PL upconversion. Second, we observed that the ethyl ester WOC complex trans-esterifies in methanol within a period of 24 hours. We thus directly synthesized and characterized the methyl ester complex for consideration in the new QD/WOC system. Figure 2.3a shows UV-Vis absorption spectra for CdS QDs and the WOC as well as their mixture at a 20:1 molar ratio of catalyst to QDs. The spectrum of the mixture solution strongly resembles a sum of the component spectra, implying that neither act to strongly perturb the other in their ground state. Manifestations of the interaction between the catalyst and

nanocrystal can be observed through the steady state band-gap exciton PL (Figure 2.3b). Photoexcitation of CdS QDs at 360 nm leads to recombination of electrons and holes across the QD band gap with a PL spectrum centered around 458nm. Upon addition of the catalyst, excitation at 360 nm is still primarily absorbed by the QDs and the 458 nm QD PL is partially quenched. The catalyst does not exhibit PL.

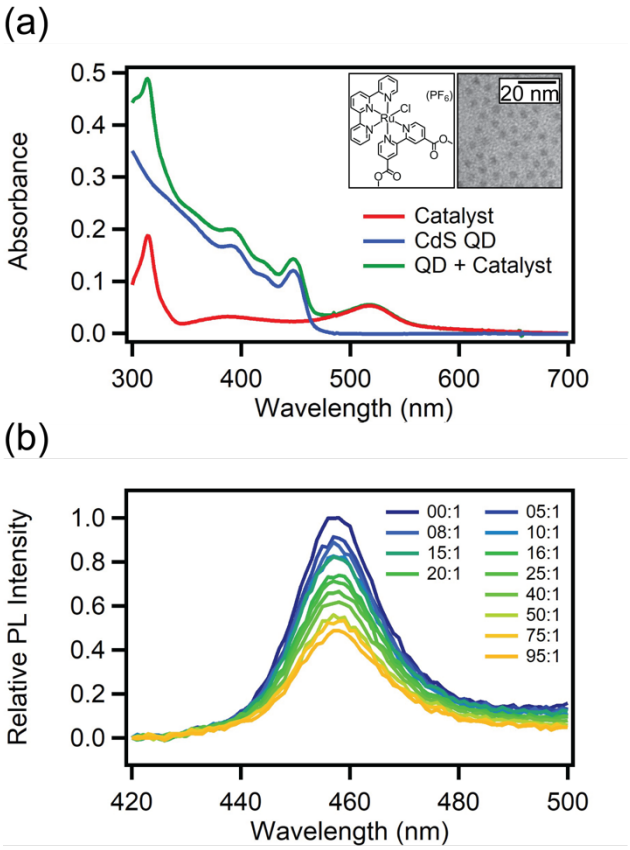

Figure 2.3 (a) UV-Vis absorption spectra of CdS QDs (100 nM), catalyst (2 μM), and their mixture at a 20:1 WOC:QD ratio. (Inset) chemical structure of catalyst and TEM image of CdS QDs. (b) PL spectra of CdS QDs with increasing amounts of catalyst. © Copyright 2018 American Chemical Society.

2.3.1. Kinetic Analysis of Electron and Hole Dynamics

As a first step in assigning the cause of the PL quenching shown in Figure 2.3b, we measured the excited state dynamics of CdS QDs without the catalyst using time-resolved spectroscopy methods that have been previously employed to distinguish the dynamics of band

edge electrons and holes in CdS QDs.[67-68] The bleach signal in TA is a direct reporter of electron population,[39] so by monitoring its decay the timescales of electron transfer and recombination can be observed. In contrast, band gap PL reports on both the electron and the hole populations at the band edge energies of the QDs and its decay is governed by the shorter-lived carrier. The PL signal decays in under ten picoseconds,[67-68] requiring the use of PL upconversion to monitor its kinetics. To obtain accurate hole trapping times using the PL upconversion technique, it is necessary to excite the nanocrystals at 440 nm as 400 nm excitation results in kinetics which are artificially slow due to carrier cooling.[69]

PL upconversion of CdS QD tends to produce kinetics with a low signal-to-noise ratio due to the low quantum yield of QD emission. This can be improved by summing the kinetics acquired across the entire emission feature if the kinetics do not vary with wavelength. The spectrometer used to record upconversion kinetics is designed to spectrally resolve the PL decay by rotating the upconversion crystal during data acquisition. To test the spectral dependence of the decay kinetics, we performed upconversion with a 400 nm pump and a 420 nm long pass filter. This experiment showed no difference in kinetics across the band edge emission feature, aside from the presence of an IRF-limited Raman peak at 454 nm. To improve signal to noise and to decrease the amount of residual pump being upconverted, in further experiments the crystal was left at a fixed angle and the kinetics were averaged across the entire emission feature. An example of the upconversion data acquired using this technique are shown in Figure 2.4. The relative signals shown here should not be taken as representative of their true intensities as the features on either side of the QD emission peak are being attenuated by the limited phase-matching bandwidth of the upconversion crystal.

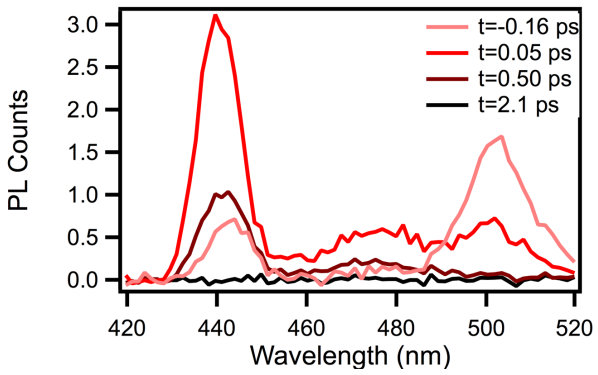

Figure 2.4 PL Upconversion spectrum of 440 nm excited QDs collected using a spectrograph/CCD camera. The x-axis has been converted from detected wavelength to emission wavelength through subtraction of the energy of one photon from the fundamental (12500 cm^{-1}). The peaks seen here correspond to 4 features: upconversion of the pump beam generated as a fourth harmonic of the idler (1760 nm idler, 440 nm fourth harmonic), upconversion of the sum frequency of the fundamental and the signal (1467 nm signal, 518nm SFI), Raman scattering from the solvent (~507 nm), and emission from the nanocrystal (centered at 458, but attenuated by long pass filter and by the phase matching angle of the crystal). The nanocrystal spectrum was identified by taking a scan of pure solvent, and the crystal angle optimized to maximize this feature while minimizing pump related features.

A comparison of the decays of the QD PL upconversion signal and the TA bleach signal monitored at 454 nm (Figure 2.5) following 440 nm excitation shows that the bleach is considerably longer lived than the band gap emission. The TA bleach has a half-life of 14.5 ns. The signal from PL upconversion, on the other hand, decays as a single exponential with a lifetime of 0.21 ± 0.01 ps.

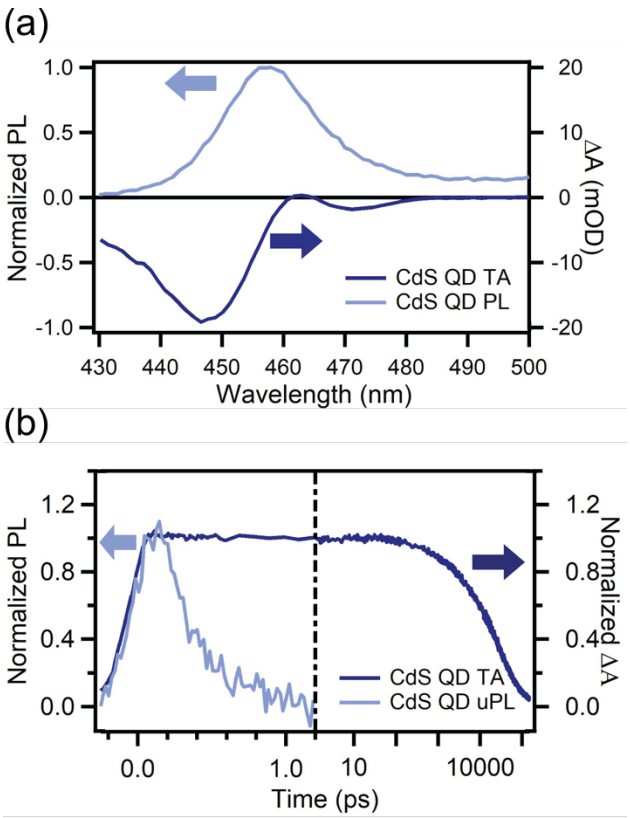

Figure 2.5 (a) PL and TA spectra of CdS QD with no added catalyst. (b) TA (454 nm) and PL kinetics (averaged across emission feature shown in Figure 2.4). These kinetics indicate that the hole trapping is the limiting process for band edge emission and occurs with a time constant of 0.21 ± 0.01 ps. © Copyright 2018 American Chemical Society.

As has been previously discussed,[70] this drastic difference in timescales allows PL upconversion decay to be attributed entirely to changes in the hole population. More specifically, the short band-gap PL lifetime of CdS QDs has been ascribed to hole trapping,[67] which occurs on a sub-picosecond to picosecond timescale in thiol-capped CdS nanocrystals.[46, 56, 71-72] Hole trapping is ubiquitous, fast, and efficient in CdS QDs with a variety of surface functionalizations, including the native organic ligands used in synthesis.[67-68] The fast hole trapping dynamics in our thiol capped QDs are responsible for their low quantum yield of band gap emission (10^{-5}), and the 0.21 ps lifetime we measure is consistent with a previously reported radiative lifetime on the order of 10 ns.[73]

The hole trapping dynamics are also seen in the TA spectra as a rise in the broadband photoinduced absorption (PA) feature to the red of the bleach (Figure 2.6). This signal has been shown to rise in on the timescale of hole trapping, allowing us an alternate measurement of hole trapping kinetics. The rise kinetics of the PA are 0.2 ± 0.01 ps, while the PL upconversion decays with a lifetime of 0.21 ± 0.008 ps. The bleach kinetics are included for comparison, exhibiting an instrument limited rise. The kinetics obtained from the upconversion were preferred over the results from the PA feature for determining the rate of hole trapping as the coherent artifact in methanol lead to difficulty in obtaining consistent fits of this fast-rising feature.

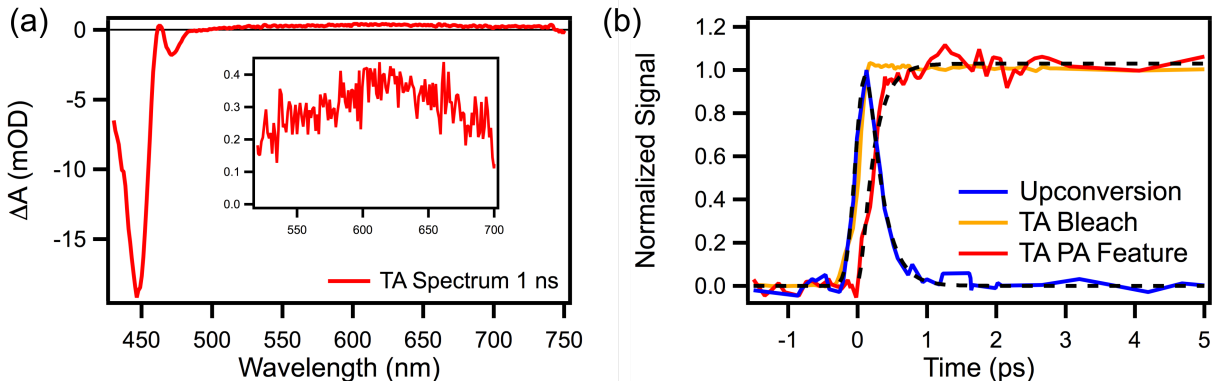

Figure 2.6 (a) TA spectrum collected 1 ns after excitation. Inset: Broadband photoinduced absorption (PA) feature. (b) Comparison of PL upconversion decay kinetics of the CdS band edge emission compared to the rise of the PA feature in the TA spectra, averaged from 520-650 nm. Both kinetics are fit to exponentials convoluted with the IRF of their respective experiments (fits shown in dashed lines).

We next examine how the addition of the WOC impacts excited state dynamics of CdS QDs (Figure 2.7). When the catalyst is added in a 10:1 WOC:QD ratio, the kinetics of the TA bleach feature do not change in the 2 ps time window in which band gap emission occurs. As shown in Figure 2.7b, the change in TA kinetics happens on a much longer timescale and cannot lead to significant PL quenching of the band-edge emission. Since there is not an electron process fast enough to change the PL lifetime, the quenching seen in Figure 2.3 cannot be due to electron or energy transfer. By contrast, upconversion measurements of the band gap PL show a lifetime

decrease from 0.210 ± 0.01 ps to 0.180 ± 0.01 ps upon addition of 7 equivalents of the catalyst. The decrease of PL lifetime without a correspondingly fast change in electron lifetime indicates that the catalyst is causing the quenching through band edge hole transfer.

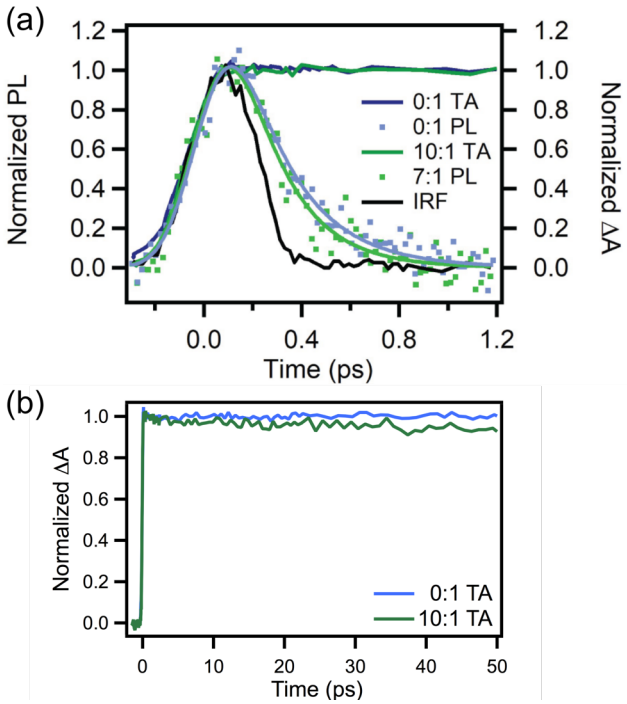

Figure 2.7 (a) Comparison of electron and hole signals in the presence and absence of catalyst. The TA dynamics are unaffected by the presence of catalyst on this timescale, implying that the PL dynamics are entirely due to holes. The decrease in PL lifetime from 0.21 ± 0.01 ps to 0.18 ± 0.01 ps (fits to upconversion data are shown in the figure using solid lines) indicates that hole transfer to the catalyst is competitive with the hole trapping process. (b) TA kinetics of the bleach feature for the first 50 ps for 0:1 and 10:1 samples. The catalyst does induce a slight decay on this time window, possibly recombination following hole transfer to the catalyst as was previously hypothesized for the ethyl ester system.[35] We disregard this decay in our analysis as it is well separated in time from hole transfer. © Copyright 2018 American Chemical Society.

To test whether the lifetimes extracted from fitting our PL upconversion data in Figure 2.7 are statistically distinguishable, we performed a bootstrap Monte Carlo analysis on the data. This method is useful to find errors associated with parameters in nonlinear fit functions through resampling of data.[47, 74] The resulting distribution of lifetimes for our two samples are shown in Figure 2.8. The uncertainties were found to be 0.01 ps for both fits. 1000 resamples were executed

for each data set. This analysis confirms that our experiment is sensitive enough to distinguish the difference in lifetime between these two samples.

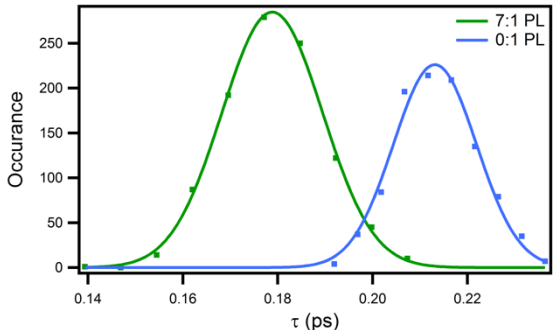

Figure 2.8 Distributions in fitted lifetime obtained through resampling of 0:1 and 7:1 WOC:QD mixtures. Histograms were generated from bootstrap Monte Carlo analysis of both data sets over 1000 different fits. Gaussian fits to the distributions established a peak of 0.21 ps at 0:1 and 0.18 ps at 7:1 with standard deviations of 0.01 ps for each. © Copyright 2018 American Chemical Society.

While a lifetime change of the band-gap PL indicates competitive hole-transfer from CdS QDs to the WOC, the determination of a *rate constant* requires quantification of the number of WOC molecules that are bound per QD. This, in turn, requires varying the WOC concentration. We encounter an experimental limitation associated with the instrument response function (IRF) of the PL upconversion experiment (Figure 2.7) so that shorter lifetimes that result from increasing the WOC:QD ratio would be difficult to distinguish in this experiment. Although the PL lifetime changes when catalyst is added, the time resolution of the measurement is insufficient to determine the percentage of bound catalysts using the decay kinetics alone. For this reason, we combine the result of the CdS QD PL lifetime measurement with PL quenching as a function of WOC:QD ratio and develop a model that allows us to extract both a binding equilibrium constant and the hole transfer rate constant.

2.3.2. Construction of PL Quenching Model

Figure 2.3 showed that the change in band gap PL intensity decreases as the WOC:QD ratio is increased, with saturation at high ratios. Although there are established methods in the nanocrystal literature[55] to describe PL quenching with a Langmuir isotherm model when quenching is efficient[56, 75] or with a competitive charge transfer model when binding is strong,[51, 76,] our system presents a challenge because we cannot make either assumption and the binding equilibrium and quenching efficiency need to be accounted for simultaneously.[77]

We developed a model that combines the effects of chemical equilibrium, competing decay pathways and a limited number of surface binding sites as adjustable parameters to fit the PL quenching data over a range of WOC concentrations and obtain a per-catalyst hole-transfer rate constant. Assuming single exponential decay and hole-transfer kinetics, the quantum efficiency of band edge hole-transfer for a quantum dot with n bound catalysts can be modeled with the expression shown in

$$\Phi_{HT}(n) = \frac{nk_{HT}}{k_{trap} + nk_{HT}} = \frac{n(k_{HT}/k_{trap})}{1 + n(k_{HT}/k_{trap})} \quad (2.2)$$

where k_{trap} is the intrinsic rate of decay of the nanocrystal band edge exciton, dominated by hole trapping, and k_{HT} is the rate of hole transfer.

Due to the large size of nanocrystals, binding of quenchers to nanocrystal surfaces often leads to inhomogeneity in the sample where some nanocrystals have many quenchers attached and others have relatively few.[75, 78] This can be modeled by assuming a distribution in the number of quenchers bound per nanocrystal and averaging the quenching model over this distribution. We first assume that the effects of the distribution of catalysts per nanocrystal is negligible, and use the average value of n, $\langle n \rangle$, as an approximation for the true behavior of the system

$$\Phi_{HT}(\langle n \rangle) \approx \frac{\langle n \rangle (k_{HT}/k_{trap})}{1 + \langle n \rangle (k_{HT}/k_{trap})} \quad (2.3)$$

Equation 2.3 has been used previously for quenching of nanocrystal fluorescence where the average number of bound catalysts is known from prior experiments.[51] We do not have a direct measurement of the average number bound, but instead use a Langmuir adsorption isotherm to relate the mixing ratio of catalyst and nanocrystal to the average number of bound catalysts per nanocrystal.

Langmuir binding isotherms have been used frequently in the literature to model the binding of many types of substrate to nanocrystal surfaces.[7, 76, 79] The Langmuir expression for the number of free catalysts as a function of fractional surface coverage is

$$[n_{free}] = \frac{\theta}{K_{eq}(1-\theta)} \tag{1.4}$$

where $[n_{free}]$ is the concentration of free catalysts in solution, θ is the fractional surface coverage, and K_{eq} is the binding equilibrium constant. Rewriting this in terms of bound catalysts,

$$[n_{bound}] = [n_0] - [n_{free}] = [n_0] - \frac{\theta}{K_{eq}(1-\theta)} \tag{2.5}$$

$$\langle n \rangle = \frac{[n_{bound}]}{[QD]} = \frac{[n_0] - \frac{\theta}{K_{eq}(1-\theta)}}{[QD]} \tag{2.6}$$

where $[n_0]$ is the initial concentration of catalyst before binding and $[QD]$ is the concentration of QDs added. Assuming the same number of binding sites per nanocrystal, θ can be given by $\theta = \frac{\langle n \rangle}{N}$ with N being the total number of binding sites on each nanocrystal. Substituting this in and writing the equation in terms of the mixing ratio of catalysts and nanocrystals, R, we obtain

$$\langle n \rangle = \frac{[n_0] - \frac{\frac{\langle n \rangle}{N}}{K_{eq}\left(1 - \frac{\langle n \rangle}{N}\right)}}{[QD]} = R - \frac{\langle n \rangle}{K_{eq}[QD](N - \langle n \rangle)} \tag{2.7}$$

This can be solved for $\langle n \rangle$

$$\langle n \rangle = \frac{\left(R + N + (K_{eq}[QD])^{-1}\right) \pm \sqrt{\left(R + N + (K_{eq}[QD])^{-1}\right)^2 - 4RN}}{2} \tag{2.8}$$

The positive root is discarded as nonphysical ($\langle n \rangle > R$). Our final fit expression is obtained by substituting (2.8) into (2.3).

$$\Phi_{HT}(\langle n \rangle) = \frac{(k_{HT}/k_{trap})\dfrac{\left(R + N + (K_{eq}[QD])^{-1}\right) - \sqrt{\left(R + N + (K_{eq}[QD])^{-1}\right)^2 - 4RN}}{2}}{1 + (k_{HT}/k_{trap})\dfrac{\left(R + N + (K_{eq}[QD])^{-1}\right) - \sqrt{\left(R + N + (K_{eq}[QD])^{-1}\right)^2 - 4RN}}{2}} \quad (2.9)$$

We now evaluate the assumption made in (2.3) that the eventual functional form is not sensitive to the distribution of catalysts on nanocrystal surfaces. If binding events are independent, for a nanocrystal with N available binding sites the distribution of bound catalysts follows binomial statistics[77, 79]

$$P(n) = \binom{N}{n}\left(\frac{\langle n \rangle}{N}\right)^n \left(1 - \frac{\langle n \rangle}{N}\right)^{N-n} \quad (2.10)$$

We may then average over the distribution to find the observed efficiency of hole transfer for a solution with $\langle n \rangle$ average bound catalysts per QD.

$$\Phi_{HT}(n) = \sum_{k=0}^{N} \frac{n(k_{HT}/k_{trap})}{1 + n(k_{HT}/k_{trap})}\binom{N}{n}\left(\frac{\langle n \rangle}{N}\right)^n \left(1 - \frac{\langle n \rangle}{N}\right)^{N-n} \quad (2.11)$$

We combined (2.8) and (2.11) to produce a fit function accounting for the distribution of bound catalysts.

2.3.3. Quantitative Analysis of Steady State PL

Having derived expressions for modelling the PL data we have collected, we now use them to fit the PL quenching as a function of mixing ratio.

Figure 2.9 shows the fit of (2.9) to our PL quenching data and the resulting values of N, k_{HT}/k_{trap}, and K_{eq}. In the following paragraphs, each parameter is discussed individually. We also performed fits to the data accounting for the distribution with (2.11). The obtained fit parameters for N, k_{HT}/k_{trap}, and K_{eq} changed by 0.6%, 5%, and 8% respectively, implying that the distribution

has only a minor impact on the fit. This justifies our use of the averaged model given by (2.9) and the fit parameters that it produces.

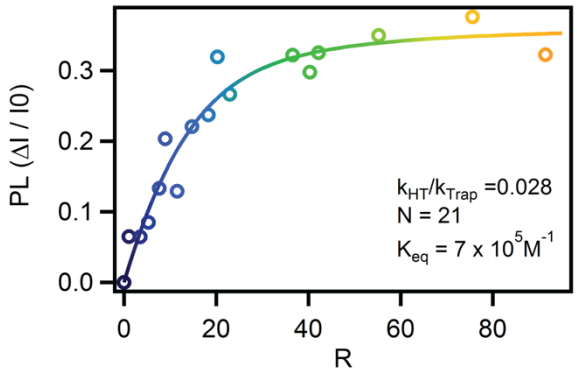

Figure 2.9 Fractional quenching of band-gap PL as a function of ratio of WOC to QD. The data is fit to (2.9) to measure both the competitive quenching and trapping efficiency and Langmuir binding equilibrium. © Copyright 2018 American Chemical Society.

Starting with N, fit values indicate that a maximum of 21 ± 4 WOC molecules can bind to each QD. To contextualize this number, we estimate the maximum number of catalysts which can bind to the surface, limited by the volume near the nanocrystal. We approximate catalysts as spheres with a diameter ~1.2 nm, which is the width of a ruthenium-bound terpyridine molecule. If we include the length of a fully extended 3-MPA molecule (~0.6 nm), the radius of the quantum dot is ~3.3 nm. Therefore, the volume contained within a monolayer of catalysts is approximately:

$$V_{mono} = V_{QD+Ru} - V_{QD} = \frac{4}{3}\pi(2.65\ nm + 0.6\ nm)^3 - \frac{4}{3}\pi(2.65\ nm)^3 = 65\ nm^3 \qquad (1.12)$$

Using the packing efficiency of spheres (74%) as an estimate, we obtain a value of 48 nm^3 that can be occupied by catalysts. Each spherical catalyst would have a volume of approximately 0.9 nm^3, which implies that a maximum number of 53 catalysts can be bound. This is somewhat similar to our result from PL fitting of 21 bound catalysts, implying that catalyst binding is possibly limited by the volume of the bound catalysts rather than charge balance of the surface ligands. The measured maximum surface coverage is 40% of the maximum determined in this analysis. This is a reasonable surface coverage result, given that maximum surface coverages of up to 56% of the

geometric maximum were previously seen for ferrocene derivatives, a complex of similar size, covalently tethered to a nanocrystal surface.[51]

The observed K_{eq} of $7 \pm 0.7 \times 10^5$ M^{-1} suggests that catalysts bind readily to the nanocrystal surface; for our PL experiment, 73% of catalysts in solution were bound at a 11:1 mixing ratio (half saturation of the PL quenching). This is a large equilibrium constant, comparable to ruthenium complexes binding to TiO_2 through phosphonate groups[80] and an order of magnitude larger than viologens adsorbing to the surface of a CdS nanocrystal,[75] but several orders of magnitude smaller than the K_{eq} observed for alkanethiols adsorbing to a CdSe surface.[76] Strong binding between the catalyst and nanocrystal is important for the efficiency of hole scavenging. This is especially crucial in the catalysis of multi-electron reactions, as the catalyst must reside on the surface long enough to complete four charge transfers.

The large equilibrium binding constant K_{eq} suggests an intimate contact between the donor and the acceptor. However, this is not a sufficient condition for efficient hole transfer given the fast and efficient hole trapping evidenced by short-lived band-gap PL (Figure 2.5). We therefore examine parameters in the model that govern the hole transfer rate to the catalyst. From our fit we find a ratio of k_{HT} to k_{trap} of 0.028 ± 0.004 per catalyst. As k_{trap} is $4.8 \pm 0.3 \times 10^{12}$ s^{-1} from our upconversion experiments (Figure 2.5), k_{HT} is $1.3 \pm 0.2 \times 10^{11}$ s^{-1} per WOC. Based on this result, it is possible to estimate the rate of PL decay for the 7:1 mixing ratio used in our PL upconversion experiment. Under those mixing conditions, the average number of catalysts per nanocrystal is 6.8, leading to a hole transfer rate of 9.0×10^{11} s^{-1}, which, when added to the hole trapping rate constant, corresponds to a lifetime of 0.18 ± 0.01 ps. Notably, this value is identical to our fitted result from the upconversion experiment of 0.18 ps (Figure 2.7), indicating that our model is accurately capturing the quenching behavior of both steady state and time-resolved quenching experiments.

The maximum achievable hole transfer rate in this system is $2.8 \pm 0.6 \times 10^{12}$ s^{-1} when the surface is saturated with the catalyst.

Measurements of hole transfer rate constants from cadmium chalcogenide quantum dots are difficult, and are sometimes reported in the literature for systems with an unknown number of bound acceptors capable of receiving holes. In cases where acceptor numbers are known, hole transfer rates of $>3 \times 10^{12}$ s^{-1} have been reported, with the largest value found in a system with 50 bound acceptors.[72] For systems where a rate constant was quantified for a 1:1 mixing ratio, values range from 4.0×10^{6} s^{-1} to 5.0×10^{9} s^{-1}.[51, 81-82] For our system, both the 1:1 and the maximum hole transfer rate (1.3×10^{11} s^{-1} and 2.8×10^{12} s^{-1}, respectively) are exceptional in their magnitude, enabling productive competition against the sub-picosecond trapping process. These values are comparable to a system that exhibits sub-picosecond hole transfer (instrument limited at 300 fs) between CdS QDs and phenothiazine (PTZ) molecules that are covalently attached to CdS QDs using a dithiocarbamate bridge.[72] Those fast rates were attributed to strong electronic coupling between the hole donor and acceptor moieties mediated by the dithiocarbamate bridge, as evidenced by changes in the QD absorption spectra upon binding of PTZ. Our systems have different driving forces for hole transfer and are in different solvents, so a direct comparison between parameters relevant for charge transfer rate will not elucidate the reasons for the fast hole transfer observed in our system. We do note, however, that we do not observe strong perturbations to the QD or WOC absorption spectra upon interaction. This suggests the possibility of a different type of electronic coupling, such as super-exchange via ligand orbitals on the WOC, that would enable the large value of k_{HT} in our system. Further work is needed to explore this possibility.

The fast hole transfer from the valence band has significant implications on the design of nanocrystal-based systems for water oxidation. For these particular QD/WOC systems, the yield

of valence band hole transfer is limited by competition with hole trapping. Despite the favorable binding and k_{HT}, hole trapping – under conditions of a single bound catalyst – occurs 37 times faster than hole transfer. Assuming independent hole transfer events of identical speed, no transfer of trapped holes, negligible back hole-transfer, and recognizing that four oxidations are required for turnover during water oxidation, this system would need to absorb ~10^6 photons to generate a single molecule of oxygen. Therefore, the primary way of improving the catalytic viability of this system should be decreasing the trapping rate.

Several methods have been developed to reduce hole trapping based on modifications to the surface of the particle. Ligand exchanges have been performed which decrease hole trapping rates, even to the limit of trap-free QDs,[83] though it is not yet clear whether such methods would have deleterious effects on catalyst binding. Other methods decrease the trapping rate for QDs by epitaxially growing a semiconductor shell on the particle creating a heterostructure and decreasing numbers of surface traps.[84-85] The disadvantage of using heterostructure systems lies in their slower charge transfer rates due to the shell acting as a tunneling barrier.[51, 86] Nevertheless, heterostructures have been used successfully for hole transfer and have demonstrated up to a 99% hole transfer quantum yield.[51] Substituting the CdS QDs in our system with a trap-free QDs or heterostructure is a viable systematic handle to decrease the trapping rate. Since hole transfer is already so fast and recombination comparatively slow (~60 ns), this could lead to a net gain in charge transfer efficiency.

2.4. Conclusions

Utilizing a combination of ultrafast and steady-state spectroscopies, we have determined the rate constant for hole transfer from a photoexcited CdS nanocrystal to a water oxidation catalyst, as well as the equilibrium constant for catalyst binding. The rate of hole transfer is

comparable to hole trapping and orders of magnitude faster than electron-hole recombination. In this and similar systems, efforts to improve function can now focus on extending hole lifetimes in order to approach practical turnover conditions.

Chapter 3 The Hole Picture: A Comprehensive Description of Carrier Dynamics for Two CdS Quantum Dot/Water Oxidation Catalyst Systems

3.1. Introduction

Semiconductor nanostructures are a useful model system for the development of solar fuel technologies due to their strong light absorption, high surface-to-volume ratios, and tunable ligand shells which facilitate coupling to bound co-catalysts.[7, 63, 87-88] These properties have enabled the study of a variety of light-driven reductive reactions utilizing CdS nanocrystals as photosensitizers.[5, 23, 26, 29, 46] In these studies sacrificial hole scavengers are added to prevent oxidative damage to the semiconductor or ligands following accumulation of holes.[19, 21, 89] Although oxidation of scavengers allows for reductive catalysis to be studied in a controlled environment, application of these systems to solar fuel generation schemes will require the replacement of these scavengers with catalysts capable of removing holes through water oxidation.[1]

Photocatalytic water oxidation presents a number of challenges. Four holes must be transferred to a single catalytic active site to achieve turnover.[9] Between photoexcitation events, electron-hole recombination removes holes from the active site preventing charge accumulation. These recombination events must be characterized to aid in electron removal and optimize the efficiency of water oxidation. Several mechanistic studies of the competition between charge transfer and recombination in reductive systems have been performed,[45-47] but comparatively few studies of hole transfer and recombination have been undertaken in hole scavenging model systems,[56] and only initial hole transfer rates determined for water oxidation catalysts.[33, 41]

In this work we use a battery of spectroscopic techniques to fully characterize the excited state dynamics in two systems composed of Ru-based water oxidation catalysts (WOC) bound to CdS quantum dots (QDs). The first of these systems utilizes a catalyst which has been previously demonstrated to accept holes from the photoexcited QD to on a picosecond timescale.[41] We discover that aside from its fast hole transfer properties, additional dynamics are present which allow decay of excited states through electron transfer to bound catalysts. The second system utilizes a catalyst with a similar structure, but with a higher LUMO level to prevent electron transfer and support our conclusions about the decay pathways of catalyst 1. Both systems show favorable dynamics for photocatalytic water oxidation, with the catalytically relevant charge-separated state existing for 4 orders of magnitude in time. These measurements allow us to evaluate potential synergy with reductive co-catalyst partners towards the goal of overall water-splitting.

3.2. Materials and Methods

3.2.1. CdS QD Synthesis and Characterization

CdS QDs were synthesized following the methods described in Chapter 2.[41] All measurements except PLE were performed using a single synthesis of QDs which was stored under argon in a glovebox. The sample used for PLE with catalyst 2 is the same sample previously described in Chapter 2, with a diameter of 5.2 nm and a first exciton transition at 450 nm.[41] The sample used for all other measurements was characterized using UV-visible spectroscopy and TEM imaging (Figure 3.1) to have a 452 nm first exciton transition (2.74 eV) corresponding to a size of 5.4 nm as determined from published sizing curves.[63]

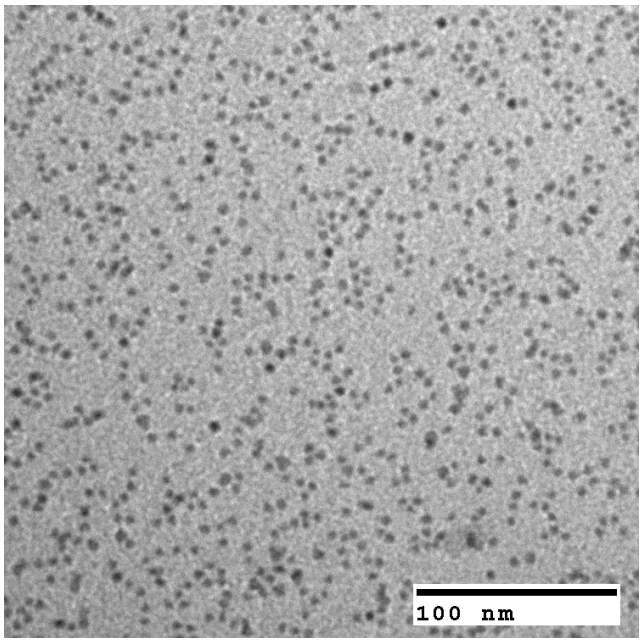

Figure 3.1 TEM micrograph of CdS QDs.

3.2.2. Ruthenium Catalyst Synthesis and Characterization

Catalyst 1 was prepared following the methods described in Chapter 2.[41] Catalyst 2 was synthesized following previously published procedures.[11, 90] ^{1}H NMR and ESI(+) MS were used to confirm the identity and purity of each species.

3.2.3. Steady-State Spectroscopy (UV-Vis, PL, PLE)

UV-visible absorption spectra were recorded using a Cary 60 spectrophotometer (Agilent) using a Xenon flashlamp as an excitation source and observing samples at room temperature in 10 mm quartz cuvettes sealed under Ar. Typical concentration was 0.1 μM for these as well as PL experiments. PL spectra were obtained under conditions of vigorous stirring at room temperature (293 K) using a Fluorolog-3 fluorometer (Horiba) with a 450 W xenon lamp and a Hamamatsu R928P PMT. A photodiode reference was used to ratiometrically compensate for fluctuations in the lamp intensity. Emission was recorded at 90° relative to the excitation. In experiments where the PL was recorded at a wavelengths double the excitation wavelength a 420 nm long pass filter was added after the sample to remove the second order diffraction peak. Emission spectra were

corrected for wavelength dependence of the instrument response. The steady state absorption of each sample was used to compensate for the attenuation of the excitation and emission light as described in Chapter 2.[41]

PLE Spectra were recorded on a SLM AMINCO 8000C spectrofluorometer which has been previously described.[57] A fraction of the excitation light was split-off prior to hitting the sample and its intensity was monitored using a rhodamine B quantum counter with a Hamamatsu R928 PMT detector operating at 700 V direct current. The measured emission intensity was corrected for the excitation intensity at each wavelength through division by the quantum counter signal, and converted to absorbance units using

$$A \propto -\log_{10}(1 - I_{PL}/I_{QC}) \tag{3.1}$$

where I_{PL} is the observed signal of the PL and I_{QC} is the observed signal from the quantum counter.

3.2.4. Cyclic Voltammetry and Spectroelectrochemistry

Cyclic voltammetry was performed using a previously described apparatus.[91] A three-electrode setup was constructed using a 1.6 mm Pt working electrode, Pt wire counter electrode, and 0.01 M $Ag/AgNO_3$ reference electrode. Measurements were made using a CH Instruments 601C electrochemical analyzer. Analyte solutions of approximately 1 mM were dissolved in freshly made solutions of acetonitrile with 0.1 M tetrabutylammonium hexafluorophosphate ($TBAPF_6$) supporting electrolyte. Measurements were made following a 5-minute N_2 bubbling and were referenced to ferrocene as an internal standard. Data were acquired with a scan rate of 100 mV/s. Conversion from a ferrocene to NHE reference was performed using conversion factors from Pavlishchuk and Addison.[92]

Spectroelectrochemical results were acquired using a home-built OTTLE cell (optically transparent thin-layer electrode) which has been described previously.[91] This cell consists of a transparent platinum mesh working electrode, a platinum wire auxiliary electrode, and a 0.01 M

$Ag/AgNO_3$ in acetonitrile reference electrode. The three-electrode cell was constructed in a 2 mm thick cuvette with 0.1 M $TBAPF_6$. Analyte was added to bring the solution to an absorbance of 0.1 at the lowest MLCT transition and the cell was bubbled with N_2 for 5 minutes prior to data collection.

3.2.5. Visible TA Spectroscopy

The complete experimental set-up for TA measurements is described in Tseng et al.[35] 2 μM solutions of CdS QDs were sealed under Ar in 2 mm quartz cuvettes at room temperature (293 K). The solutions were stirred continuously with a magnetic stirrer. The depolarized pump beam had a beam waist of ~240 μm, pulse duration of ~150 fs and pulse energy of 30 nJ per pulse for the 440 nm excitation of the QDs. The pump powers in all cases were chosen such that the TA decay kinetics were independent of pump power (<0.3 excitations per QD).

3.2.6. NIR TA Spectroscopy

NIR TA spectroscopy was performed using a Helios spectrometer (Ultrafast Systems, LLC) utilizing an InGaAs detector and coupled to the same laser and OPA used in visible TA spectroscopy and PL upconversion. The pump beam for NIR TA is depolarized, chopped at 500 Hz, and focused into the sample in a 200 μm FWHM spot. Pump power was attenuated using neutral density filters to keep the excitation density below 0.3 excitations per QD. To produce the NIR probe, a small amount (~2 nJ/pulse) of 800 nm fundamental from the laser was directed into the system and delayed by up to 8 ns. This 800 nm fundamental was focused into a thick sapphire plate generating a probe continuum (950-1600 nm) which is focused into the sample. The probe beam is overlapped in the sample with the pump beam, collimated, and filtered to remove the visible continuum and fundamental. The probe is finally focused into a fiber coupled spectrograph and detector synchronized to the repetition rate of the laser. Samples were made at a concentration

of 2 μM QDs and were stirred continuously during acquisition. The IRF was measured by replacing the sample with a glass slide and recording the duration of optical Kerr effect signal in the medium (FWHM=0.35 ps).

To measure the hole kinetics the NIR TA signal was averaged from 1350 nm to 1450 nm. This signal is known to contain contributions from both the valence band hole and conduction band electron, but since the conduction band electron population is static on this timescale these kinetics can be numerically removed through addition of a y-offset to the decay function.

3.2.7. PL Upconversion Spectroscopy

PL upconversion was performed using a Halcyone Spectrometer as described in Chapter 2.[41] Samples containing 2 μM QDs in methanol were prepared in sealed 2 mm cuvettes under argon. Excitation was performed at 440 nm, and the pulse energy attenuated using ND filters to prevent multiple excitation events within a single QD (~1 nJ). Samples were stirred continuously during data collection.

3.2.8. TCSPC and TRES Spectroscopy

Time-Correlated Single Photon Counting (TCSPC) was performed using a DeltaFlex system (Horiba) equipped with a 402 nm pulsed diode laser excitation source. The vertically polarized laser beam was focused into the sample. Emission from the sample was collected at 90° from excitation, collimated and directed into a monochromator coupled to a PMT. The emission was tested for anisotropy effects using a polarizer placed before the monochromator, but none were observed upon changing the polarization. An IRF was measured at 402 nm with a dilute solution of silica and found to have a 220 ps FWHM for a 100 ns time window.

In a typical experiment a 0.2 μM solution of QDs was sealed in a 10 mm cuvette under Ar and placed in the sample chamber. Samples were continuously stirred and maintained at 293 K

using a recirculating water bath. Excitation was performed at 500 kHz for 100 ns time windows and 100 kHz for 6.8 μs time windows. Data acquisition lasted from 5 to 15 minutes at a single wavelength with a monochromator bandpass of 12 nm. UV-Visible spectroscopy showed no signs of sample degradation over the course of the experiment.

For Time-Resolved Emission Scans (TRES) samples were produced identically as other TCSPC experiments. Scans were carried out for fixed durations at each wavelength (typically 15 minutes/decay for a 100 ns time window) with a 12 nm bandpass, with scans taken every 30 nm. Spectra were corrected for detector sensitivity between 500 nm and 800 nm using the NIST standard reference material SRM 2943.

3.3. Results and Discussion

The systems under investigation consist of CdS QDs in solution with one of two Ru-based water oxidation catalysts with similar structures but distinct energetics. The QDs have a first exciton transition at 452 nm, a diameter of 5.4 nm, and are ligand exchanged to have polar 3-mercaptopropionate (3-MPA) surface ligands to facilitate interaction with the catalysts. Catalyst 1, $[Ru(dmcbpy)(tpy)Cl]PF_6$ (dmcbpy = 4,4′-dimethylcarboxylate-2,2′-bipyridine, tpy = 2,2′:6′,2′′-terpyridine), has previously been shown to quickly accept photoexcited holes from CdS QDs with efficiency limited by trapping of holes to the QD surface.[41] Catalyst 2 $[Ru(bpy)(tpy)Cl]PF_6$ (bpy=2,2′-bipyridine) is a very commonly studied mononuclear WOC with a similar structure to catalyst 1.[11] The two catalysts have distinct energy levels, with catalyst 1 having both HOMO and LUMO levels at a lower electrochemical potential. The redox potentials of both catalysts and the nanocrystal are shown in figure 2a, showing that both catalysts have substantial driving force to accept holes from the photoexcited nanocrystal. The band potentials of the QD were estimated using the Brus Equation, as described in Chapter 2,[41] while the HOMO and LUMO potentials of

the catalysts were measured using cyclic voltammetry. The measured catalyst orbital energies showed superb agreement with those reported in the literature for catalyst 2 and the ethyl-ester analogue of catalyst 1.[11]

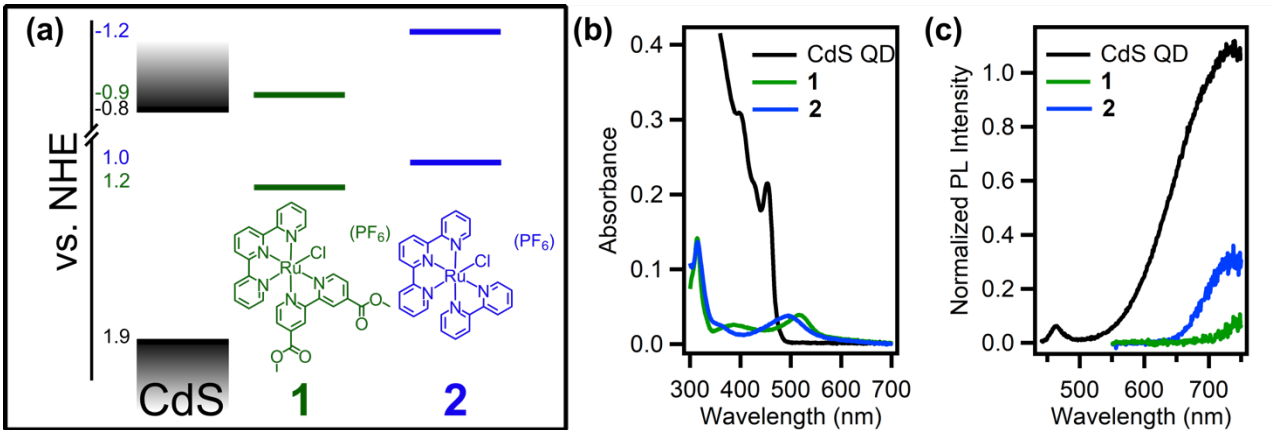

Figure 3.2 (a) Band potentials of CdS QD and redox potentials of catalyst 1 and 2. (b) UV-Vis spectra of CdS QD and both catalysts. (c) PL spectra of CdS QD (0.07 μM), catalyst 1 (5 μM), and catalyst 2 (11 μM). The QD sample was excited at 360 nm, and catalysts 1 and 2 were excited at their respective MLCT maxima.

Figure 3.2b shows the absorption spectra of the two catalysts and the QDs. The QD absorption spectra show the characteristic transitions of CdS QDs including a first exciton peak at 452 nm. This spectrum corresponds to QDs with a narrow size distribution centered around 5.4 nm, consistent with what is seen through TEM imaging (Figure 3.1). Catalyst 1 exhibits a MLCT transition with a peak at 518 nm (ε=16,000),[41] while the MLCT transition for catalyst 2 peaks at 496 nm (ε=10,000).[93] Upon mixing either catalyst with the QDs the UV-Vis spectrum does not undergo any strong changes, appearing to be a superposition of the two components.

The PL spectra of samples are shown in Figure 3.2c. The QD fluorescence consists of a band edge emission and a trap emission feature. Band edge emission is peaked around 463 nm and occurs through radiative recombination of a valence band hole and conduction band electron. The trap emission is broader and centered around 729 nm. This feature is ascribed to multiple types of carrier recombination,[94] although the primary component at the emission maximum is believed to

be due to recombination between a trapped hole and band edge electron.[35, 45, 95] The emission spectrum of catalyst 1 has an emission feature which is far to the red and too weak for our instrument to adequately characterize. Catalyst 2 has a weak but detectable emission feature at 736 nm which has been ascribed to phosphorescence from a metal-to-ligand charge transfer (MLCT) state.[96] This peak is much narrower than the nanocrystal trap emission, with a full width at half maximum of 93 nm for the catalyst feature compared to 189 for the trap emission.

In Chapter 2, catalyst 1 was shown to have a hole transfer rate constant of 1.3×10^{11} s^{-1} per catalyst and hole transfer was shown to have efficiency limited by competition with hole trapping.[41] Building upon this work we will now attempt to discern the decay pathways which return the excited system to the ground state. Modelling these later processes is especially challenging due to the different decay pathways available depending on if the hole was trapped or transferred on the picosecond timescale. We designate these two populations the trapped-hole population and the direct hole transfer population. Our approach in identifying both the decay pathway, and the population undergoing decay involves a combination of time-resolved and steady state spectroscopies. We will begin by studying the steady state quenching and time-resolved quenching kinetics of the trap emission by catalyst 1. This will allow us to isolate the kinetics of the trapped hole population. We will then examine the TA which contains signatures of both trapped hole and direct hole transfer populations and facilitates identification of the carriers involved in decay pathways to the ground state. This will allow us to produce a full kinetic model of decay described at the end of section 3.3.4. Finally, we will perform a similar analysis on catalyst 2/QD mixtures to better understand how the catalyst structure and energetics influence the overall kinetic scheme.

3.3.1. Steady-State QD PL Quenching by Catalyst 1

We first perform PL quenching experiments to observe catalyst binding and charge transfer. Upon mixing with catalyst 1, both band edge and trap emission are quenched as shown in Figure 3.3a. The quenching was calculated from the peak intensity at each ratio using the equation

$$\frac{\Delta I}{I_0} = 1 - I_q/I_0 \tag{3.2}$$

where I_0 is the intensity of the unquenched emission and I_q is the intensity of the quenched emission. Intensity of the band edge emission was calculated by fitting the spectral feature to a gaussian and taking the gaussian amplitude as a proxy for intensity. The trap emission intensity was measured directly from the spectrum at 620 nm. Both features were quenched more strongly at higher ratios of catalyst 1/QD, approaching limiting values at high ratios as shown in Figure 3.3b. The trap emission exhibits stronger quenching than the band edge emission at all ratios.

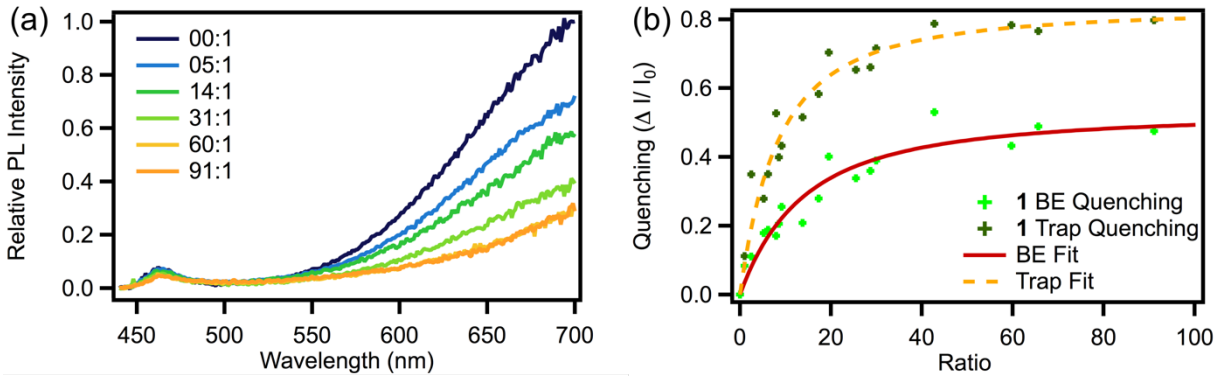

Figure 3.3 (a) Steady state PL quenching of CdS QD, by catalyst 1. The ratios indicated are catalyst 1:QD. The weak solvent background fluorescence has been subtracted from each PL scan. (b) Quenching of band edge and trap PL by catalyst 1 fit to a model accounting for catalyst binding and charge transfer efficiency. Quenching of the band edge emission was measured from (a) by spectrally fitting of the band edge emission feature, whereas quenching of the trap emission was directly determined by the intensity at 620 nm.

The quenching of the QD band edge emission by catalyst 1 is due to valence band hole transfer in competition with hole trapping, as described in Chapter 2.[41] The process leading to trap

emission quenching has not yet been studied in this system. Strong trap and band edge emission quenching has previously been observed in studies of WOCs bound to CdS nanorods.[33, 35] In both of these reports quenching of the two emission features was attributed to hole transfer from both the band edge and trap states. In both of these reports, quenching data were modeled using Langmuir adsorption isotherms and not used to extract dynamics of hole transfer from the trap state as we have previously done with the band edge emission quenching.[41]

In Chapter 2 the band edge emission quenching of CdS with catalyst 1 was described using a function which accounts for the effects of catalyst binding and competitive hole trapping in this quenching system.[41] Since this model determined an equilibrium constant for binding as well as a maximum number of catalysts that bind to the surface of the nanocrystal these parameters can be used in modelling the quenching of trap emission. Although this and other similar models[77, 97] have successfully fit the quenching of a single emission feature, they have not yet needed to account for the sequential quenching of both trap and band edge states. We now modify this model to simultaneously fit both CdS emission features.

The equation used for fitting quenching of the band edge emission is given by

$$\Phi_{HT1}(R) = \frac{(k_{HT1}/k_{tr})\left(\left(R + N + \left(K_{eq}[QD]\right)^{-1}\right) - \sqrt{\left(R + N + (K_{eq}[QD])^{-1}\right)^2 - 4RN}\right)}{2 + (k_{HT1}/k_{tr})\left(\left(R + N + \left(K_{eq}[QD]\right)^{-1}\right) - \sqrt{\left(R + N + \left(K_{eq}[QD]\right)^{-1}\right)^2 - 4RN}\right)} \quad (3.3)$$

where $\Phi_{HT1}(R)$ is the efficiency of valence band hole transfer, R is the mixing ratio, k_{HT1}/k_{tr} is the ratio of hole transfer and hole trapping rate constants, N is the maximum number of catalysts which may bind to the surface, K_{eq} is the equilibrium constant for Langmuir binding, and [QD] is the concentration of QDs. This model is still suitable to fit the band edge PL shown in Figure 3.3b but cannot be used to characterize the quenching of the trap emission due to the competition between hole transfer and trapping.

The intensity of trap emission follows the relationship

$$\mathrm{I_{Trap}} \propto \Phi_{\mathrm{Trapping}}\Phi_{\mathrm{Em}} \tag{3.4}$$

where I_{trap} is the measured intensity of trap emission, Φ_{Trapping} is the quantum efficiency of trapping, and Φ_{Em} is the quantum efficiency of trap emission. Φ_{Em} is near unity for 3-MPA coated CdS QDs, but changes upon addition of catalyst

$$\Phi_{Trapping} = (1 - \Phi_{HT1}(R)) \tag{3.5}$$

We convert this expression from an emission measurement to a quenching one using the same expression used in the derivation of (3.3)

$$\begin{aligned}\Phi_{obs}(R) &= \frac{I_{Trap}(0) - I(R)}{I_{Trap}(0)} \\ &= \frac{P_0\big(1 - \Phi_{HT1}(0)\big)\Phi_{\mathrm{Em}}(0) - P_0\big(1 - \Phi_{HT1}(R)\big)\Phi_{\mathrm{Em}}(R)}{P_0\big(1 - \Phi_{HT1}(0)\big)\Phi_{\mathrm{Em}}(0)} \\ &= \frac{\Phi_{\mathrm{Em}}(0) - \big(1 - \Phi_{HT1}(R)\big)\Phi_{\mathrm{Em}}(R)}{\Phi_{\mathrm{Em}}(0)} \\ &= 1 - \big(1 - \Phi_{HT1}(R)\big)\frac{\Phi_{\mathrm{Em}}(R)}{\Phi_{\mathrm{Em}}(0)}\end{aligned} \tag{3.6}$$

Here we use radiative and nonradiative decay pathways characterized by individual rate constants to express the quantum yield of emission

$$\Phi_{Em}(R) = \frac{k_r}{k_r + k_{nr} + k_2\langle n\rangle} \tag{3.7}$$

where k_r is the radiative rate constant, k_{nr} is the non-radiative rate constant, $\langle n\rangle$ is the average number of bound catalysts per nanocrystal, and k_2 is the per-catalyst quenching rate constant for the process which is quenching trap emission. In this model all variables with the exception of $\langle n\rangle$ are assumed to be independent of R. Before proceeding, we note that the rate constants in (3.7) are only valid descriptors for single-exponential decay processes. Trap emission is typically a highly-distributed multiexponential process,[45, 94, 98] meaning that the rate constants used in modelling the trap emission decay are approximations to the time-dependent rates which determine the overall emission yield.[99]

Combining (3.6) and (3.7) simplifies our quenching expression to

$$\begin{aligned} 1-\left(1-\Phi_{HT1}(R)\right)\frac{\Phi_{\mathrm{Em}}(R)}{\Phi_{\mathrm{Em}}(0)} &= 1-\left(1-\Phi_{HT1}(R)\right)\frac{k_r+k_{nr}}{k_r+k_{nr}+k_2\langle n\rangle} \\ &= 1-\left(1-\Phi_{HT1}(R)\right)\left(1-\Phi_2(R)\right) \\ &= \Phi_{HT1}(R)+\Phi_2(R)-\Phi_{HT1}(R)\Phi_2(R) \\ &= \Phi_{HT1}(R)+(1-\Phi_{HT1}(R))\Phi_2(R) \end{aligned} \tag{3.8}$$

where $\Phi_2(R)$ is the efficiency of trap emission quenching from the trap state. The expression has a simple interpretation in its final form: The fraction of the population which underwent hole transfer (given by Φ_{HT1}) has 100% efficient trap emission quenching, while the remainder of the population has a quenching efficiency given by $\Phi_2(R)$. As this quenching efficiency is now acting solely on the trapped hole population, we express $\Phi_2(R)$ using (3.3) to produce our quenching model

$$\Phi_{\mathrm{obs}}(\mathrm{R}) = \Phi_{\mathrm{HT1}}(\mathrm{R}) + \frac{(1-\Phi_{\mathrm{HT1}}(\mathrm{R}))\,(\mathrm{k_2/k_0})\left(\left(\mathrm{R+N+(K_{eq}[QD])^{-1}}\right)-\sqrt{\left(\mathrm{R+N+(K_{eq}[QD])^{-1}}\right)^2-4\mathrm{RN}}\right)}{2+(\mathrm{k_2/k_0})\left(\left(\mathrm{R+N+(K_{eq}[QD])^{-1}}\right)-\sqrt{\left(\mathrm{R+N+(K_{eq}[QD])^{-1}}\right)^2-4\mathrm{RN}}\right)} \tag{3.9}$$

Having derived models to fit quenching from either emission feature we apply equations (3.3) and (3.9) to fit the quenching of the band edge and trap emission as shown in Figure 3.3b. The catalyst binding to the QD surface is described in this model by N (the maximum number of catalysts which may bind to the surface) and K_{eq} (the equilibrium constant for Langmuir binding). These parameters should be identical for quenching of both emission features by catalyst 1, as they are determined by the thermodynamics of catalyst binding and not the nature of the excited state. The two emission features correspond to two different electronic states, so we allow for two different quenching efficiency parameters k_{HT1}/k_{tr} and k_2/k_0. To our knowledge, this is the first report of simultaneous fitting of both nanocrystal emission features with a single set of binding parameters.

The binding parameters found by globally fitting the trap and band edge quenching of catalyst 1 give N=23 ± 10 and K_{eq}=1.2 ± 0.4 × 10^6 M^{-1}, while the quenching efficiency parameters

are k_{HT1}/k_{tr}=0.045 ± 0.027 and k_2/k_0=0.073 ± 0.04. The quenching results for the band edge are within error of the values found in the previous report, although the uncertainty for each value is significantly larger.[41] This uncertainty is caused by greater noise in the data, which is a biproduct of lower sample concentrations and using a fluorometer with a higher noise floor for these measurements.

The fit parameters obtained from this data are within error of those measured in the previous report, but the quenching of the band edge is clearly different upon inspection of the data. This difference is manifested in the asymptotic behavior of the quenching at high catalyst loading, which approaches 51% in Figure 3.3b while the maximum achievable quenching reported in Chapter 2 was 37%.[41] This change could be explained by changes to either N or k_{HT1}/k_{tr}, but not by changes in K_{eq} as in the high ratio limit every site is occupied regardless of the equilibrium constant. The value of N from the fit (N=23) was almost unchanged from the value found in Chapter 2 (N=21). The difference then is likely due to a change in k_{HT1}/k_{tr} between samples, indicating faster hole transfer or slower hole trapping for this sample. To evaluate this, we measured the hole trapping rate k_{tr} for a CdS sample using PL upconversion, visible TA, and NIR TA. These techniques have each been used previously to measure the hole trapping time in cadmium chalcogenide nanocrystals.[41, 66, 100-101] Using all three techniques provides further confidence that we have a value which is reflective of the hole trapping time without interference from other kinetic factors. The value for hole trapping we obtained from fitting these data was 0.320 ± 0.015 ps, or a rate of $3.1 \pm 0.3 \times 10^{12}$ s^{-1}. Combining this with our value of k_{HT1}/k_{tr} results in a k_{HT1} value of $1.4 \pm 0.86 \times 10^{11}$ s^{-1}. This value is consistent with our previously observed value of $1.3 \pm 0.2 \times 10^{11}$ s^{-1}, meaning that the stronger band-edge quenching observed here is entirely due to changes in the trapping time.

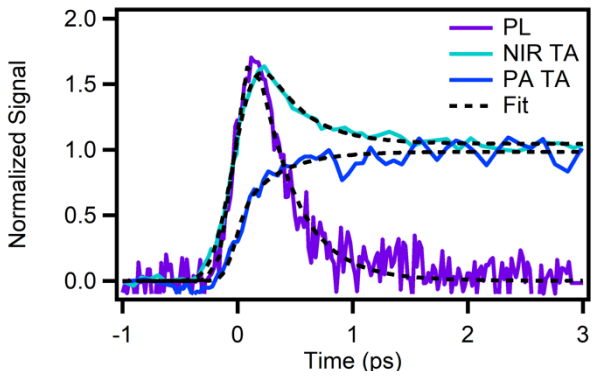

Figure 3.4 Hole trapping time constant measurement from PL upconversion, NIR TA, and TA of the broadband photoinduced absorption (PA) feature. All scans were obtained using a 440 nm excitation wavelength. PL upconversion kinetics were averaged across the observable emission feature (460-480 nm) and fit to a single exponential convoluted with the instrument response function (IRF). The PA feature was averaged from 550-700 and fit with an exponential rise convoluted with the IRF. The NIR TA feature was averaged from 1350-1450 and fit to a single exponential with a y-offset convoluted with the IRF.

Fitting of the trap emission gives a value of k_2/k_0 of 0.073 ± 0.04, which corresponds to a maximum achievable trap quenching of 63% upon saturation of the surface with CdS QDs. When combined with the static quenching contribution of the band edge, we find the maximum quenching as the asymptotic behavior of equation (3.9)

$$\Phi_{obs}(\infty) = 0.51 + (1 - 0.51) \times \frac{k_2/k_0\, N_{max}}{1 + k_2/k_0\, N_{max}} = 0.51 + 0.51 \times 0.63 \qquad (3.10)$$

which results in 83% total quenching of the trap emission, as reflected in Figure 3.3b.

Although k_2/k_0 proves to be a useful parameter for fitting the trap emission, the meaning of this quantity is unclear from the quenching experiment. More information on the decay of trap emission and the timescale of emission quenching by the catalyst is required to determine the physical process which leads to k_2 quenching and the implications of this quenching for catalysis. We now turn to time-resolved PL measurements to further characterize decay through the trapped-hole pathway.

3.3.2. TCSPC Kinetics of Catalyst 1

As PL reflects the process of two-carrier radiative recombination, its dynamics are determined by the shorter-lived carrier, either the electron or the hole. CdS QDs with 3-MPA ligands, the decay of the band edge emission is instrument limited in TCSPC due to sub-picosecond hole trapping. The lifetime of the trap emission feature is much longer, and TCSPC has been used previously to study trapped hole dynamics in several cadmium chalcogenide nanostructures.[45, 94, 102-103]

The spectra and kinetics of trap emission from cadmium chalcogenide nanostructures are subjects of active research[94, 102, 104-106] and both must be carefully characterized for CdS QDs before interpretation of the quenched data. To do so we performed a time-resolved emission scan (TRES) of the QD trap emission by measuring the kinetics of emission at 30 nm intervals across the emission spectrum. This generates a 2-dimensional array containing spectral and kinetic information of the trap emission decay. To examine the spectral evolution of the trap emission for QDs, the dataset was binned into logarithmically spaced time intervals and averaged, resulting in the spectra shown in Figure 3.5a. The emission begins with a strong and broad feature which appears to both decay and shift in the first 5-10 nanoseconds of observation. This behavior is not novel, and has been assigned to several different root causes, including emission from both electron and hole traps,[94] and diffusion of holes from high to low energy trap states.[107]

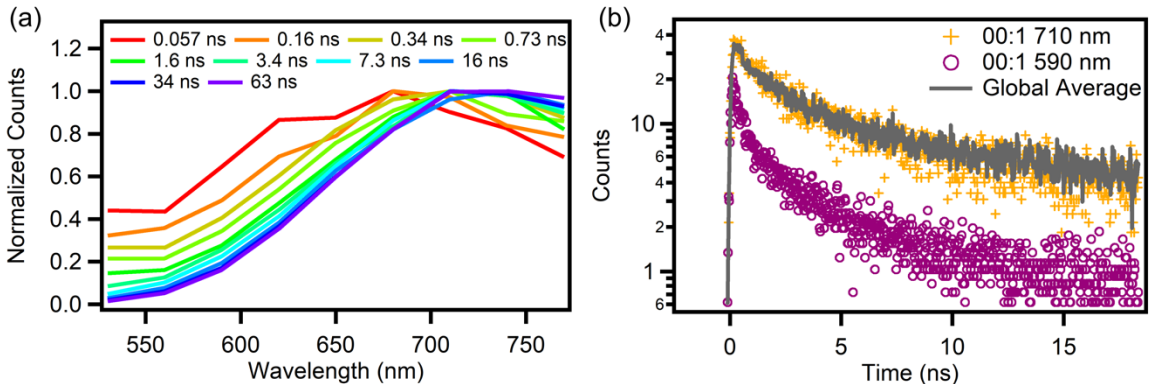

Figure 3.5 (a) TRES of CdS QD showing shifting and narrowing occurring during decay. The spectra shown here were rebinned from linearly spaced time-points (26 ps/bin) to the times indicated in the legend and normalized to the peak. (b) Kinetics of the trap emission at 590 nm and 710 compared to the amplitude of a gaussian spectral global fit.

The spectral dynamics observed in the TRES of the trap emission may lead to wavelength specific quenching of the steady-state emission, depending on the mechanism of spectral shifting and timescale of quenching. For example, addition of a quenching pathway with kinetics slower than the spectral shifting would lead to preferential quenching of the red-shifted emission and result in a blue shift of the steady state spectrum at all mixing ratios. In Figure 3.3 there is not a significant shift of the trap emission upon addition of quencher, leading us to conclude that the QD spectral dynamics observed in TCSPC are of secondary importance for understanding the quenching mechanism. It is therefore desirable to separate the kinetics of the electron-hole recombination from those due to spectral shifting. To achieve this, we performed a spectral global fit of the complete TRES data set to a single gaussian peak at each time point using the function

$$I(\lambda, t) = A(t) \times \exp\left(-\frac{\left(\lambda - \lambda_0(t)\right)^2}{w(t)^2}\right) \tag{3.11}$$

where t is time, λ is the wavelength, A(t) is the amplitude, $\lambda_0(t)$ is the center wavelength of the spectrum, and w(t) is the width of the feature. By fitting these data, we were able to observe how the amplitude A(t) of the peak changed over the course of the PL decay. The results of this fit are included in Figure 3.5b. The trap emission amplitude exhibits nearly identical kinetics to those observed at 710 nm. We note this as a useful observation which can be leveraged to extract the decay of the entire trap emission feature in a single, rapid TCSPC experiment rather than through acquisition of the whole spectrum.

Figure 3.6 shows change in the decay kinetics of the trap PL amplitude upon addition of catalyst 1. Catalyst quenching leads to faster trap emission decay at early times, after which the kinetics match those of the CdS QDs. This represents a more complex quenching behavior than

observed in quenching of the band edge emission.[41] The lack of quenching following the initial decay suggests that the quenching is limited by some internal process, such as a population transfer between a quenched and unquenched emissive state.

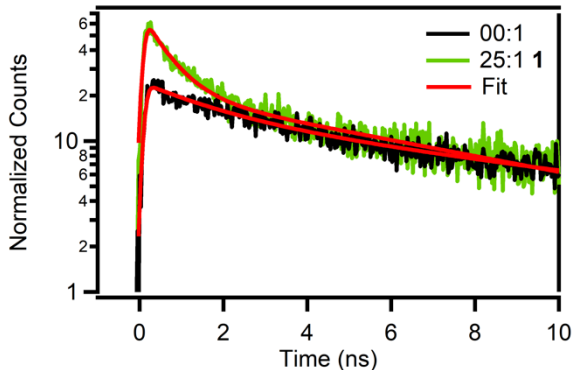

Figure 3.6 Kinetics of trap emission from samples containing QDs and a 25:1 ratio of catalyst 1/QD. Kinetics have been normalized to highlight their similarity at late times. The data are fit to multiexponential decay functions convoluted with the TCSPC IRF.

The TCSPC and steady state results suggest that quenching of QD emission by catalyst 1 occurs on a sub-nanosecond timescale with the quenching efficiency increasing at higher catalyst loadings. The majority of quenching appears to occur in the first nanoseconds of decay, after which the kinetics resemble those of CdS QDs without catalyst. Having determined the timescale of quenching, it is now important to identify the carriers which are affected by addition of catalyst 1. To resolve the process involved in PL quenching we will compare these kinetics to TA kinetics.

3.3.3. TA Spectra and Kinetics of CdS + Catalyst 1

We utilize TA to examine the effects of these catalysts on the QD conduction band electron lifetime. The bleach signal of the first exciton peak of the QD is a direct reporter of electron population in the conduction band, making TA a reliable technique to directly measure electron kinetics.[39] Because of this strong electron signal, TA can be used in conjunction with TCSPC to separate hole and electron dynamics for cadmium chalcogenide nanocrystals.[45, 52] TA can also be used to study the excited state behavior of ruthenium-based catalysts.[108] The absorption spectrum

of ruthenium complexes are impacted by the oxidation state which allows for direct observation of photoinduced charge transfer.[11, 33, 91, 109]

To aid in our interpretation of the TA spectra with catalyst 1 present, we begin by characterizing changes in the catalyst absorption features due to oxidation or reduction using spectroelectrochemistry. This experiment allows us to observe changes in the catalyst absorption spectrum upon creation of the one electron oxidized or reduced species, as shown in Figure 3.7. Upon applying a 1.4 V potential to the sample cell we observed changes due to oxidation of the ruthenium complex. In the visible region of the spectrum, the primary effect was a bleaching of the MLCT transition. The spectrum obtained through reductive spectroelectrochemistry at -1.0 V was distinct from the oxidative spectrum. Reduction leads to broadening of the MLCT transition with isosbestic points at 514 and 546 nm. The changes following either reduction or oxidation of catalyst 1 resemble those reported previously for other ruthenium polypyridine complexes.[11, 91] Photoinduced charge transfer from the QD to catalyst 1 should contain spectral signatures similar to Figure 3.7c as well as contributions from the excited QD.

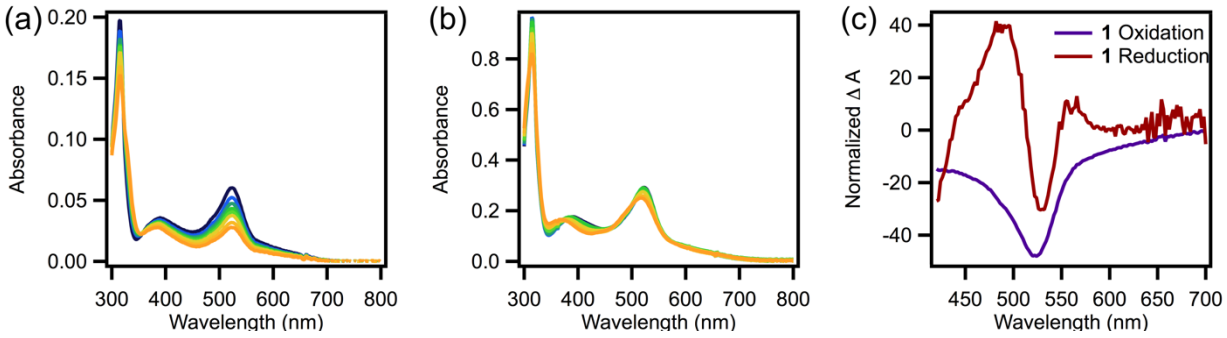

Figure 3.7 (a) Oxidative spectroelectrochemistry of catalyst 1 in acetonitrile. Blue spectra are the initially acquired spectra and yellow are following over time following application of a 1.4 V potential vs NHE. (b) Reductive spectroelectrochemistry of catalyst 1. Blue spectra are the initially acquired spectra and yellow are following application of a -1.0 V potential vs NHE. (c) Difference spectra following reduction or oxidation, showing the relative change in absorbance features.

We turn now to TA on the QD and catalyst 1/QD mixtures shown in Figure 3.8. The TA spectrum of the nanocrystal following excitation at 440 nm exhibits a strong bleach of the first band edge transition combined with a broad and weak photoinduced absorption feature from 500 to 700 nm. These features are well known to originate from conduction band electrons and trapped holes, respectively and strongly resemble the TA spectra of CdS QD obtained in Chapter 2.[39, 41, 75, 110] Addition of catalyst 1 leads to the appearance of several new features in the TA spectra. A bleach feature appears in the picosecond spectra of the catalyst/nanocrystal mixture at the wavelengths of the lowest energy MLCT transition of the catalyst. This spectrum was a reasonable match to the changes observed in the oxidative spectroelectrochemistry of the catalyst, suggesting that the bleach in the picosecond TA spectrum of samples containing catalyst is partially due to the oxidation of the catalysts with photoexcited holes from the CdS valence band. It must be noted however that direct photoexcitation of the catalyst MLCT produces a similar looking spectrum.

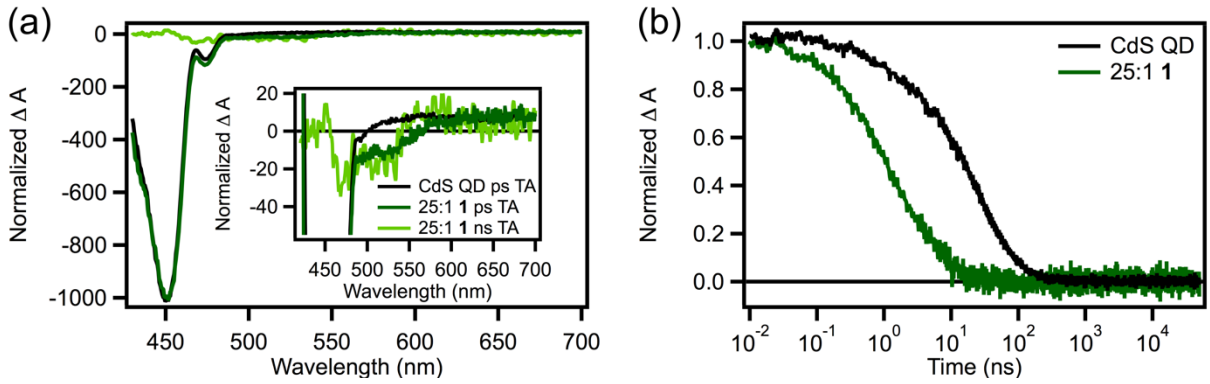

Figure 3.8 (a) TA spectra of CdS QD and 25:1 catalyst 1/QD in two time windows. The picosecond spectra are averaged from 10 to 20 ps while the nanosecond spectrum was taken by averaging TA spectra from 20 to 500 ns. Inset: Zoom-in view of (a), showing the changes in the region of the catalyst MLCT absorption. (b) TA kinetics of the QD bleach showing faster decay upon addition of catalyst 1. All kinetics were taken at 456 nm.

At later times another spectral feature grew in during the decay of the nanocrystal bleach in samples containing catalyst 1. This feature persisted for microseconds, much longer than any signal present in QD samples. This long-lived feature resembles two gaussian derivatives with

zero crossings at 456 and 544 nm. The latter wavelength is very close to one of the zero crossing points observed in the reductive spectroelectrochemistry of catalyst 1, suggesting that the late time TA spectrum of the catalyst 1/QD mixture contains signals of a reduced catalyst. The other derivative like feature in the TA spectrum occurs near the 1S maximum of the QDs. Similar derivative-like features have been reported for CdS nanorods following electron transfer and are attributed to a stark shift of the 1S transition by the reduced electron acceptor.[110] Taken together, this suggests that the TA spectrum of the catalyst 1/QD mixture at later times is due to electron transfer from the conduction band to catalyst 1.[110]

Having described the spectral features of the TA data we now examine the TA kinetics. Figure 3.8b shows nanocrystal band edge bleach kinetics reported at 456 nm. This wavelength was chosen as an isosbestic point of the nanosecond spectra with catalyst 1 to remove kinetics of the derivative feature. Upon addition of catalyst 1 to solution the decay of the band edge electron accelerates, a trend also seen in the analogous CdS NR-ethyl ester catalyst system.[35] The timescale of this decay indicates the creation of a new electron transfer or recombination process on the same timescale seen in the TCSPC decay of catalyst 1/QD samples.

We find that the late-time feature observed in the spectra appears to rise on the same timescale in which the band edge begins to decay. This is seen more clearly when the kinetic signal from the late-times feature is averaged between 540 and 600 nm, the positive peak seen in Figure 3.8. The kinetics of its rise are similar to the initial decay of the band edge bleach as shown in Figure 3.9.

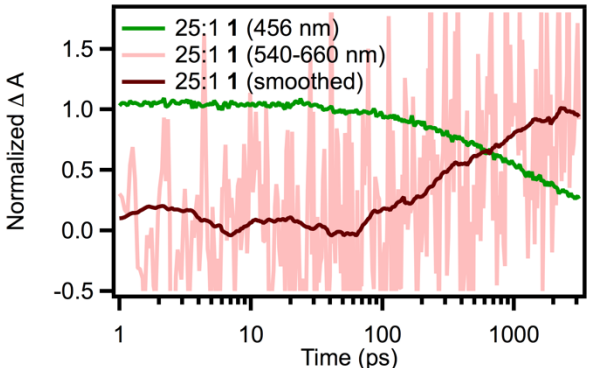

Figure 3.9 Rise of the TA signal of the reduced catalyst (averaged from 540-660 nm) and decay of the band edge electron signal (456 nm)

The spectral signatures of a reduced catalyst combined with the observation that this feature rises in with the decay of the QD bleach strongly suggest that electron transfer to the catalyst is a dominant decay pathway for the photoexcited electron. Using a combination of fitting and analysis of the kinetic data, we will now determine the impact of this pathway on the kinetics of the TCSPC and construct a kinetic model to describe the sum total of decay processes in the system.

3.3.4. Summary and Construction of Kinetic Model for CdS Catalyst 1/QD

We will begin combining our observations from absorption and PL data by comparing the kinetics of CdS PL and TA decay from Figure 3.6 and Figure 3.8. Decay of both trap emission and the QD bleach can be fit using a multiexponential decay function convoluted with the instrument response function

$$I(t) = IRF \otimes \sum_{i=1}^{n} a_i \exp\left(-\frac{t}{\tau_i}\right) \tag{3.12}$$

with time constants given in Table 1. The TA bleach decays more slowly than the trap emission for the initial part of the decay, but the kinetics of the two measurements match following this initial process as shown in Figure 3.10. The match between TA and trap PL kinetics at later times leads us to conclude the kinetics at these times are due to recombination of the trapped hole with

a conduction band electron. The origin of the faster decay in the TA and TCSPC is less clear. Prior work has assigned this initial decay to hole transfer from surface traps to bound thiol ligands.[45]

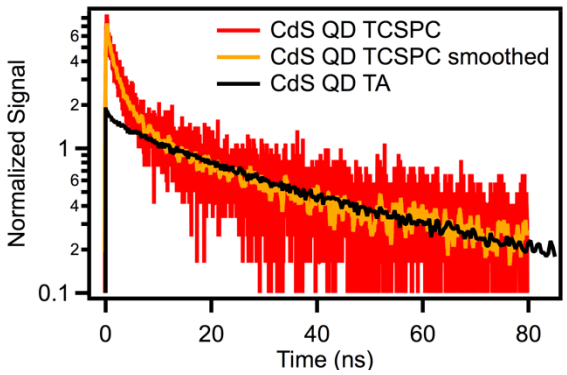

Figure 3.10 TCSPC (710 nm), smoothed TCSPC data, and TA kinetics (456 nm) of CdS QDs, normalized to highlight the similarity of the decay at late times.

Table 1 Fit parameters from multiexponential fits to TA and TCSPC kinetic data

	CdS TCSPC	CdS TA	25:1 TCSPC	25:1 TA
a_1	0.55±0.025	0.14±0.007	0.60±0.012	0.54±0.013
τ_1 (ns)	1.00±0.075	1.00±0.078	0.46±0.02	0.64±0.024
a_2	0.33±0.025	0.37±0.040	0.29±0.010	0.45±0.013
τ_2 (ns)	4.9±0.383	14.2±1.5	3.3±0.125	5.55±0.18
a_3	0.124±0.005	0.49±0.045	0.099±0.002	—
τ_3 (ns)	50±2.3	53.1±3.5	39.4±0.934	—

Electron transfer may or may not cause quenching of the trap emission depending on whether it primarily occurred in the population with a trapped hole or a transferred hole. If the change in decay time in the TCSPC decay is similar to the electron transfer time in the TA decay, that will be a strong indication that the process is identical. The distinct TA and TCSPC decays mean that direct comparison of the kinetics will not work, and that the process must be considered individually for each measurement before comparison.

We will begin by estimating the order of magnitude of k_2 and k_0 from the TA decay, assuming that k_2 corresponds to electron tr. The lifetime of the initial TA decay is 0.64 ± 0.024 ns. This produces an upper bound of $(k_2 \times \langle N \rangle) \leq 1.6 \pm 0.06 \times 10^9\ s^{-1}$, where <N> is the number of bound catalysts. Using the equilibrium constants calculated from the quenching experiments, we

estimate that 22 ± 9 catalysts are bound in the TA experiment with catalyst 1. This means that $k_2 \leq 7.1 \pm 3 \times 10^7$ s^{-1} per catalyst bound. The quenching model we used earlier found a value of k_2/k_0 of 0.073 ± 0.04 per catalyst for the trap emission quenching. Treating the quenching of trap emission as a simple competition between single exponential processes with time constants k_2 and k_0, this implies that $k_0 \leq 1 \pm 0.6 \times 10^9$ s^{-1}. This number matches the fastest decay component observed in the QD TA and TCSPC although the uncertainty is relatively large. We had previously observed that the trap emission quenching in TCSPC had a substantial effect for the initial few nanoseconds of decay, after which the kinetics matched. The value of k_0 occurring on this timescale independent of our TCSPC observations suggests that the process which is depletes the trap emission on a nanosecond timescale is also in some way limiting electron transfer from nanocrystal to catalyst.

Having isolated the timescale of k_0, we now determine if the timescale of k_2 measured in TA matches the lifetime shortening of TCSPC. At the concentration used for the 25:1 TCSPC Sample, 16 ± 5 catalysts are bound per nanocrystal. Using the value for k_2 calculated from the TA data, we would expect this to result in an additional decay component with a rate $(k_2 \times \langle N \rangle) \leq 1.2 \pm 0.6 \times 10^9$ s^{-1}. This decay competes with the decay k_0, resulting in a total decay constant of $2.2 \pm 0.9 \times 10^9$ s^{-1}. This results in a time constant of 0.46 ns, which is an excellent match to what was observed in the TCSPC measurement. This leads us to conclude that the quenching of the trap emission is indeed due to electron transfer.

Previous reports on charge transfer between Ru polypyridyl complexes and CdS nanostructures disregarded the possibility of trap emission quenching through electron transfer based on the energy level alignment between nanocrystal and catalyst.[33, 35] The energetics of the catalyst as we have calculated in Figure 3.2a should disfavor electron transfer due to a difference

of 70 meV between the LUMO of catalyst 1 and the CB of the QD. There are several factors which could generate inaccuracy in our estimated driving force and enable electron transfer. QD heterogeneity could lead to a subpopulation with a higher LUMO capable of photoinduced electron transfer, although the UV-Visible and TEM data do not seem to show a subpopulation with a small enough diameters to allow this. It could be that the measured potentials of catalyst 1 from Figure 3.2a are altered by changing the solvent from acetonitrile to methanol, enabling electron transfer, although this is not typically the case for coordinatively saturated complexes[111]. Alternatively, it could be that the interaction between catalyst and QD leads to a sufficient shift in catalyst or nanocrystal energetics to enable electron transfer. Work from Kilina et al.[112] has previously shown that interactions with a surface can provide a substantial perturbation on the energetics of ruthenium complexes, which could lead to the change in catalyst LUMO with no corresponding change in the absorption spectrum. Free metal ions have also been shown to perturb the energy levels of ruthenium complexes in solution in a way that does not significantly alter the absorption spectra.[113] Cd^{2+} ions have been shown to dissociate from QDs with surface ligands,[114] which could lead to shifting in the catalyst energy levels through association with the complex. Finally, we hypothesize that the presence of the trapped hole on the surface near the catalyst could stark-shift the catalyst energy levels and enable an electron transfer pathway.

Trap PL quenching is not sensitive to the population of nanocrystals which transferred holes to catalyst 1 on a picosecond timescale and cannot report whether this population also performs electron transfer to the catalyst. TA is sensitive to this population however, as nanocrystals which have transferred a hole to the catalyst still contain an electron in their conduction band. Examining the fit to the TA from Table 1, we find that only 55% of the TA decay is occurring on the 640 ps timescale for a 25:1 ratio of catalyst 1. The remaining 45% of the

nanocrystals decay with a lifetime of 5.5 ns. Based on the PL quenching data, approximately 50% of nanocrystals should decay through the hole transfer pathway, so the amplitudes of these exponential decays suggest that they correspond to the trapped hole and transferred hole populations. As we have already shown that the 640 ps component corresponds to the accelerated TCSPC kinetics and therefore the trapped hole pathway, we assign the other pathway to recombination of the transferred hole with a conduction band electron. The measured lifetime gives this process a rate constant of 1.8×10^8 s^{-1}. We do not anticipate the rate at which this state returns to the ground state to be significantly affected by catalyst loading, as the recombination mechanism should only involve the QD and oxidized catalyst, with little contribution from the adsorbed ground state catalysts.

The decay of the reduced catalyst state observed in TA is much slower than every other process observed in this system, as shown in Figure 3.11. This suggests that electronic communication between the reduced catalyst and the trapped hole is limited, most likely by the poor overlap between these spatially localized states. The recombination is then limited by the mobility of the carriers to explore the QD surface and reunite. Recently, it was shown that trapped holes are able to diffuse on the surface of Cd-chalcogenide nanocrystals by hopping between surface chalcogenide atoms.[57, 71, 100, 115] This behavior is typically not observed in the TA spectra of QDs because the conduction band electron has equal overlap with all points on the surface so the hopping of the hole from surface trap to trap has no effect on the electron–hole recombination.[57] This changes upon electron transfer to a bound catalyst on the surface of the particle, which allows the motion of the hole closer or further from the reduced catalyst to modulate the carrier recombination time. Decay of the reduced catalyst state can be modeled as trapped-hole diffusional recombination.

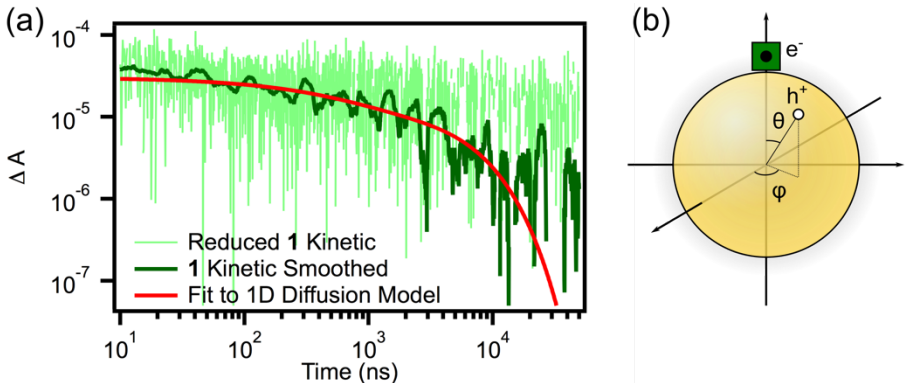

Figure 3.11 (a) Decay of the TA signal of the reduced catalyst through trapped-hole diffusion-limited recombination. TA kinetics were averaged from 550-570 nm to isolate the reduced catalyst decay (see Figure 3.8). The fit to the data uses a multiexponential model for diffusion limited recombination derived below. (b) Illustration of coordinate system used in the derivation of a model of the recombination kinetics of a stationary reduced catalyst with a mobile trapped hole.

To model the kinetics of this recombination mechanism, we assume that the trapped hole undergoes diffusion while the reduced catalyst remains stationary on the timescale of the measurement and that neither species decay by other mechanisms. In this model, the hole traverses the two-dimensional surface of the QD until it encounters the reduced catalyst and recombines. We define the coordinate system such that the reduced catalyst is located at the polar angle $\theta = 0$. The trapped hole starts at an initial polar angle θ_0. To simplify the dimensionality of the problem, we assume that motion of the hole in the azimuthal direction (φ) is independent from motion from the polar direction, in which case diffusion in the azimuthal direction has no effect on recombination and can be neglected. In this case, the survival probability of the reduced catalyst is equivalent to the solved problem of one-dimensional diffusion–annihilation on a finite half-line[57, 116]

$$S(t) = \sum_{n=0}^{\infty} \frac{2\sin[(n+1/2)\theta_0]}{(n+1/2)\pi} e^{-(n+1/2)^2\pi^2 t/\tau}, \tag{3.13}$$

where $\tau = \pi^2 r^2/D$ and r is the radius of the QD. In the ensemble there will be a distribution in the initial positions of the trapped holes, $p(\theta_0)$.[57] We approximate this initial distribution to be flat

and centered symmetrically around the reduced catalyst; that is, $p(\theta_0)$ is uniform on $0 < \theta_0 < \theta_{\max}$, where $\theta_{\max} \leq \pi$, and has no φ dependence. Integrating the survival probability in (3.13) over this initial distribution gives the ensemble survival probability for reduced catalysts[57]

$$S(t) = \frac{4\pi}{\theta_{\max}} \sum_{n=0}^{\infty} \frac{\sin^2[(n+1/2)\theta_{\max}/2]}{(n+1/2)^2\pi^2} e^{-(n+1/2)^2\pi^2 t/\tau}. \quad (3.14)$$

The decay of the reduced catalyst was fit to a sum of the first 10 terms of (3.14), which achieved convergence throughout the experimental time window. The resulting fit parameters τ = 14 ± 7 μs, and $\theta_{\max}$ = 77 ± 24° (Figure 3.11). The diffusion coefficient can be obtained from τ and r (5.4 nm) to give D = 5.0 ± 2.4 × 10^{-8} cm^2 s^{-1}. This value is comparable to previous reports for the diffusion coefficient for trapped holes on a CdS surface in the direction of the wurtzite c-axis, which was bounded from above by 10^{-7} cm^2 s^{-1}.[57] The result for $\theta_{\max}$ being smaller than 180° suggests that electron transfer is more likely to occur from the photoexcited QD to catalyst 1 if the hole is trapped nearby. The mechanism which causes preferential electron transfer to catalysts near the trapped hole is unclear but could be due to a shift in the energy levels of the QD or catalyst by the adjacent trapped hole. This could also explain why electron transfer occurs despite our calculations showing unfavorable electron transfer driving force.

A summary of the decay processes for catalyst 1 bound to CdS QD is shown in Figure 3.12. This kinetic model combines results from all experiments performed on catalyst 1, and includes 5 kinetic pathways: valence band hole transfer, hole trapping, electron transfer, trapped hole/conduction band electron recombination, transferred hole/conduction band electron recombination, and diffusional transferred-electron/trapped-hole recombination. We note that this is intended as a minimal model to explain the diverse measurements acquired on this system. Additional techniques which more accurately account for the trap emission may lead to additional insights about the electron transfer and recombination processes.

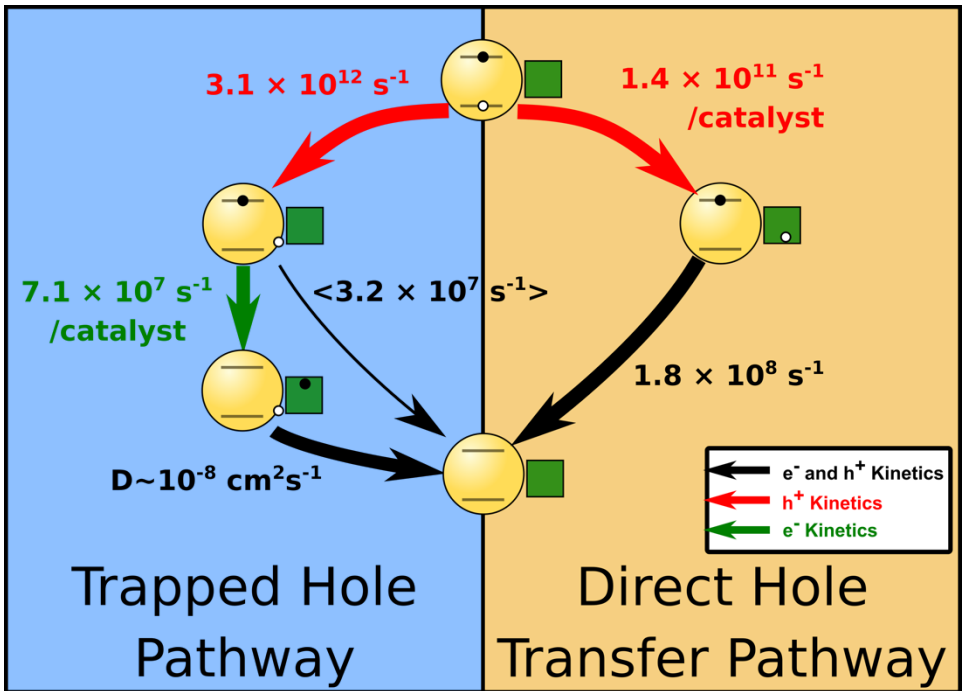

Figure 3.12: Kinetic scheme for the decay of catalyst 1/QD mixture. The arrows (in descending order by associated constant) indicate hole trapping, valence band hole transfer to catalyst 1, recombination of the transferred hole, electron transfer to catalyst 1, trapped hole recombination, and trapped-hole diffusional recombination with a reduced catalyst. The width of the arrows indicate the efficiency of each process for high-loading conditions. Angled brackets indicate an average rate constant.

Having determined the mechanism for decay of catalyst 1 using a series of spectroscopic techniques, we elected to test the methods and modelling required to produce a kinetic scheme for catalyst 1 on catalyst 2. The energy level diagram in Figure 3.2 showed that the catalyst 2 LUMO is 300 meV higher in energy than catalyst 1. The larger energy offset between the QD conduction band and catalyst 2 LUMO should make electron transfer from the QD far less favorable. Catalyst 2 also has more driving force for hole transfer than catalyst 1 which may improve the efficiency of reaching the direct hole transfer pathway. This will serve as an investigation of a hitherto unexplored system as well an opportunity to test procedures developed in the analysis of catalyst 1.

3.3.5. Decay Pathways and Kinetics of Catalyst 2

We begin our study of catalyst 2 in a similar fashion to catalyst 1, by examining its PL quenching behavior as shown in Figure 3.13. Catalyst 2 exhibits almost identical band edge quenching as observed with catalyst 1. We additionally see quenching of the trap emission, although it does not seem to be as strongly quenched as was observed with catalyst 1. There are also changes in the emission spectrum of the catalyst 2/QD mixture, with an increase in intensity on the red edge of the spectrum. Upon increased catalyst loading a second emission feature grows in, which strongly resembles the emission from catalyst 2 as shown in Figure 3.2.

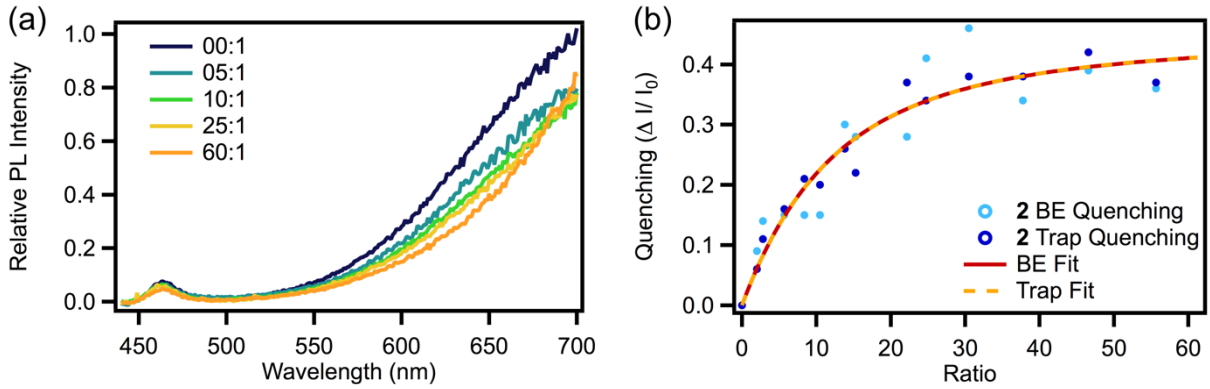

Figure 3.13 (a) Steady state PL quenching of CdS QD, by catalyst 2. The ratios indicated are catalyst2:QD. (b) Quenching of band edge and Trap PL by catalyst 2 fit to the model used in fitting of Figure 3.3.

The simplest explanation for the appearance of this catalyst-like emission feature is that the catalyst is partially absorbing the excitation light leading to phosphorescence. However, the weak absorption of the catalyst at the excitation wavelength leads us to consider other possible excitation mechanisms such as energy transfer from a photoexcited nanocrystal to catalyst 2. One approach which could distinguish direct excitation from energy transfer is to perform an excitation scan monitoring the catalyst emission feature as a function of excitation wavelength to determine if exciting the nanocrystal generated catalyst 2 emission. This simple approach is not effective though due to the overlap between the trap emission and catalyst 2 emission peaks. To account for

this, we performed a 2D excitation/emission scan of a catalyst 2/QD mixture, acquiring a PL spectrum at many different excitation wavelengths. Several of the emission scans acquired in this way are shown in Figure 3.14a. The emission scans showed a dependence of emission on excitation wavelength, ranging from spectra resembling catalyst 2 emission to emission resembling a linear combination of catalyst and trap emission. This suggested that the true excitation spectra could be extracted using a spectral global fit to the emission spectra, using the catalyst and QD trap emission spectra as a basis set

$$I(\lambda_{ex}, \lambda_{em}) = a_1(\lambda_{ex}) \times Trap(\lambda_{em}) + a_2(\lambda_{ex}) \times Catalyst(\lambda_{em}) \quad (3.15)$$

where a_1 and a_2 are extracted excitation spectra of the two features, Trap(λ_{em}) is the spectrum of the trap emission, and Catalyst(λ_{em}) is the emission spectrum of catalyst 2. The results of this fit are shown in Figure 3.14b.

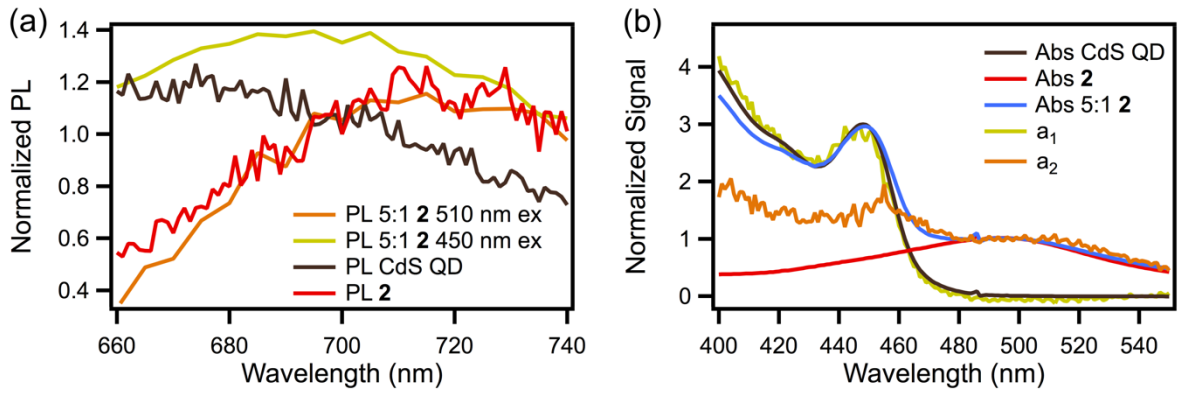

Figure 3.14 (a) Emission scans of QD, catalyst 2, and their mixture when exciting at 2 different wavelengths. (b) UV-Vis and PLE scans of QD, catalyst 2, and a 5:1 mixture. The PLE scans were achieved through global fitting of a 2D excitation/emission scan using the emission spectra of QD and catalyst 2 shown in the left frame. PLE were converted to a logarithmic y-scale before being normalized.

The PLE data extracted from this fit are straightforward to interpret. The excitation spectrum of the trap emission is almost identical to the absorption spectrum of the nanocrystal indicating that excitation of the nanocrystal leads to trap emission while excitation of the catalyst does not. The excitation scan of the catalyst 2 emission did not match the absorption spectrum of

catalyst 2 but appeared to have features due to both catalyst and nanocrystal. This indicates that excitation of the nanocrystal leads to catalyst emission, which is a signature of energy transfer.

Having determined the mechanism of catalyst-like emission as energy transfer from the nanocrystal to catalyst 2, we now return to its trap emission quenching behavior. Catalyst 2 does not have a significant amount of emission at 620 nm, which allows us to quantify the quenching of the trap emission shown in Figure 3.13b. Unlike catalyst 1, the quenching of the trap emission by catalyst 2 appears to match the band edge emission quenching very closely. As the additional trap quenching above band edge quenching was shown to correspond to electron transfer in catalyst 1, this appears to suggest that the higher LUMO in catalyst 2 was successful in discouraging electron transfer.

Performing global fits of equations (3.3) and (3.9) to the trap and band edge quenching data for catalyst 2 are shown in Figure 3.13b. These fit parameters are k_{HT1}/k_{Tr}=0.042 ± 0.027, K_{eq}= 1.6 ± 0.6 ×10^6 M^{-1}, N= 18 ± 8, and k_2/k_0=0 ± 1 × 10^{-3}. These results once again indicate strong binding interactions between catalyst 2 and the QD with fast transfer of the photoexcited band edge hole to catalyst 2 competing successfully with trapping.

The values obtained for the band edge fit are very close to the corresponding parameters in catalyst 1. Both catalysts have similar binding parameters with the QD, which suggests that the ester group of catalyst 1 is not participating in the binding. Further study of this binding mechanism is undertaken in Chapter 4.

Trap emission quenching effectiveness is the parameter which changed the most in our analysis of the quenching from catalyst 1 and catalyst 2. The similarity of band edge quenching but striking difference in trap quenching between the two catalysts validates our model of trap emission as having contributions from both removal of the valence band hole and direct quenching

of the trap emission. This also verifies that electron transfer to the catalyst has been successfully deactivated by increasing the energy of the LUMO. We now transition to examining the decay kinetics of catalyst 2 using TCSPC and TA, which should offer further confirmation of the removal of the electron transfer pathway.

3.3.6. TCSPC and TA Kinetics of Catalyst 2

The quenching of QD band edge and trap emission by catalyst 2 appears to be sufficiently described by removal of the band edge holes without any additional change in the trapped hole population. However, energy transfer from the photoexcited QD to catalyst 2 should lead to additional PL quenching as it introduces a new path for the excited system to reach the ground state. To look for evidence of quenching due to energy transfer, we returned to time-resolved emission measurements. We recorded TRES of a 20:1 catalyst 2 mixture and compared it to the CdS TRES as shown in Figure 3.15. The kinetics for this sample appear unchanged, as expected from the near identical quenching of band edge and trap emission observed in the steady state data. However, the spectra acquired for this experiment sample exhibit the same catalyst 2 emission feature seen in the steady state.

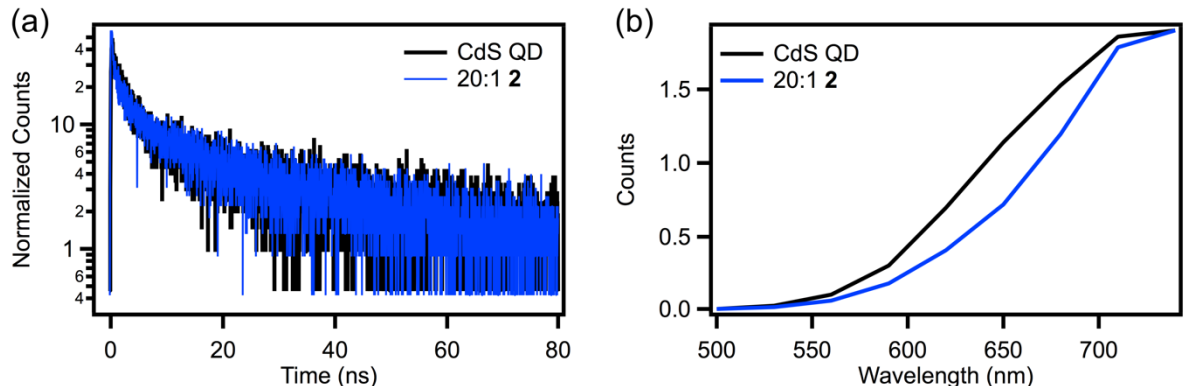

Figure 3.15 (a) TCSPC decay of the trap emission of QD and 20:1 catalyst 2/QD mixture measured at 710 nm. (b) TRES of these samples averaged from 45 to 55 ns. Due to energy transfer, the emission of the Catalyst 2/QD mixture resembles emission from the catalyst rather than the nanocrystal.

Based on the quenching and kinetics, the pathway which transfers excitation from the nanocrystal to the catalyst must be slower than the intrinsic decay pathways of the QD, as fast pathways would lead to acceleration of the TCSPC decay kinetics. The only way in which a slow energy transfer pathway can result in predominantly catalyst 2 emission is if the catalyst has a higher quantum yield than the nanocrystal, causing a small population of excited catalysts to have a proportionally larger signal. Although this catalyst does not have a strong emission feature, it is plausible that it is comparable to the extremely weak and partially quenched trap emission from the nanocrystals (QY_{Trap} <<1%). For this mechanism to be consistent with the data, catalyst emission also must be fast compared to the transfer process to avoid a delay between transfer and emission in the kinetics. The catalyst decay kinetics were measured by TA and TCSPC to have a suitably fast rate constant of 1.3×10^8 s^{-1} as shown in Figure 3.16.

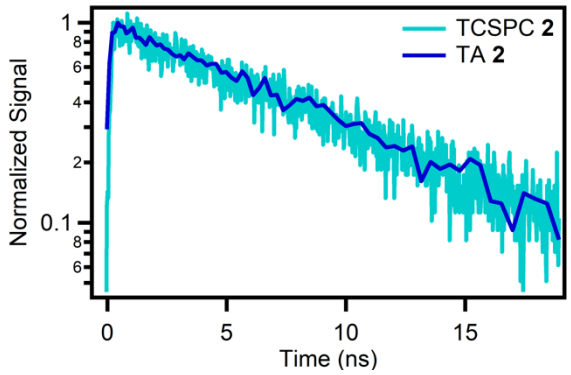

Figure 3.16: Decay kinetics of directly photoexcited catalyst 2, as measured by TA and TCSPC. TA kinetics were measured at the MLCT maximum (496 nm) following excitation at 400 nm. TCSPC was measured exciting with a 402 nm excitation source and observing emission at 720 nm with a 32 nm monochromator bandpass and a 420 nm long pass filter to remove scattered excitation light.

To look for a slow decay pathway of the trap emission induced by catalyst 2, TCSPC kinetics were taken with a larger time window as shown in Figure 3.17a. The trap emission has a weak and long-lived tail which decays nonexponentially over hundreds of nanoseconds. Upon

addition of catalyst, the trap emission decays more quickly in this time window, supporting the idea that addition of catalyst 2 does result in a new decay pathway with slow kinetics.

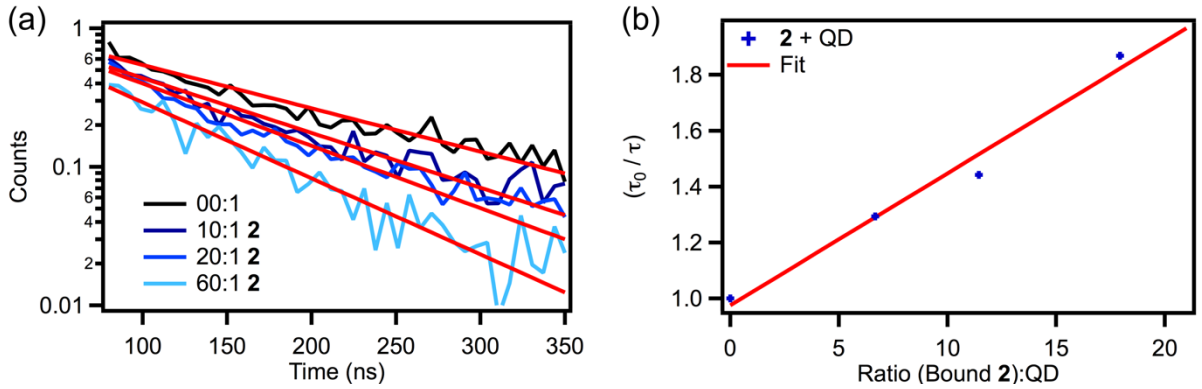

Figure 3.17 (a) Late time emission kinetics for different mixing ratios with catalyst 2 showing quenching on a nanosecond timescale. (b) Lifetime quenching as a function of number of bound catalyst 2 per nanocrystal for the data shown in (a), and a fit to the quenching model derived below.

To quantify the rate of energy transfer from the nanocrystal to the catalyst, we measured the decay of the QD in the presence of three different catalysts concentrations and fit the decay to time constant on an 80 – 350 ns time window. The quenching was fit to the Stern-Volmer expression for energy transfer

$$\frac{\tau_0}{\tau_q} = 1 + K_{SV}[\mathbf{2}] \tag{3.16}$$

but did not find a satisfactory fit. We suspected that the poor fit was due to bound catalysts performing the quenching rather than catalyst in solution. Taking a similar approach as used in Chapter 2,[41] we modify equation to predict the change in lifetime upon catalyst binding. The expression for the lifetime of a nanocrystal with <N> bound quenchers is

$$\tau_q = \frac{1}{k_0 + k_{NT} < N >} \tag{3.17}$$

where k_0 is the time constant of the decay and k_{NT} is the energy transfer rate constant. This can be linearized similarly to the Stern-Volmer expression

$$\frac{\tau_0}{\tau_q} = \frac{k_0 + k_{NT} < N >}{k_0} = 1 + \frac{k_{NT}}{k_0} < N > \tag{3.18}$$

<N> can be calculated using the ratio, QD concentration, equilibrium constant, and maximum number of catalysts bound as determined from the steady state quenching experiments. These numbers are given in Table 2. The values and the with the fit to the data is plotted in Figure 3.17b. The slope of the line produces a slope of 0.048, which corresponds to an energy transfer rate constant of 3.2×10^5.

Table 2 Catalyst Loadings and Lifetimes for Estimation of Energy Transfer Rate Constant

Mixing Ratio	<N>	τ (ns)	τ_0/τ_q
0	0	149	1
10	7.7	115	1.30
20	12.6	103	1.45
60	16.8	81	1.85

Although energy transfer is slow, it still represents a quenching pathway of the trap emission which may be detectable from our steady state quenching measurement. However, even at high ratios the quenching does not begin to affect the kinetics until 60 ns after excitation, by which point a majority of the total trap emission has already occurred. The signal to noise level of our quenching data and the small amount of catalyst emission present at the quenching wavelength may be concealing the weak trap quenching due to energy transfer.

Having noted these changes to the emission spectra and kinetics, we begin our examination of the TA of QDs mixed with catalyst 2. The picosecond TA spectra of QDs with and without catalyst 2 are shown in Figure 3.18a. The spectrum of catalyst 2/QD resembles the picosecond spectrum of catalyst 1/QD shown in Figure 3.8, containing nanocrystal signals with an additional bleach at the MLCT peak wavelengths due to hole transfer and photoexcitation. This feature is much weaker than observed in the catalyst 1/QD spectra due to the lower absorptivity of catalyst 2 at both the pump and probe wavelengths. The entire TA spectrum of the catalyst 2/QD solution decays to baseline on the timescale of the QD bleach decay.

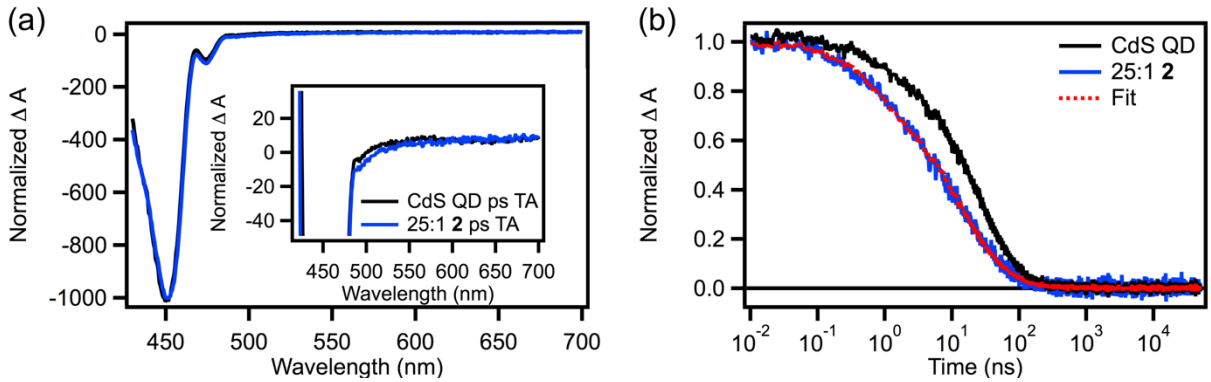

Figure 3.18 (a) TA spectra of CdS QD and 25:1 catalyst 2/QD solution averaged from 10 to 20 ps. Inset: Zoom-in view of (a), showing the changes in the region of the catalyst 2 MLCT absorption. (b) Kinetics of TA samples from (a) taken at 456 nm. The 25:1 sample was fit using the kinetics of the QDs combined with a biexponential fit.

The transient absorption kinetics of catalyst 2/QD mixtures shown in Figure 3.18b demonstrate changes on a faster timescale than seen in TCSPC. The presence of lifetime shortening in TA and the lack of shortening in emission kinetics on this timescale allow us to assign these changes to the population of nanocrystals which performed hole transfer to catalyst 2. To find the lifetime of the recombination we needed to extract these two populations from TA, an issue which was not present in catalyst 1/QD samples due to the separation in timescales between electron transfer and transferred-hole recombination.

To quantify the decay due to recombination we treated the TA decay as a sum of two populations with different decay kinetics

$$\Delta A(t) = \Phi_{HT1} \times A_{HT}(t) + (1 - \Phi_{HT1}) \times A_{Tr}(t) \qquad (3.19)$$

where ΔA is the QD bleach kinetic signal, Φ_{HT1} is the hole transfer efficiency as defined in (3.3), A_{HT} the kinetics of the hole-transfer population, and A_{Tr} the kinetics of the trapped hole population. As there were only minor changes in the TCSPC kinetics, we assume that A_{Tr} has kinetics identical to the QD sample. We found that the kinetics of A_{HT} were best approximated by a biexponential decay. The function used to fit the data was

$$\Delta A(t) = \Phi_{HT1} \times (A_1 e^{-t/\tau_1} + A_2 e^{-t/\tau_2}) + (1 - \Phi_{HT1}) \times A_{QD}(t) \qquad (3.20)$$

where $A_{QD}(t)$ represents the kinetics of the QDs without catalyst 2. The result of this fit is shown in Figure 3.18b, and the fit parameters are given in Table 3, along with as the time averaged rate constant

$$\bar{k} = \frac{1}{\sum_i a_i \tau_i} \tag{3.21}$$

where a_i and τ_i are the multiexponential fit parameters of the hole-transfer population.

Table 3 Fit to TA Decay of 25:1 Catalyst 2

Φ_{HT1}	A_1	τ_1 (ns)	A_2	τ_2 (ns)	$\bar{k}$ (s^{-1})
0.48	0.40	0.80	0.60	9.1	1.7×10^8

As expected from the quenching data, the efficiency for hole trapping and direct hole transfer are approximately equal at this mixing ratio. This was also seen in catalyst 1, where approximately half of the TA decay occurred through the electron transfer pathway. The decay of the trapped hole state is biexponential, which was not observed in catalyst 1. However, the average rate constant for the biexponential transferred hole recombination is 1.7×10^8 s^{-1}, similar to the value obtained for catalyst 1 recombination.

The complete kinetic model for QDs and catalyst 2 is shown in Figure 3.19. The principal difference between the two models is the removal of the electron transfer from the catalyst 1 model and the observation of an energy transfer pathway. The slower rate of energy transfer compared to electron transfer means that it is a minor pathway for the trapped hole population, which accounts for the lack of trap emission quenching by catalyst 2. The behavior of the transferred hole pathway is nearly identical for both catalysts despite their differences in energetics, although in catalyst 2 the decay of this state follows a biexponential process.

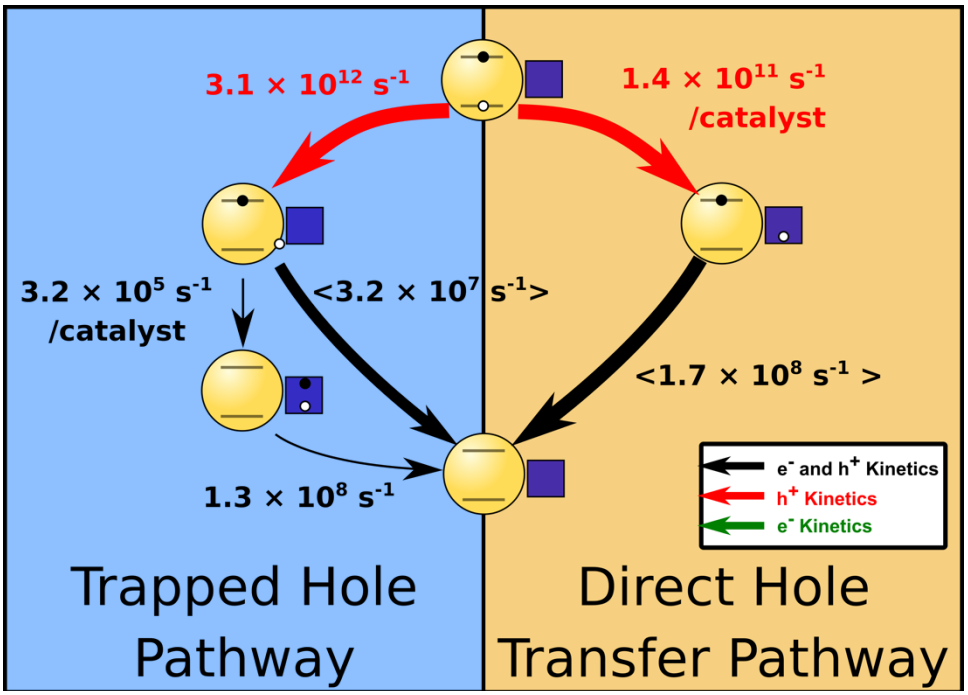

Figure 3.19 Kinetic scheme for the decay of catalyst 2/QD mixture. The arrows (in descending order by rate constant) indicate hole trapping, valence band hole transfer to catalyst 2, recombination of the transferred hole, recombination across the MLCT state of catalyst 2, trapped hole recombination, and energy transfer to catalyst 2. The width of the arrows indicate the efficiency of each process for high-loading conditions. Angled brackets indicate an average rate constant.

3.3.7. Comparison of Systems and Final Remarks

Having now determined the complete kinetic schemes for decay of both catalyst/QD systems in Figure 3.12 and Figure 3.19, we now address the differences between the kinetic models for each catalyst and the implications of the measured rate constants for water oxidation catalysis using these systems. In Chapter 2,[41] catalyst 1 was shown to be a potentially promising water-oxidation co-catalyst for QDs based upon the complex's rapid hole transfer rate and strong binding. Catalyst 2 has similarly fast and promising hole transfer characteristics. The lack of change in hole transfer kinetics for catalyst 2 despite the significant increase in driving force suggests that optimization of the catalyst energetics may not lead to gains in hole transfer efficiency. On the

other hand, the increase in quenching with this QD sample confirms our earlier prediction that the efficiency of hole transfer can be easily improved by reduction of the hole trapping rate.[41]

Catalytic efficiency depends on the hole transfer quantum efficiency as well as the lifetime of the charge separated state, both of which were determined in our models for the transferred hole population for each catalyst. Although the hole transfer efficiency with these catalysts only reaches 50% with surface saturation, the 3-4 orders of magnitude in time for which the transferred hole state exists before recombination is promising for catalytic applications. This long-lived charge separated state indicates that this system can potentially be coupled to a variety of electron scavengers and reductive co-catalysts, insofar as they are able to compete with the 1.8×10^8 s^{-1} recombination rate. The electron could be efficiently removed through either methyl viologen reduction ($\sim 10^{10}$ s^{-1}) or electron transfer to a platinum co-catalyst ($\sim 10^{12}$ s^{-1}), as both are substantially faster than the recombination rate for the direct hole transfer pathway.[110] On the other hand, the hydrogenase enzyme has an electron transfer rate of 2.4×10^7 s^{-1} from photoexcited CdS nanorods and would not be an efficient partner in preventing recombination.[47]

Although we obtained a rate of energy transfer for catalyst 2/QD complexes, the mechanism which facilitates energy transfer to the catalyst is not obvious. The catalyst has a weak absorption shoulder which covers much of the visible region, meaning Förster energy transfer is a possible pathway for catalyst excitation. On the other hand, trap states have been shown to enable non-Förster energy transfer from QDs to phthalocyanine complexes. If the energy transfer occurs through charge transfer of both electron and trapped hole, scavenging of the electron may enable a pathway to transfer the trapped hole to the catalyst. Future improvements in efficiency of hole transfer could be achieved through transferring both valence band and trapped holes to the catalyst over longer timescales.

For catalyst 1 we did not observe the same characteristic signatures of energy transfer which were seen in catalyst 2. This was likely due to the electron transfer pathway rapidly depleting the trapped hole population and quenching both trap and energy transfer emission. The weak emission feature of catalyst 1 also made observation of energy transfer a challenging task. At very high ratios, the steady state PL spectrum quenched by catalyst 1 does appear to have a slight redshift, which may be a signature of energy transfer to the weak catalyst 1 emission. Our ability to investigate this feature is limited due to the sensitivity of our detector as we approach 800 nm, but future work may reveal that the remaining trapped hole population in catalyst 1/QD systems undergoes energy transfer similarly to the catalyst 2 system.

3.4. Conclusions

Combining a number of spectroscopic techniques, kinetic models were generated for a series of two WOC's mixed with CdS QD sensitizers. Both systems exhibited excited state bifurcation in on a picosecond timescale, leading to a population of nanocrystals with trapped holes and a population of nanocrystals with holes transferred to the catalyst partner. The trapped hole population was shown to undergo electron or energy transfer to the catalyst depending on the relative positions of the catalyst LUMO and the QD conduction band. Following electron transfer, the reduced catalyst decayed over the course of microseconds through a mechanism involving diffusion-limited trapped-hole recombination.

The population which decays through the direct hole-transfer pathway was established through sub-picosecond photooxidation of the catalyst, with similar rates of valence band hole transfer observed for each catalyst. The charge separated state remained intact for 3-4 orders of magnitude in time before recombination. This fast hole transfer and long lifetime of this charge

separated state highlights the potential value of these catalysts as oxidative partners in a solar water-splitting tandem with a highly active reductive co-catalysts.

Chapter 4 Binding Orientation of a Ruthenium Based Water Oxidation Catalyst on a CdS QD Surface Revealed through NMR Spectroscopy

4.1. Introduction

CdS nanostructures represent a promising platform for photocatalysis due to their strong absorptivity for visible light and tunable surface chemistry which enables coupling to a variety of substrates and co-catalysts.[5, 7, 26, 46] Strong interactions between light-absorber and charge-acceptor are essential to maximize the number of active catalysts and to promote the donor-acceptor coupling required for rapid charge transfer.[47] The advantages of strong surface interaction for photoreductive catalysis are apparent in the rapid rates of photoinduced electron transfer from cadmium chalcogenide nanostructures to surface-bound Pt[110] and Ni[117] H_2 reduction co-catalysts. In these systems reductive efficiency is limited not by electron transfer but by sluggish hole removal dynamics,[45, 118] enabling noncatalytic processes such as hole trapping and electron-hole recombination. Hole scavenging in CdS QDs typically occurs on a nanosecond timescale, much slower than typical rates of electron transfer, a difference which has been attributed to reduced surface overlap due to the higher effective mass of the hole.[119-120] More recently, sub-picosecond hole transfer rates were achieved by Weiss et al.[72] using dithiocarbamate functional groups to attach hole scavengers to the nanocrystal surface, an advancement which facilitated the development of the first water splitting nanocrystal system.[33] The key improvement which allowed for faster hole transfer in these systems was the interaction between the electronic structure of the dithiocarbamate and quantum dot (QD),[121] which provides an efficient coupling pathway between the valence band of nanocrystals and electronic structure of acceptors.

We have previously observed picosecond hole transfer in a molecular-nanostructure system consisting of a Ru-based water oxidation catalyst (WOC) mixed in solution with CdS QDs.[41] The rapid rate of charge transfer indicated that the WOC was binding to the QD surface, and modelling of the quenching data gave evidence for a strong binding interaction with the QD surface. The large rate constant for hole transfer suggested substantial electronic coupling between the QD and WOC, but neither the interaction by which the complex binds to the QD nor the source of the electronic coupling could be determined with PL quenching methods. Systems designed with a well-defined covalent linkage to the QD surface benefit from an obvious orientation between the QD and charge acceptor, allowing identification of likely coupling pathways through examination of the molecular frontier orbitals.[121] Our WOC/QD system lacked this orientational specificity, as binding was believed to occur through coulombic interactions between the anionic QD ligands and the cationic WOC. An improved understanding of the QD/WOC interaction is needed to determine the factors which contribute to the observed fast hole transfer.

In this report we use NMR spectroscopy to study the WOC/QD binding in our system. Measurements of both the chemical shift and lifetime of the WOC polypyridyl proton NMR signals suggest binding with preferential orientation, bringing the terpyridine and chloro ligands of the WOC into proximity with the nanocrystal surface. We discuss the possible factors which lead to the binding and alignment of the WOC on the QD, as well as the role the WOC orientation may play in coupling the QD valence band and frontier molecular orbitals. We discuss the significant implications of the oriented attachment to charge transfer catalysis in this system as well as how it informs the design of future WOC/QD photocatalysts.

4.2. Materials and Methods

4.2.1. CdS QD Synthesis and Ligand exchange

CdS QDs were synthesized according to the method described in Chapter 2, with the synthesis scaled up by a factor of 2.[41] The resulting QDs had a band gap of 462 nm (Figure 4.1). This corresponds to a QD with a diameter of 5.8 nm and a molar absorptivity of 1.2×10^6 M^{-1} cm^{-1} based on the sizing curves from Yu et al.[63]

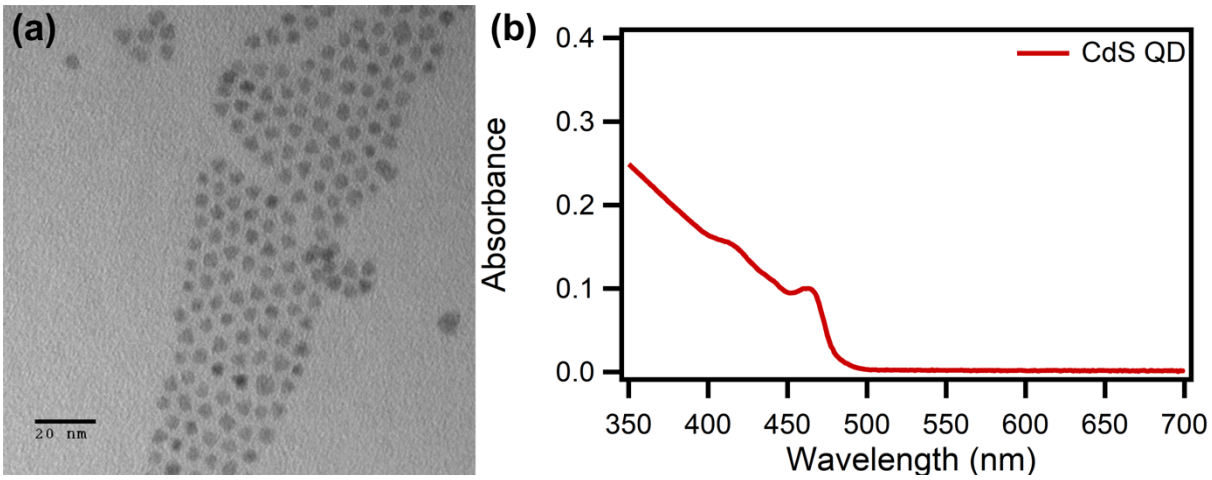

Figure 4.1 (a) TEM micrograph of CdS QDs. (b) UV-Visible absorption spectra of CdS QDs.

The ligand exchange protocol (Chapter 2) was modified to prepare samples for NMR analysis as follows.[71] The typical volume of oleate-capped QDs used for preparation of ligand exchanges was increased 5 to 10-fold, (500 µL – 1 mL) and the volume of ligand exchange solution was doubled (2 mL). Following precipitation with toluene and resuspension in methanol, the particles were crashed out of solution again using a second addition of toluene in minimal volume to precipitate the QDs. The supernatant was decanted, and a few drops of methanol were added to encourage formation of an azeotrope with the residual toluene, and the solution was dried in a vacuum chamber overnight. This procedure typically resulted in the removal of most toluene, but a residual solvent peak was still noticeable in some cases. The dried pellet was redispersed in a

minimal volume of deuterated methanol and its concentration determined using UV-Visible spectroscopy.

4.2.2. Ruthenium Complex Synthesis

The WOC was synthesized as described in Chapter 2. All samples used for NMR studies were dissolved in deuterated solvents in an Ar filled glovebox shortly prior to use.

4.2.3. NMR Spectroscopy

For all NMR experiments 500 – 700 μL solutions were made under Ar. Samples containing QDs were sealed using a screw-cap in airtight tubes. Typical concentrations for these experiments were 35 μM for QDs and/or 350 μM WOC in MeOD. Experiments involving WOC without QDs were performed in deuterated acetone to minimize transesterification. For routine NMR spectroscopy, ^{1}H NMR spectra were acquired on a Bruker advance-III spectrometer operating at a ^{1}H frequency of 300 MHz equipped with smart broadband probe at room temperature (299 K). For typical 1D ^{1}H measurements, 64k data points were acquired with a spectral width of 21.6 ppm, 3s acquisition time and a 1 s relaxation delay with pulse width 12.5 μs.

For two-dimensional NMR experiments including COSY, HSQC, HMBC, TOCSY, and relaxation (T_1 and T_2 lifetime) measurements, Agilent INOVA 500 spectrometer operating at 499.599 MHz with VNMRJ 3.2 software and equipped with a 5 mm triple resonance HCN probe at 295 K was used. For ^{1}H NMR data acquisition; acquisition time 3.0 s, spectral width 8 kHz, pulse width 6.12 μs, relaxation delay 2.0 s and 16 scans were used. TOCSY spectra were collected using 256 t1 increments and spectral widths of 5000 Hz in both dimensions with acquisition time 0.15 s, relaxation delays 2.0 s and a spinlock (MLEV-17) mixing time of 80 ms. Spin lattice relaxation time (T1) was measured using an inversion recovery sequence with relaxation delay

40.0 s and 16 scans. Spin-spin relaxation (T_2 lifetime) measurements were conducted using the CPMG (Carl-Purcell-Meiboom-Gill) pulse sequence. Data were processed using Mnova software.

4.3. Results and Discussion

As discussed in Chapters 2 and 3, CdS QDs with a 3-mercaptopropionate (3-MPA) surface exhibit ultrafast hole transfer behavior when mixed with the WOC [Ru(dmcbpy)(tpy)Cl]PF_6 (dmcbpy = 4,4′-dimethylcarboxylate-2,2′-bipyridine, tpy = 2,2′:6′2″-terpyridine).[41] The extremely rapid rate of hole transfer and the characteristic quenching behavior under different WOC loadings is strong evidence that the WOC must be directly interacting with the nanocrystal surface, as the rate constant observed for charge transfer is an order of magnitude greater than the upper bound obtainable in diffusion limited collisional charge transfer.[122] Although fluorescence quenching indicates that the WOC is binding to the surface, this technique does not describe the nature of the binding interaction leading to charge transfer.

Common 1D ^{1}H NMR measurements on nanocrystals are insensitive to the inorganic structure of the QD but exhibit dramatic changes to the spectrum of molecules which associate with the QD surface. The most diagnostic of these changes upon binding is that protons on bound molecules have greatly increased linewidths compared to those free in solution, even leading to complete disappearance of the resonance.[123] The chemical environment near the QD can also lead to shifting of the peaks in the NMR spectrum, providing further evidence of binding.[123-125]

These effects of molecular interaction with QDs are apparent in the ^{1}H NMR spectrum of CdS QD with 3-MPA surface ligands dissolved in MeOD shown in Figure 4.2. At 2.72 ppm and 2.47 ppm we see two sharp triplets due to free 3-MPA ligands, as well as a broad resonance centered near 3 ppm which has been assigned to 3-MPA bound to the nanocrystal surface. There

is also a strong peak at 3.24 ppm from the tetramethylammonium (TMA) counterions which charge balance the surface bound 3-MPA. This peak is also broadened and shifted from its normal position at 3.19 ppm, despite the tertiary amine not having the ability to directly bond to the surface.

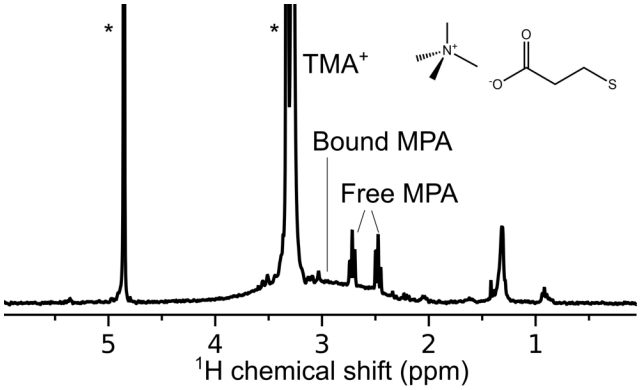

Figure 4.2 ^{1}H NMR spectrum of CdS QD with a 3-MPA surface in MeOD. This spectrum exhibits peaks characteristic of bound and free 3-MPA, as well as solvent peaks, TMA counterion peaks, and an aliphatic impurity from synthesis. This spectrum was acquired on a 300 MHz NMR spectrometer.

4.3.1. Assignment of WOC NMR Peaks

The WOC exhibits an NMR spectrum dominated by the protons in the polypyridine system as shown in Figure 4.2b. To understand the effects of binding to QDs, we first must assign the resonances in the WOC spectrum to specific protons. First, we examine the integrals of the individual peaks. As has been observed in similar WOCs, several dmcbpy protons display a pronounced shift downfield due to the inductive effects of the halogen near proton 1.[126] This disrupts the symmetry of the dmcbpy ligand, leading all protons in that system to have integrals of 1. In contrast, all of the terpyridine protons integrated to 2, with the exception of proton a. This proton was easily identified by its triplet splitting. Knowing which ligand each resonance belongs to, we now must relate the chemical shift to position within the ligand.

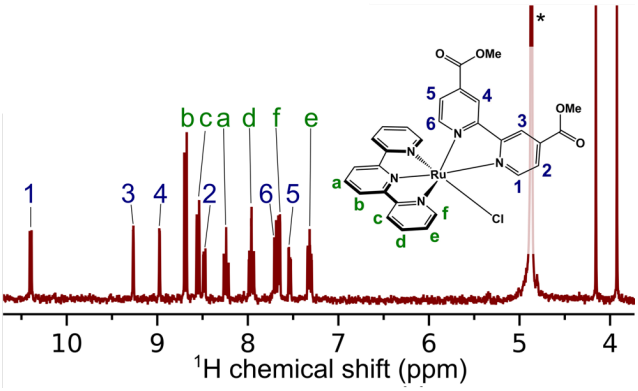

Figure 4.3 ^{1}H NMR spectrum of the WOC. These data were acquired on a 300 MHz NMR spectrometer.

As protons couple strongly within individual aromatic rings, 4 correlated aromatic spin systems are expected for this molecule corresponding to the two rings of dmcbpy, the central terpyridine ring, and the terminal terpyridine rings. The COSY spectrum shown in

Figure 4.4 confirms this, with the correlated spin systems being distinguished by color. As we have assigned the farthest downfield proton to proton 1, protons 2 and 3 were trivial to assign based on the COSY, with proton 2 exhibiting a larger J value than proton 3. The other dmcbpy ring was assigned similarly, based on the integrals, COSY, and J values. The terpyridine resonances on the central ring (protons a, b) were trivial to assign from the COSY and their splitting pattern. Assignment of the protons on the terminal rings of the terpyridine were more challenging as the pairs c, f and d, e have similar correlations and splitting patterns.

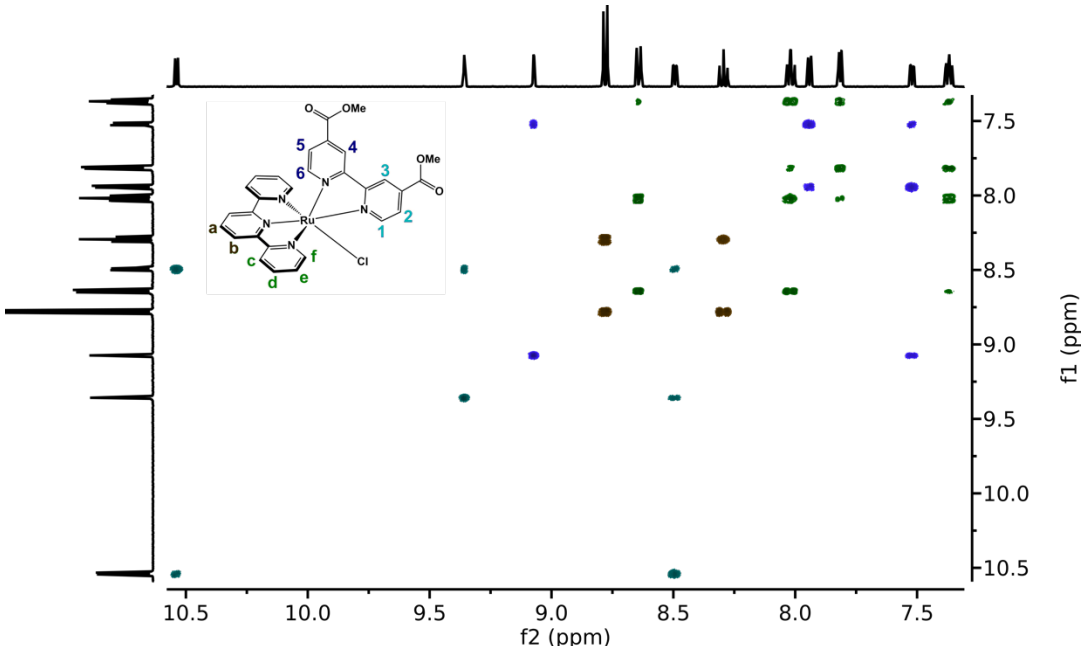

Figure 4.4 COSY of the WOC in acetone-d6.

The assignment of the remaining protons was performed using HSQC and HMBC. The HSQC spectrum shown in Figure 4.5 correlates directly interacting ^{13}C and ^{1}H nuclei, allowing us to assign peaks in the ^{13}C NMR. The HMBC spectrum shown in Figure 4.6 correlates ^{13}C and ^{1}H across two or three bonds, with suppression of single bond correlations. Examining the terminal terpyridine ring protons in the HMBC, we see correlations between 3 terpyridine protons and a carbon at 158 ppm. This carbon did not correlate to any protons in the HSQC spectrum, which means that it is likely the signal of carbons 2 (C_2) and 2″ in the terminal terpyridine rings. Proton e is para to C_2 and does not couple to C_2 in HMBC, allowing us to assign proton e to the doublet of doublet of doublets at 7.4 ppm. We also assign proton d to the other doublet of doublet of doublets at 8.02 ppm. Finally, we assign protons c and f based on the COSY, as proton e has a stronger correlation with the doublet of doublets at 7.81 ppm than to the similar signal at 8.64 ppm. These assignments follow the same ordering of protons with respect to ^{1}H chemical shift observed in similar terpyridine complexes, as expected by the weakly perturbative interactions between the terpyridine and other ligands.[93]

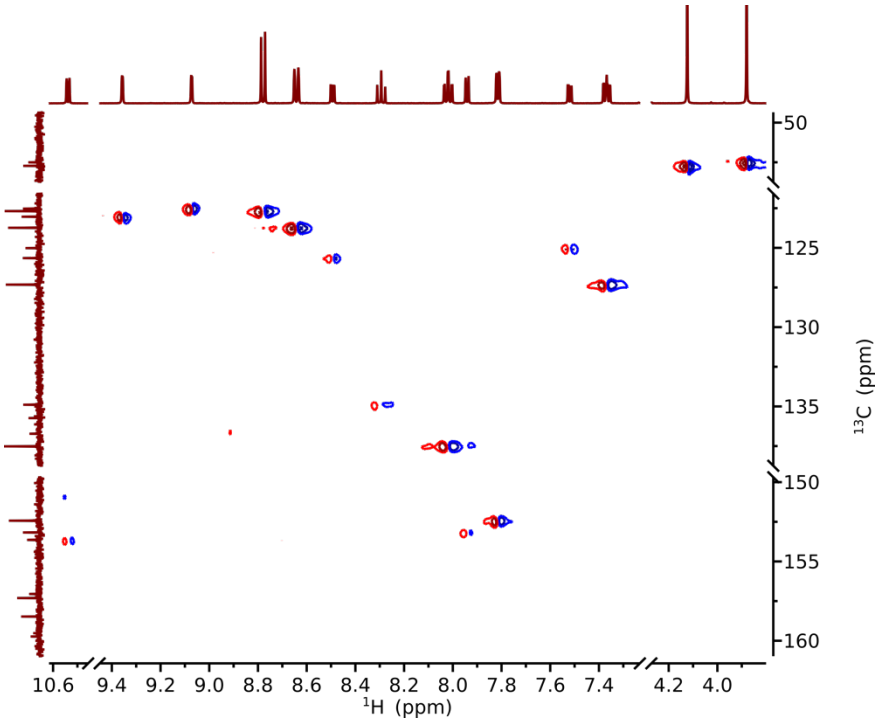

Figure 4.5 HSQC spectra of the WOC in acetone-d6.

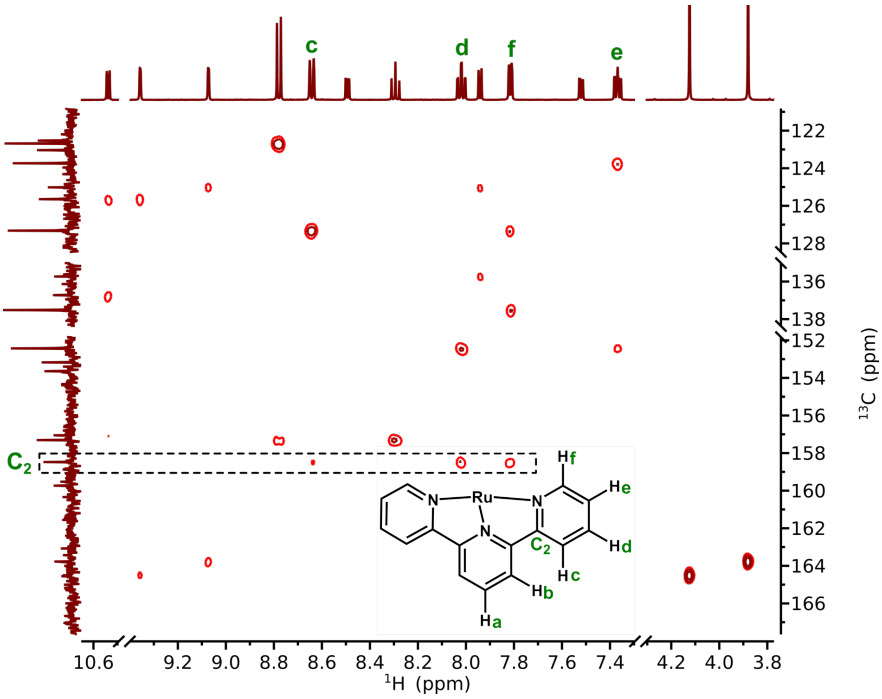

Figure 4.6 HMBC Spectrum of the WOC in acetone-d6. The highlighted peaks are correlations between protons c, d, and f with carbons 2 and 2" in terpyridine.

Upon mixing the WOC and nanocrystal at a 10:1 ratio, we immediately notice several changes to the 1D NMR as shown in Figure 4.7. The peaks associated with the WOC are broadened and shifted by the presence of the QD, as expected for surface bound species. No residual sharp peaks are observed from free WOC, indicating either that the catalyst is entirely bound or that binding and debinding occurs rapidly on the NMR time scale. Based on the Langmuir equilibrium constants measured in the prior chapters (~10^6 M^{-1}), at this QD concentration >99% of catalysts should be bound to the QD surface.[41] The WOC peaks are not as broadened as those of bound 3-MPA shown in Figure 4.2. This may indicate that the catalyst is less hindered in its motion than bound 3-MPA, or that it experiences less inhomogeneous broadening.

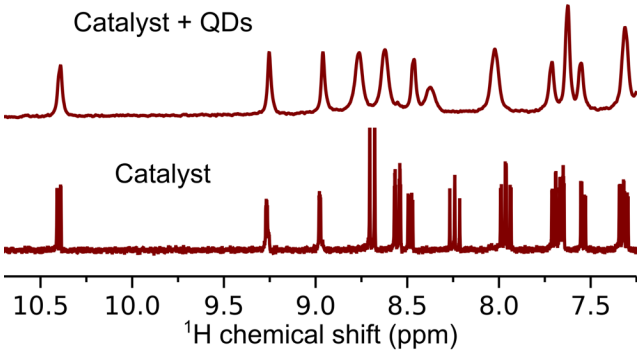

Figure 4.7 NMR spectra of the aromatic region of the WOC with and without QD added.

Although all WOC peaks in the aromatic region broadened upon addition of the QD, peaks appeared to demonstrate non-uniform changes in chemical shift. This seems to suggest that the protons are experiencing a range of chemical environments near the QD, ranging from solvent-like to QD specific. Determination of trends in perturbation strength as a function of proton position within the WOC could contain information about its binding mode to the QD surface. However, it was first necessary to re-assign the NMR peaks to protons in the WOC/QD mixture. This was accomplished using TOCSY on the mixed system, which measures the correlations between protons seen in Figure 4.8. TOCSY was selected rather than COSY to obtain these

correlations as the broad peaks seen in Figure 4.7 suggested fast spin relaxation, an issue which diminishes the correlations seen in COSY but has a lesser effect on TOCSY. The correlations between protons observed through this technique show the same four spin systems seen in Figure 4.4. This allowed us to assign the protons of the 1D spectrum, as indicated in Figure 4.9.

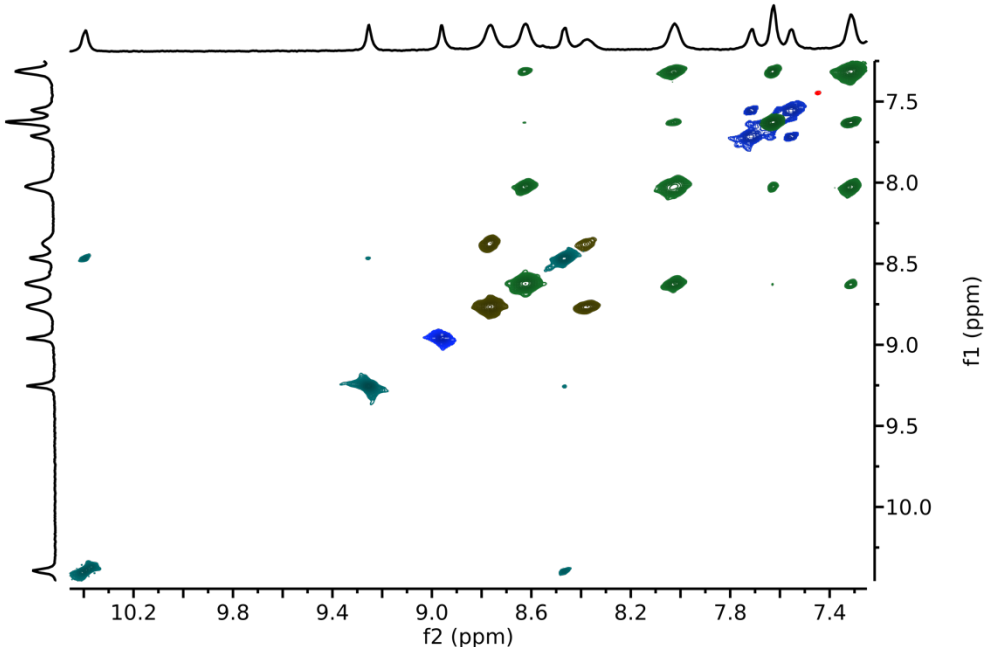

Figure 4.8 TOCSY of 10:1 WOC/QDs in MeOD. Diagonal and cross-peaks were color coded based upon their correlations, with peaks belonging to the terpyridine highlighted in green and brown and peaks from the bipyridine in blue and teal. Based upon the similar COSY of the WOC shown in Figure 4.4, we have assigned each NMR peak of the mixed QD/WOC system to a proton.

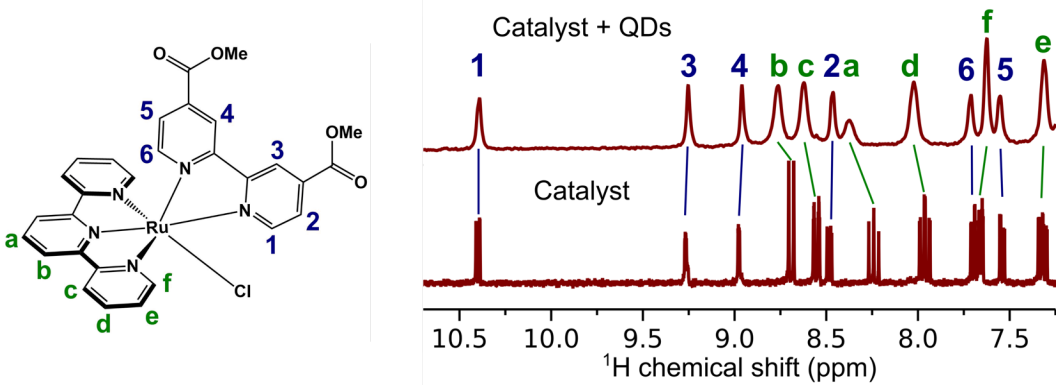

Figure 4.9 Assignments of proton resonances in the ^{1}H NMR spectrum of WOC + QDs based on analysis of the TOCSY spectrum shown in Figure 4.8. Lines between the spectra indicate the change in chemical shift upon addition of the QDs.

4.3.2. Effects of Binding on WOC Chemical Shift and Relaxation Time

The changes in chemical shift (ΔCS) for each proton are enumerated in Table 4. Several patterns emerge in ΔCS based on the proton positions on each ligand. Upon mixing with the QD, ΔCS steadily decreases proceeding from terpyridine proton a to f. The dmcbpy protons exhibited much smaller changes upon addition of QD. As proton 1 on dmcbpy tends to shift upon displacement of the chloride ligand,[126] the changes to the NMR spectrum do not seem to be due to chloride loss.

Table 4 Peak positions and T_2 lifetimes for WOC protons

Proton	**1** (ppm)	QD+**1** (ppm)	ΔCS (ppm)	T_2 (ms)
1	10.3982	10.3944	-0.0038	62.0
3	9.2635	9.2531	-0.0104	44.7
4	8.9777	8.9604	-0.0173	45.4
b	8.6887	8.7641	0.0754	24.2
c	8.5508	8.6232	0.0724	26.7
2	8.4807	8.466	-0.0147	76.1
a	8.2394	8.3735	0.1341	24.8
d	7.9555	8.9228	0.0673	35.9
6	7.6984	7.7155	0.0171	59.2
f	7.6544	7.6264	-0.028	65.7
5	7.5383	7.5531	0.0148	55.7
e	7.3238	7.314	-0.0098	46.7

Closer examination of the catalyst peaks in the presence of QDs reveals that the shifted protons also experienced substantial increases in peak linewidth. QDs often cause broadening of NMR features by decreasing in the spin-spin relaxation time (T_2) of the NMR signal.[123] T_2

relaxation is an important concept in NMR and merits a brief description before we proceed. The signal in NMR spectroscopy is measured from the precession of the sample's magnetization vector in an applied magnetic field.[127] The magnetization vector is a sum of the individual magnetic moments due to the nuclear spins, which begin with a fixed phase relationship following coherent excitation by a RF pulse. As time evolves this phase relationship decays through a variety of mechanisms, some acting uniformly on all spins (homogeneous) and some acting nonuniformly (inhomogeneous). The timescales of homogeneous and total relaxation are distinguished as T_2 and T_2*. Transient interactions with the solvent can lead to homogenous broadening, but the fast rotations and vibrations of molecules serve to average out these interactions.[128] Due to their large volumes, QDs possess long rotational correlation times, on the order of 10^{-7} s.[129] Any surface bound species also rotate slowly, leading to an decrease in the T_2 relaxation timescale. For ^{1}H NMR this is manifested as lifetime broadening, given by the relationship[127]

$$\Delta\nu \, T_2^* \geq 1 \tag{4.1}$$

where $\Delta\nu$ is the broadening of the signal in Hz.

To better understand what leads to the observed broadening, we directly measured the (homogeneous) T_2 lifetime using a spin-echo technique.[130] We briefly describe the principles of this measurement here, and refer the reader to more comprehensive treatments elsewhere.[123, 130] The individual steps as viewed from the rotating frame are depicted in Figure 4.10, starting with a net sample magnetization along the z-axis induced by the static magnetic field of the spectrometer (B_0). As in 1D ^{1}H NMR, a RF pulse is used to tip the sample magnetization into the x-y plane of the Bloch sphere (Figure 4.10b). Inhomogeneous effects lead to each proton experiencing a slightly different magnetic field, B_{eff}, causing a distribution in precession rate and leading to dephasing of the magnetization in the x-y plane (Figure 4.10c). Concurrently, homogeneous T_2 decay is

occurring which leads to randomized loss of phase coherence. After a specified delay time T_{delay}, a second RF pulse is introduced, which inverts the position of each spin on the x-y plane of the Bloch sphere (Figure 4.10d). This inversion places the more slowly precessing magnetization vectors ahead of the central frequency in the rotating frame x-y plane and places the more quickly precessing magnetization vectors behind the central frequency. A second delay is afforded of duration T_{delay} which allows the overall magnetization to recohere, after attenuation by homogeneous effects (Figure 4.10e). Following recoherence, a free induction decay (FID) is recorded (Figure 4.10f). The strength of the magnetization is measured through a Fourier transform of the FID and integration of the peak at the desired frequency. T_2 is extracted by measuring this integral as a function of T_{delay}, which is then fit to an exponential.

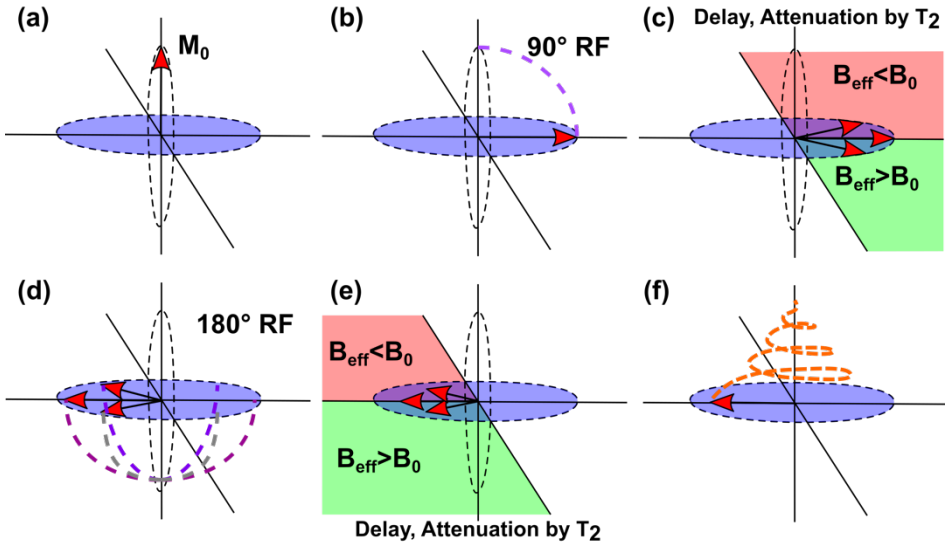

Figure 4.10 Procedure for measurement of T_2 using spin echo, as viewed from the rotating frame, based on similar illustrations from Carr et al.[130] (a) Prior to excitation, the ensemble of spins produces a net magnetization, M_0, aligned with the external magnetic field. (b) An RF pulse tips the net magnetization into the x-y plane. (c) Due to inhomogeneities in the magnetic field, some protons precess faster or slower than the central frequency. Simultaneously, homogeneous T_2 shortening leads to irreversible loss of phase information and attenuation of all magnetization components. These two effects are allowed to occur for a fixed delay. (d) An RF pulse is used to tip the overall magnetization by 180°. (e) A delay of equal duration to the one used in (c) is allowed. During this time, the protons with difference B_{eff} experience an equal and opposite phase shift to the phase shift accrued during the previous delay, leading to recoherence. As occurred during (c), homogeneous T_2 relaxation irreversibly removes magnetization. (f) After

recoherence the FID is acquired, and the resonance integrated to measure the homogeneously lost magnetization as a function of delay time.

The T_2 lifetimes of the WOC peaks range from 76.1 ms to 24.2 ms as given in Table 4 and illustrated in Figure 4.11a. Similar to the trends seen in ΔCS, the T_2 lifetime shows a pronounced contrast between terpyridine and bipyridine protons, with terpyridine protons tending to be shorter-lived. To visualize the similarity between these trends, we plotted the relaxation rate (T_2^{-1}) and magnitude of ΔCS for each proton as shown in Figure 4.11b. There is a fairly strong correlation between the two, suggesting that interaction with the QD is consistently affecting both chemical shift and T_2 time as a function of proton.

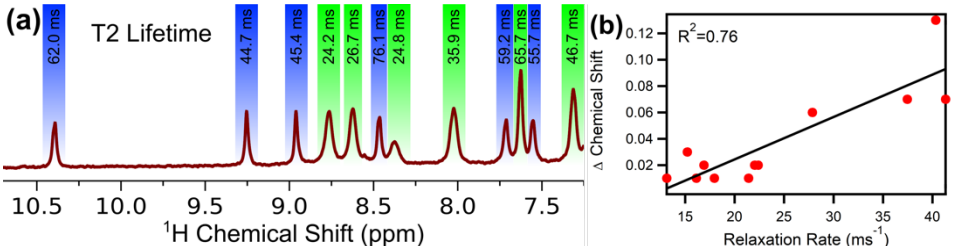

Figure 4.11 (a) T_2 relaxation lifetime of each peak in the proton NMR of a WOC/QD solution. The terpyridine resonances (green highlight) tend to have shorter T_2 lifetimes than the dmcbpy resonances (blue highlight). (b) The correlation in absolute change in chemical shift with relaxation rate (T_2^{-1}).

Broadening of the peaks of surface bound species contains both homogeneous and inhomogeneous contributions. The inhomogeneous broadening has been attributed to solvation effects, where tightly packed surface ligands lead to inhomogeneous solvent environments.[131] The total relaxation time T_2^* containing homogeneous and inhomogeneous components can be determined from the linewidths ($\Delta\nu = \frac{1}{\pi T_2^*}$).[127] In Table 5 we compare T_2 and T_2^* for the four furthest downfield peaks, with linewidths measured through fitting the peaks to Lorentzian doublets with the same J values as in the WOC only sample. The values seen here show relatively little inhomogeneous broadening (T_2^*~1.5 T_2) compared to the inhomogeneous broadening experienced by bound surface ligands (T_2^*~8 T_2).[131] The limited inhomogeneity could indicate the

WOC are well solvated, and do not cluster together on the surface. This supports our estimations of surface coverage from Chapter 2, which concluded that even at high ratios the surface is only sparsely covered in WOCs.

Table 5 Comparison between calculated and measured linewidths for selected protons in QD/WOC mixture.

Proton	1	3	4	b
Calculated Peak Width (Hz)	5.1	7.1	7.0	13.2
Fit Peak Width (Hz)	9.9	10.8	10	18.4

These nanocrystals are known to engage in photoinduced charge transfer to this WOC, as well as 3-MPA and a number of other species.[41, 46] Paramagnetic species such as photogenerated radicals are also known to cause broadening of NMR resonances by stimulating emission from the excited spin state.[127] This returns the magnetization to the z-axis in the Bloch sphere, decreasing signal from the x-y plane in a mechanism known as T_1 relaxation. T_1 relaxation also leads to an observed reduction in the T_2 lifetime, as return of the magnetization to alignment along the z-axis decreases its projection into the x-y plane as well.[128] To test if the changes in T_2 lifetime were due to enhanced T_1 decay, the T_1 lifetimes of the WOC protons were directly measured using inversion recovery. The obtained values of T_1 ranged from 1 to 3 s, comparable to those observed in free WOCs. This shows that any radicals photogenerated by ambient light either decay prior to the beginning of the NMR experiment or do not interact strongly with the bound WOCs.

4.3.3. Determination of WOC Orientation and Implications for Catalysis

It has been observed before with bound ligands on the surface of QDs that T_2 lifetimes tend to shorten for protons nearer to the QD surface.[123] This is due to the greater range of motion further from the surface allowing molecules to undergo hindered rotations which partially average over the transient interactions which accelerate T_2 decay. Based on this interpretation, both our T_2 and

chemical shift measurements suggest that the central terpyridine ring is closest to the QD. This observation comes with the caveats that NMR reflects the behavior of an ensemble of WOCs averaged over the millisecond timescale of the NMR measurement and could further reflect a dynamically-averaged behavior rather than a static one, such an equilibrium between oriented and disoriented catalysts. Keeping the nature of the experiment in mind, the data appears to indicate a preferential orientation of the WOC with respect to the QD which brings the terpyridine into proximity with the particle surface.

Based upon the peak shifting and T_2 data, we are able to further refine our model of the orientation between WOC and QD. We assert that an optimal orientation between the WOC and nanocrystal surface will provide uniform trends in both measured parameters as a function of distance from the QD surface. We begin by placing proton a closest to the surface. The distances between WOC protons and the QD depend on the angle between the surface and terpyridine plane shown in Figure 4.12a. Changing this angle leads to more motion of the dmcbpy protons than the terpyridine protons. As do not see a strong difference between the two dmcbpy rings in either the T_2 or chemical shift data, we expect that the two dmcbpy rings are approximately equidistant from the surface. This leads us to the orientation shown in Figure 4.12b, which satisfies our requirement for uniform trends in both ΔCS and T_2 lifetime as a function of distance from the QD surface.

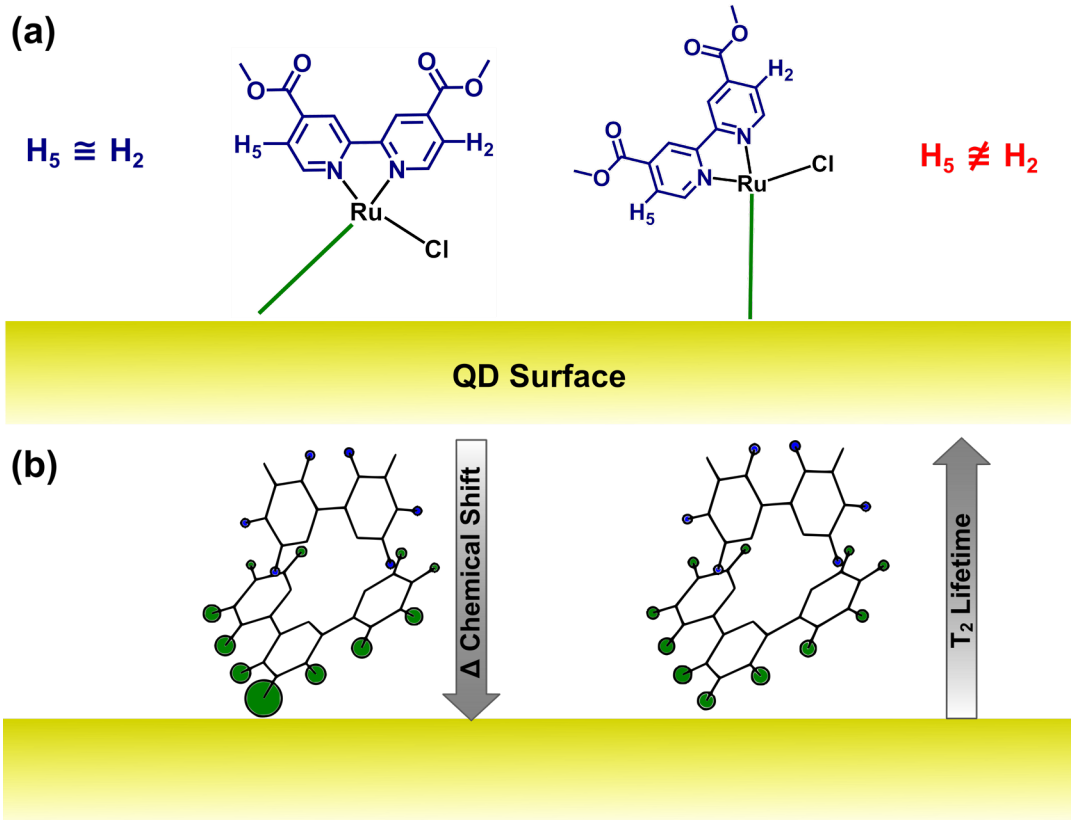

Figure 4.12 (a) Effect of WOC terpyridine and QD surface angle on the distance between dmcbpy protons and QD surface. The orientation shown on the left leads to an equal distance from the QD for both rings of the dmcbpy, while the orientation on the right places one side of the dmcbpy significantly closer to the surface. (b) Visualization of ΔCS and T_2^{-1} of protons in the WOC. Proton radius indicates the magnitude of ΔCS or T_2^{-1}. The catalyst is oriented to provide uniform trends in both quantities with distance from the nanocrystal surface. Proton coordinates are based on a related catalyst.[38]

Having determined the preferred orientation of the WOC we now revisit the surface interactions which could lead to such an orientation. In prior reports about ruthenium complexes binding to the surface of QDs it was thought that that ester or acid functionalities assisted binding to the QD surface through coordination to unpassivated surface Cd.[35, 70] Our system demonstrates the opposite orientation, with esters rotating to interact with the solvent rather than the surface. Although the polarity of the esters may play a role in orienting the WOC, they are clearly not involved through coordination to surface sites.

The orientation of the WOC does appear to bring the both the chloro ligand and the terpyridine into close proximity with the WOC surface. The terpyridine is a fairly large non-polar group, which may be driven into the aliphatic part of the ligand layer by hydrophobic effects. Alternately, the chloro ligand could be forming a bridging interaction between the Ru and Cd-rich surface. The Cd-Cl bond is known to be fairly stable as CdSe QDs have been produced with Cl^- surface ligands.[125] The orientation shown in Figure 4.12 has an ~120° angle between the Ru-Cl bond and z-axis, which is a feasible angle for bonding to a surface Cd site. Coordination between the QD surface and chloro ligand, must be transient or weakly bonded, as strong coordination would likely result in changes to the UV-visible spectra or the chemical shift of proton 1 upon binding. The orientation suggests that interactions exist between the QD surface and the WOC ligands, but the cause of the orientation cannot be definitively assigned to a single strong interaction.

We now consider the implications which the WOC orientation may have on charge transfer. In previous work, we hypothesized that fast hole transfer from photoexcited QD to this WOC required a source of electronic coupling between the QD valence band and WOC HOMO, possibly through the WOC ligand orbitals. The frontier molecular orbitals have been calculated for the related complex $[Ru(tpy)(bpy)Cl]^+$, where it was found that the HOMO of that complex is primarily located in a Ru d-orbital with some electron density is transferred to the chloro ligand through π-backbonding.[96] Owing to its close proximity to the QD surface, the increased HOMO density on the chloride may act as a bridge, enabling faster hole transfer than would be possible directly from the QD to the metal center. This is consistent with our observations from Chapter 3 in which we saw strong binding and rapid hole transfer for two different WOCs, both with chloro ligands.

The Ru-Cl bond acting as a source of electronic coupling between the QD valence band and WOC HOMO would have negative implications for the potential applications of the system for water oxidation. The mechanism of water oxidation for this family of WOCs requires inner-sphere hole transfer to a bound water molecule[36] which typically replaces the chloride during catalysis. As water is not a strong π-donor, replacement of the chloro ligand with water would reduce the rate and efficiency of hole transfer which is also crucial for progress through the catalytic cycle. Should it be shown that having a chloro ligand is essential for hole transfer to occur limits the applications of this complex as an oxidative co-catalyst despite the rapid rate of hole transfer it achieves.

On the other hand, finding that such a favorable orientation can be achieved in this system with a minimal synthetic transformation suggests that many other complexes could serve as effective co-catalysts. Halogen ligands are synthetically simple to add to metal complexes, and selection of the halogen may provide interesting effects on the coupling to the nanocrystal. Successful WOCs have been demonstrated with tunable positions in the coordination sphere,[132] and catalytic activity has also been shown for a complex which retains an iodo ligand throughout the entire catalytic cycle.[126] By replacing this ligand with a chloride or other ligand capable of π-backbonding to the Ru center a WOC may be produced with strong hole transfer and water oxidation characteristics.

In conclusion, we have observed that the WOC binds to the QD surface with a preferential orientation. This orientation manifests itself through changes of the chemical shift of several protons on the catalyst as well as accelerated T_2 decay observed in NMR. This improved understanding of the WOC/QD binding suggests a source of electronic coupling between the two which enables the fast hole transfer observed in prior measurements. This information suggests

new ideas for the improvement of photoinduced hole transfer from QDs to surface bound WOCs towards the goal of a successful water oxidation photocatalyst.

Chapter 5 Conclusions and Outlook

Chapter 2 demonstrated rapid hole transfer from CdS QDs to surface bound WOCs. Through a combination of optical spectroscopies and modelling we found that the catalyst interacted with the QD surface and received holes from the nanocrystal with a rate constant of 1.3 x 10^{11} s^{-1} per catalyst bound. At a 1:1 ratio of WOC to QD, hole trapping strongly outcompetes hole transfer, but higher ratios allow transfer to occur with similar efficiency to trapping. Although the system investigated is not optimal for catalysis the fast rate constant of hole transfer showed the potential for the system if hole trapping could be moderately reduced.

Chapter 3 investigated the mechanisms by which the system returns to the ground state following either picosecond hole trapping or transfer. After hole trapping, electron transfer occurs to the catalyst, quenching the trap emission and leading to a long-lived charge-separated state. This state recombines through diffusion-limited electron-hole recombination over the course of microseconds. Following hole transfer the oxidized WOC was found to decay through electron-hole recombination on a ten-nanosecond timescale. These results were supported through analysis of a related catalyst with unfavorable energetics for electron transfer. The finding that four orders of magnitude in time separating hole transfer and recombination is promising for eventual coupling of this system to sacrificial hole scavengers or reductive co-catalysts such as viologens or platinum particles.

Chapter 4 used NMR spectroscopy to elucidate the specifics of how the WOC interacts with the QD. Upon exposure to the QD, WOC protons experience changes in chemical environment and rotational correlation time consistent with binding to the QD surface. This binding occurs with a preferential orientation, bringing the terpyridine and chloro ligands of the

WOC close to the QD surface. This orientation suggests hole transfer through the chloro ligand as a mechanism for the strong coupling to the QD valence band. The design of future WOCs may utilize this information by placing a halogen in the coordination sphere where it will not obstruct the active site.

Taken together, these observations reveal principles for future design of water splitting systems. Preparing nanocrystals with reduced hole trapping rates will drastically improve initial charge transfer efficiency. Reductive co-catalysts with nanosecond electron transfer times will effectively prevent recombination of transferred charges. Selecting catalysts to favor coupling to the nanocrystal will facilitate hole transfer and improve turnover rates. The work presented here offers principles for both the analysis and design of future metal complex/nanocrystal water oxidation photocatalysts.

Chapter 6 Bibliography

(1) Cook, T. R.; Dogutan, D. K.; Reece, S. Y.; Surendranath, Y.; Teets, T. S.; Nocera, D. G., Solar Energy Supply and Storage for the Legacy and Nonlegacy Worlds. *Chem. Rev.* **2010,** *110*, 6474-6502.

(2) Allen, M.; Babiker, M.; Chen, Y.; Coninck, H. D.; Connors, S.; Diemen, R. v.; Dube, O. P.; Ebi, K. L.; Ebi, K.; Engelbrecht, F.; Ferrat, M.; Ford, J.; Forster, P.; Fuss, S.; Bolaños, T. G.; Harold, J.; Hoegh-Guldberg, O.; Hourcade, J.-C.; Huppmann, D.; Hayward, B.; Jacob, D.; Jiang, K.; Johansen, T. G.; Kainuma, M.; Kleijne, K. d.; Kriegler, E.; Ley, D.; Liverman, D.; Mahowald, N.; Masson-Delmotte, V.; Matthews, J. B. R.; Millar, R.; Mintenbeck, K.; Morelli, A.; Moufouma-Okia, W.; Mulugetta, Y.; Mundaca, L.; Nicoali, M.; Okereke, C.; Pathak, M.; Payne, A.; Pidcock, R.; Pirani, A.; Poloczanska, E.; Hans-OttoPörtner; Revi, A.; Riahi, K.; Roberts, D. C.; Roy, J.; Seneviratne, S. I.; R.Shukla, P.; Skea, J.; Slade, R.; Shindell, D.; Singh, C.; Solecki, W.; Steg, L.; Taylor, M.; Tschakert, P.; Waisman, H.; Warren, R.; Zhai, P.; Zickfeld, K. *IPCC, 2018: Summary for Policymakers.*; IPCC: World Meteorological Organization, 2018; pp 1-32.

(3) Lewis, N. S., Toward Cost-Effective Solar Energy Use. *Science* **2007,** *315*, 798.

(4) Styring, S., Artificial Photosynthesis for Solar Fuels. *Faraday Discuss.* **2012,** *155*, 357-376.

(5) Brown, K. A.; Harris, D. F.; Wilker, M. B.; Rasmussen, A.; Khadka, N.; Hamby, H.; Keable, S.; Dukovic, G.; Peters, J. W.; Seefeldt, L. C., Light-Driven Dinitrogen Reduction Catalyzed by a CdS: Nitrogenase MoFe Protein Biohybrid. *Science* **2016,** *352*, 448-450.

(6) Kim, D.; Sakimoto, K. K.; Hong, D.; Yang, P., Artificial Photosynthesis for Sustainable Fuel and Chemical Production. *Angew. Chem. Int. Ed.* **2015,** *54*, 3259-3266.

(7) Wilker, M. B.; Schnitzenbaumer, K. J.; Dukovic, G., Recent Progress in Photocatalysis Mediated by Colloidal II-VI Nanocrystals. *Isr. J. Chem.* **2012,** *52*, 1002-1015.

(8) Yano, J.; Kern, J.; Sauer, K.; Latimer, M. J.; Pushkar, Y.; Biesiadka, J.; Loll, B.; Saenger, W.; Messinger, J.; Zouni, A.; Yachandra, V. K., Where Water Is Oxidized to Dioxygen: Structure of the Photosynthetic Mn_4Ca Cluster. *Science* **2006,** *314*, 821.

(9) Eisenberg, R.; Gray, H. B., Preface on Making Oxygen. *Inorg. Chem.* **2008,** *47*, 1697-1699.

(10) Cady, C. W.; Crabtree, R. H.; Brudvig, G. W., Functional Models for the Oxygen-Evolving Complex of Photosystem II. *Coord. Chem. Rev.* **2008,** *252*, 444-455.

(11) Tseng, H.-W.; Zong, R.; Muckerman, J. T.; Thummel, R., Mononuclear Ruthenium(II) Complexes that Catalyze Water Oxidation. *Inorg. Chem.* **2008,** *47*, 11763-11773.

(12) Hetterscheid, D. G. H.; Reek, J. N. H., Mononuclear Water Oxidation Catalysts. *Angew. Chem. Int. Ed.* **2012,** *51*, 9740-9747.

(13) Duan, L.; Bozoglian, F.; Mandal, S.; Stewart, B.; Privalov, T.; Llobet, A.; Sun, L., A Molecular Ruthenium Catalyst with Water-Oxidation Activity Comparable to that of Photosystem II. *Nat. Chem.* **2012,** *4*, 418.

(14) Pokhrel, R.; Goetz, M. K.; Shaner, S. E.; Wu, X.; Stahl, S. S., The "Best Catalyst" for Water Oxidation Depends on the Oxidation Method Employed: A Case Study of Manganese Oxides. *J. Am. Chem. Soc.* **2015,** *137*, 8384-8387.

(15) Yu, Z.; Li, F.; Sun, L., Recent advances in dye-sensitized photoelectrochemical cells for solar hydrogen production based on molecular components. *Energy & Environmental Science* **2015,** *8*, 760-775.
(16) Brus, L. E., A Simple Model for the Ionization Potential, Electron Affinity, and Aqueous Redox Potentials of Small Semiconductor Crystallites. *J. Chem. Phys.* **1983,** *79*, 5566-5571.
(17) Kuno, M., Introductory Nanoscience: Physical and Chemical Concepts, Garland Science. Taylor & Francis Group, New York: 2012.
(18) Kippeny, T.; Swafford, L. A.; Rosenthal, S. J., Semiconductor Nanocrystals: A Powerful Visual Aid for Introducing the Particle in a Box. *J. Chem. Educ.* **2002,** *79*, 1094.
(19) Weiss, E. A., Designing the Surfaces of Semiconductor Quantum Dots for Colloidal Photocatalysis. *ACS Energy Lett.* **2017,** *2*, 1005-1013.
(20) Walter, M. G.; Warren, E. L.; McKone, J. R.; Boettcher, S. W.; Mi, Q.; Santori, E. A.; Lewis, N. S., Solar Water Splitting Cells. *Chem. Rev.* **2010,** *110*, 6446-6473.
(21) Meissner, D.; Memming, R.; Kastening, B.; Bahnemann, D., Fundamental Problems of Water Splitting at Cadmium Sulfide. *Chem. Phys. Lett.* **1986,** *127*, 419-423.
(22) Bard, A. J.; Faulkner, L. R.; Leddy, J.; Zoski, C. G., *Electrochemical Methods: Fundamentals and Applications*. 3rd ed.; Wiley New York: 1980; Vol. 2.
(23) Amirav, L.; Alivisatos, A. P., Photocatalytic Hydrogen Production with Tunable Nanorod Heterostructures. *J. Phys. Chem. Lett.* **2010,** *1*, 1051-1054.
(24) Gimbert-Suriñach, C.; Albero, J.; Stoll, T.; Fortage, J. r. m.; Collomb, M.-N. l.; Deronzier, A.; Palomares, E.; Llobet, A., Efficient and Limiting Reactions in Aqueous Light-Induced Hydrogen Evolution Systems using Molecular Catalysts and Quantum Dots. *J. Am. Chem. Soc.* **2014,** *136*, 7655-7661.
(25) Han, Z.; Qiu, F.; Eisenberg, R.; Holland, P. L.; Krauss, T. D., Robust Photogeneration of H_2 in Water Using Semiconductor Nanocrystals and a Nickel Catalyst. *Science* **2012,** *338*, 1321.
(26) Brown, K. A.; Wilker, M. B.; Boehm, M.; Dukovic, G.; King, P. W., Characterization of Photochemical Processes for H2 Production by CdS Nanorod–[FeFe] Hydrogenase Complexes. *J. Am. Chem. Soc.* **2012,** *134*, 5627-5636.
(27) Brown, K. A.; Dayal, S.; Ai, X.; Rumbles, G.; King, P. W., Controlled Assembly of Hydrogenase-CdTe Nanocrystal Hybrids for Solar Hydrogen Production. *J. Am. Chem. Soc.* **2010,** *132*, 9672-9680.
(28) Burai, T. N.; Panay, A. J.; Zhu, H.; Lian, T.; Lutz, S., Light-Driven, Quantum Dot-Mediated Regeneration of FMN To Drive Reduction of Ketoisophorone by Old Yellow Enzyme. *ACS Catal.* **2012,** *2*, 667-670.
(29) Chaudhary, Y. S.; Woolerton, T. W.; Allen, C. S.; Warner, J. H.; Pierce, E.; Ragsdale, S. W.; Armstrong, F. A., Visible Light-Driven CO_2 Reduction by Enzyme Coupled CdS Nanocrystals. *Chem. Commun. (Cambridge, U. K.)* **2012,** *48*, 58-60.
(30) Greene, B. L.; Joseph, C. A.; Maroney, M. J.; Dyer, R. B., Direct Evidence of Active-Site Reduction and Photodriven Catalysis in Sensitized Hydrogenase Assemblies. *J. Am. Chem. Soc.* **2012,** *134*, 11108-11111.
(31) Brown, K. A.; Wilker, M. B.; Boehm, M.; Hamby, H.; Dukovic, G.; King, P. W., Photocatalytic Regeneration of Nicotinamide Cofactors by Quantum Dot–Enzyme Biohybrid Complexes. *ACS Catal.* **2016,** *6*, 2201-2204.

(32) Yehezkeli, O.; de Oliveira, D. R.; Cha, J. N., Electrostatically Assembled CdS–Co3O4 Nanostructures for Photo-assisted Water Oxidation and Photocatalytic Reduction of Dye Molecules. *Small* **2015,** *11*, 668-674.
(33) Wolff, C. M.; Frischmann, P. D.; Schulze, M.; Bohn, B. J.; Wein, R.; Livadas, P.; Carlson, M. T.; Jäckel, F.; Feldmann, J.; Würthner, F.; Stolarczyk, J. K., All-in-One Visible-Light-Driven Water Splitting by Combining Nanoparticulate and Molecular Co-Catalysts on CdS Nanorods. *Nat. Energy* **2018,** *3*, 862-869.
(34) Dimitrijevic, N. M.; Li, S.; Grätzel, M., Visible Light-Induced Oxygen Evolution in Aqueous Cadmium Sulfide Suspensions. *J. Am. Chem. Soc.* **1984,** *106*, 6565-6569.
(35) Tseng, H.-W.; Wilker, M. B.; Damrauer, N. H.; Dukovic, G., Charge Transfer Dynamics between Photoexcited CdS Nanorods and Mononuclear Ru Water-Oxidation Catalysts. *J. Am. Chem. Soc.* **2013,** *135*, 3383-3386.
(36) Concepcion, J. J.; Tsai, M.-K.; Muckerman, J. T.; Meyer, T. J., Mechanism of Water Oxidation by Single-Site Ruthenium Complex Catalysts. *J. Am. Chem. Soc.* **2010,** *132*, 1545-1557.
(37) Masaoka, S.; Sakai, K., Clear Evidence Showing the Robustness of a Highly Active Oxygen-evolving Mononuclear Ruthenium Complex with an Aqua Ligand. *Chem. Lett.* **2009,** *38*, 182-183.
(38) Pushkar, Y.; Moonshiram, D.; Purohit, V.; Yan, L.; Alperovich, I., Spectroscopic Analysis of Catalytic Water Oxidation by $[Ru^{II}(bpy)(tpy)H_2O]^{2+}$ Suggests That RuV═O Is Not a Rate-Limiting Intermediate. *J. Am. Chem. Soc.* **2014,** *136*, 11938-11945.
(39) Klimov, V. I., Spectral and Dynamical Properties of Multiexcitons in Semiconductor Nanocrystals. *Annu. Rev. Phys. Chem.* **2007,** *58*, 635-673.
(40) Klimov, V.; Bolivar, P. H.; Kurz, H., Ultrafast Carrier Dynamics in Semiconductor Quantum Dots. *Phys. Rev. B* **1996,** *53*, 1463-1467.
(41) Pearce, O. M.; Duncan, J. S.; Damrauer, N. H.; Dukovic, G., Ultrafast Hole Transfer from CdS Quantum Dots to a Water Oxidation Catalyst. *J. Phys. Chem. C* **2018,** *122*, 17559-17565.
(42) Kuehnel, M. F.; Orchard, K. L.; Dalle, K. E.; Reisner, E., Selective Photocatalytic CO_2 Reduction in Water Through Anchoring of a Molecular Ni Catalyst on CdS Nanocrystals. *J. Am. Chem. Soc.* **2017,** *139*, 7217-7223.
(43) Xu, Y.; Chen, R.; Li, Z.; Li, A.; Han, H.; Li, C., Influence of the Electrostatic Interaction between a Molecular Catalyst and Semiconductor on Photocatalytic Hydrogen Evolution Activity in Cobaloxime/CdS Hybrid Systems. *ACS Appl. Mater. Interfaces* **2017,** *9*, 23230-23237.
(44) Wilker, M. B.; Shinopoulos, K. E.; Brown, K. A.; Mulder, D. W.; King, P. W.; Dukovic, G., Electron Transfer Kinetics in CdS Nanorod–[FeFe]-Hydrogenase Complexes and Implications for Photochemical H_2 Generation. *J. Am. Chem. Soc.* **2014,** *136*, 4316-4324.
(45) Wu, K.; Chen, Z.; Lv, H.; Zhu, H.; Hill, C. L.; Lian, T., Hole Removal Rate Limits Photodriven H_2 Generation Efficiency in CdS-Pt and CdSe/CdS-Pt Semiconductor Nanorod–Metal Tip Heterostructures. *J. Am. Chem. Soc.* **2014,** *136*, 7708-7716.
(46) Jensen, S. C.; Bettis Homan, S.; Weiss, E. A., Photocatalytic Conversion of Nitrobenzene to Aniline through Sequential Proton-Coupled One-Electron Transfers from a Cadmium Sulfide Quantum Dot. *J. Am. Chem. Soc.* **2016,** *138*, 1591-1600.

(47) Utterback, J. K.; Wilker, M. B.; Brown, K. A.; King, P. W.; Eaves, J. D.; Dukovic, G., Competition Between Electron Transfer, Trapping, and Recombination in CdS Nanorod-Hydrogenase Complexes. *Phys. Chem. Chem. Phys.* **2015,** *17*, 5538-5542.
(48) Berr, M. J.; Wagner, P.; Fischbach, S.; Vaneski, A.; Schneider, J.; Susha, A. S.; Rogach, A. L.; Jäckel, F.; Feldmann, J., Hole Scavenger Redox Potentials Determine Quantum Efficiency and Stability of Pt-Decorated CdS Nanorods for Photocatalytic Hydrogen Generation. *Appl. Phys. Lett.* **2012,** *100*, 223903.
(49) Kamat, P. V.; Tvrdy, K.; Baker, D. R.; Radich, J. G., Beyond Photovoltaics: Semiconductor Nanoarchitectures for Liquid-Junction Solar Cells. *Chem. Rev.* **2010,** *110*, 6664-6688.
(50) Simon, T.; Bouchonville, N.; Berr, M. J.; Vaneski, A.; Adrović, A.; Volbers, D.; Wyrwich, R.; Döblinger, M.; Susha, A. S.; Rogach, A. L.; Jäckel, F.; Stolarczyk, J. K.; Feldmann, J., Redox Shuttle Mechanism Enhances Photocatalytic H_2 Generation on Ni-Decorated CdS Nanorods. *Nat. Mater.* **2014,** *13*, 1013.
(51) Ding, T. X.; Olshansky, J. H.; Leone, S. R.; Alivisatos, A. P., Efficiency of Hole Transfer from Photoexcited Quantum Dots to Covalently Linked Molecular Species. *J. Am. Chem. Soc.* **2015,** *137*, 2021-2029.
(52) Knowles, K. E.; Peterson, M. D.; McPhail, M. R.; Weiss, E. A., Exciton Dissociation within Quantum Dot–Organic Complexes: Mechanisms, Use as a Probe of Interfacial Structure, and Applications. *J. Phys. Chem. C* **2013,** *117*, 10229-10243.
(53) Osterloh, F. E., Inorganic Nanostructures for Photoelectrochemical and Photocatalytic Water Splitting. *Chem. Soc. Rev.* **2013,** *42*, 2294-2320.
(54) Klimov, V. I., Optical Nonlinearities and Ultrafast Carrier Dynamics in Semiconductor Nanocrystals. *J. Phys. Chem. B* **2000,** *104*, 6112-6123.
(55) Peterson, M. D.; Cass, L. C.; Harris, R. D.; Edme, K.; Sung, K.; Weiss, E. A., The Role of Ligands in Determining the Exciton Relaxation Dynamics in Semiconductor Quantum Dots. *Annu. Rev. Phys. Chem.* **2014,** *65*, 317-339.
(56) Wu, K.; Du, Y.; Tang, H.; Chen, Z.; Lian, T., Efficient Extraction of Trapped Holes from Colloidal CdS Nanorods. *J. Am. Chem. Soc.* **2015,** *137*, 10224-10230.
(57) Utterback, J. K.; Grennell, A. N.; Wilker, M. B.; Pearce, O. M.; Eaves, J. D.; Dukovic, G., Observation of Trapped-Hole Diffusion on the Surfaces of CdS Nanorods. *Nat. Chem.* **2016**.
(58) Weinberg, D. R.; Gagliardi, C. J.; Hull, J. F.; Murphy, C. F.; Kent, C. A.; Westlake, B. C.; Paul, A.; Ess, D. H.; McCafferty, D. G.; Meyer, T. J., Proton-Coupled Electron Transfer. *Chem. Rev.* **2012,** *112*, 4016-4093.
(59) Kanan, M. W.; Nocera, D. G., In Situ Formation of an Oxygen-Evolving Catalyst in Neutral Water Containing Phosphate and Co^{2+}. *Science* **2008,** *321*, 1072-1075.
(60) Herlihy, D. M.; Waegele, M. M.; Chen, X.; Pemmaraju, C.; Prendergast, D.; Cuk, T., Detecting the Oxyl Radical of Photocatalytic Water Oxidation at an n-$SrTiO_3$/Aqueous Interface Through its Subsurface Vibration. *Nat. Chem.* **2016,** *8*, 549.
(61) McArthur, E. A.; Morris-Cohen, A. J.; Knowles, K. E.; Weiss, E. A., Charge Carrier Resolved Relaxation of the First Excitonic State in CdSe Quantum Dots Probed with Near-Infrared Transient Absorption Spectroscopy. *J. Phys. Chem. B* **2010,** *114*, 14514-14520.
(62) Peterson, M. D.; Jensen, S. C.; Weinberg, D. J.; Weiss, E. A., Mechanisms for Adsorption of Methyl Viologen on CdS Quantum Dots. *ACS Nano* **2014,** *8*, 2826-2837.

(63) Yu, W. W.; Qu, L.; Guo, W.; Peng, X., Experimental Determination of the Extinction Coefficient of CdTe, CdSe, and CdS Nanocrystals. *Chem. Mater.* **2003,** *15*, 2854-2860.
(64) Rurack, K.; Spieles, M., Fluorescence Quantum Yields of a Series of Red and Near-Infrared Dyes Emitting at 600−1000 nm. *Anal. Chem.* **2011,** *83*, 1232-1242.
(65) Kovalenko, S. A.; Dobryakov, A. L.; Ruthmann, J.; Ernsting, N. P., Femtosecond Spectroscopy of Condensed Phases with Chirped Supercontinuum Probing. *Phys. Rev. A* **1999,** *59*, 2369-2384.
(66) Schnitzenbaumer, K. J.; Labrador, T.; Dukovic, G., Impact of Chalcogenide Ligands on Excited State Dynamics in CdSe Quantum Dots. *J. Phys. Chem. C* **2015,** *119*, 13314-13324.
(67) Klimov, V. I.; Schwarz, C. J.; McBranch, D. W.; Leatherdale, C. A.; Bawendi, M. G., Ultrafast Dynamics of Inter- and Intraband Transitions in Semiconductor Nanocrystals: Implications For Quantum-Dot Lasers. *Phys. Rev. B* **1999,** *60*, R2177-R2180.
(68) Garrett, M. D.; Dukes III, A. D.; McBride, J. R.; Smith, N. J.; Pennycook, S. J.; Rosenthal, S. J., Band Edge Recombination in CdSe, CdS and CdS_xSe_{1-x} Alloy Nanocrystals Observed by Ultrafast Fluorescence Upconversion: The Effect of Surface Trap States. *J. Phys. Chem. C* **2008,** *112*, 12736-12746.
(69) Underwood, D. F.; Kippeny, T.; Rosenthal, S. J., Ultrafast Carrier Dynamics in CdSe Nanocrystals Determined by Femtosecond Fluorescence Upconversion Spectroscopy. *J. Phys. Chem. B* **2001,** *105*, 436-443.
(70) Sykora, M.; Petruska, M. A.; Alstrum-Acevedo, J.; Bezel, I.; Meyer, T. J.; Klimov, V. I., Photoinduced Charge Transfer between CdSe Nanocrystal Quantum Dots and Ru−Polypyridine Complexes. *J. Am. Chem. Soc.* **2006,** *128*, 9984-9985.
(71) Grennell, A. N.; Utterback, J. K.; Pearce, O. M.; Wilker, M. B.; Dukovic, G., Relationships between Exciton Dissociation and Slow Recombination within ZnSe/CdS and CdSe/CdS Dot-in-Rod Heterostructures. *Nano Lett.* **2017**.
(72) Lian, S.; Weinberg, D. J.; Harris, R. D.; Kodaimati, M. S.; Weiss, E. A., Subpicosecond Photoinduced Hole Transfer from a CdS Quantum Dot to a Molecular Acceptor Bound Through an Exciton-Delocalizing Ligand. *ACS Nano* **2016,** *10*, 6372-6382.
(73) Yang, B.; Schneeloch, J. E.; Pan, Z.; Furis, M.; Achermann, M., Radiative Lifetimes and Orbital Symmetry of Electronic Energy Levels of CdS Nanocrystals: Size Dependence. *Phys. Rev. B* **2010,** *81*, 073401.
(74) Press, W. H., *Numerical Recipes 3rd Edition: The Art of Scientific Computing*. Cambridge University Press: 2007.
(75) Morris-Cohen, A. J.; Frederick, M. T.; Cass, L. C.; Weiss, E. A., Simultaneous Determination of the Adsorption Constant and the Photoinduced Electron Transfer Rate for a CdS Quantum Dot–Viologen Complex. *J. Am. Chem. Soc.* **2011,** *133*, 10146-10154.
(76) Munro, A. M.; Jen-La Plante, I.; Ng, M. S.; Ginger, D. S., Quantitative Study of the Effects of Surface Ligand Concentration on CdSe Nanocrystal Photoluminescence. *J. Phys. Chem. C* **2007,** *111*, 6220-6227.
(77) Uematsu, T.; Shimomura, E.; Torimoto, T.; Kuwabata, S., Evaluation of Surface Ligands on Semiconductor Nanoparticle Surfaces Using Electron Transfer to Redox Species. *J. Phys. Chem. C* **2016,** *120*, 16012-16023.
(78) Sadhu, S.; Tachiya, M.; Patra, A., A Stochastic Model for Energy Transfer from CdS Quantum Dots/Rods (Donors) to Nile Red Dye (Acceptors). *J. Phys. Chem. C* **2009,** *113*, 19488-19492.

(79) Morris-Cohen, A. J.; Vasilenko, V.; Amin, V. A.; Reuter, M. G.; Weiss, E. A., Model for Adsorption of Ligands to Colloidal Quantum Dots with Concentration-Dependent Surface Structure. *ACS Nano* **2011,** *6*, 557-565.
(80) Ashford, D. L.; Brennaman, M. K.; Brown, R. J.; Keinan, S.; Concepcion, J. J.; Papanikolas, J. M.; Templeton, J. L.; Meyer, T. J., Varying the Electronic Structure of Surface-Bound Ruthenium(II) Polypyridyl Complexes. *Inorg. Chem.* **2014,** *54*, 460-469.
(81) Huang, J.; Huang, Z.; Jin, S.; Lian, T., Exciton Dissociation in CdSe Quantum Dots by Hole Transfer to Phenothiazine. *J. Phys. Chem. C* **2008,** *112*, 19734-19738.
(82) Koole, R.; Schapotschnikow, P.; de Mello Donegá, C.; Vlugt, T. J.; Meijerink, A., Time-Dependent Photoluminescence Spectroscopy as a Tool to Measure the Ligand Exchange Kinetics on a Quantum Dot Surface. *ACS Nano* **2008,** *2*, 1703-1714.
(83) Gao, Y.; Peng, X., Photogenerated Excitons in Plain Core CdSe Nanocrystals with Unity Radiative Decay in Single Channel: The Effects of Surface and Ligands. *J. Am. Chem. Soc.* **2015,** *137*, 4230-4235.
(84) Steckel, J. S.; Zimmer, J. P.; Coe-Sullivan, S.; Stott, N. E.; Bulović, V.; Bawendi, M. G., Blue Luminescence from (CdS) ZnS Core–Shell Nanocrystals. *Angew. Chem. Int. Ed.* **2004,** *43*, 2154-2158.
(85) Chen, D.; Zhao, F.; Qi, H.; Rutherford, M.; Peng, X., Bright and Stable Purple/Blue Emitting CdS/ZnS Core/Shell Nanocrystals Grown by Thermal Cycling Using a Single-Source Precursor. *Chem. Mater.* **2010,** *22*, 1437-1444.
(86) Zhu, H.; Song, N.; Lian, T., Wave Function Engineering for Ultrafast Charge Separation and Slow Charge Recombination in Type II Core/Shell Quantum Dots. *J. Am. Chem. Soc.* **2011,** *133*, 8762-8771.
(87) Wilker, M. B.; Utterback, J. K.; Greene, S.; Brown, K. A.; Mulder, D. W.; King, P. W.; Dukovic, G., Role of Surface-Capping Ligands in Photoexcited Electron Transfer between CdS Nanorods and [FeFe] Hydrogenase and the Subsequent H2 Generation. *J. Phys. Chem. C* **2018,** *122*, 741-750.
(88) He, C.; Weinberg, D. J.; Nepomnyashchii, A. B.; Lian, S.; Weiss, E. A., Control of the Redox Activity of PbS Quantum Dots by Tuning Electrostatic Interactions at the Quantum Dot/Solvent Interface. *J. Am. Chem. Soc.* **2016,** *138*, 8847-8854.
(89) Kalisman, P.; Kauffmann, Y.; Amirav, L., Photochemical Oxidation on Nanorod Photocatalysts. *J. Mater. Chem. A* **2015,** *3*, 3261-3265.
(90) Caspar, J. V.; Meyer, T. J., Photochemistry of tris(2,2'-bipyridine)ruthenium(2+) ion ($Ru(bpy)_3^{2+}$). Solvent effects. *J. Am. Chem. Soc.* **1983,** *105*, 5583-5590.
(91) Hewitt, J. T.; Vallett, P. J.; Damrauer, N. H., Dynamics of the ^{3}MLCT in Ru(II) Terpyridyl Complexes Probed by Ultrafast Spectroscopy: Evidence of Excited-State Equilibration and Interligand Electron Transfer. *J. Phys. Chem. A* **2012,** *116*, 11536-11547.
(92) Pavlishchuk, V. V.; Addison, A. W., Conversion Constants for Redox Potentials Measured Versus Different Reference Electrodes in Acetonitrile Solutions At 25°C. *Inorg. Chim. Acta* **2000,** *298*, 97-102.
(93) Wasylenko, D. J.; Ganesamoorthy, C.; Koivisto, B. D.; Henderson, M. A.; Berlinguette, C. P., Insight into Water Oxidation by Mononuclear Polypyridyl Ru Catalysts. *Inorg. Chem.* **2010,** *49*, 2202-2209.
(94) Woodall, D. L.; Tobias, A. K.; Jones, M., Resolving Carrier Recombination in Cds Quantum Dots: A Time-Resolved Fluorescence Study. *Chem. Phys.* **2016,** *471*, 2-10.

(95) Haase, M.; Weller, H.; Henglein, A., Photochemistry of Colloidal Semiconductors. 26. Photoelectron Emission from Cadmium Sulfide Particles and Related Chemical Effects. *J. Phys. Chem.* **1988,** *92*, 4706-4712.
(96) Jakubikova, E.; Chen, W.; Dattelbaum, D. M.; Rein, F. N.; Rocha, R. C.; Martin, R. L.; Batista, E. R., Electronic Structure and Spectroscopy of $[Ru(tpy)_2]^{2+}$, $[Ru(tpy)(bpy)(H_2O)]^{2+}$, and $[Ru(tpy)(bpy)(Cl)]^{+}$. *Inorg. Chem.* **2009,** *48*, 10720-10725.
(97) Tachiya, M., Kinetics of Quenching of Luminescent Probes in Micellar Systems. II. *J. Chem. Phys.* **1982,** *76*, 340-348.
(98) Eychmüller, A.; Hässelbarth, A.; Katsikas, L.; Weller, H., Photochemistry of Semiconductor Colloids. 36. Fluorescence Investigations on the Nature of Electron and Hole Traps in Q-Sized Colloidal CdS Particles. *Ber. Bunsen-Ges.* **1991,** *95*, 79-84.
(99) Berberan-Santos, M. N.; Bodunov, E. N.; Valeur, B., Mathematical Functions for the Analysis of Luminescence Decays with Underlying Distributions 1. Kohlrausch Decay Function (Stretched Exponential). *Chem. Phys.* **2005,** *315*, 171-182.
(100) Utterback, J. K.; Hamby, H.; Pearce, O. M.; Eaves, J. D.; Dukovic, G., Trapped-Hole Diffusion in Photoexcited CdSe Nanorods. *J. Phys. Chem. C* **2018,** *122*, 16974-16982.
(101) Knowles, K. E.; McArthur, E. A.; Weiss, E. A., A Multi-Timescale Map of Radiative and Nonradiative Decay Pathways for Excitons in CdSe Quantum Dots. *ACS Nano* **2011,** *5*, 2026-2035.
(102) Mooney, J.; Krause, M. M.; Saari, J. I.; Kambhampati, P., Challenge to the Deep-Trap Model of the Surface in Semiconductor Nanocrystals. *Phys. Rev. B* **2013,** *87*, 081201.
(103) Jones, M.; Lo, S. S.; Scholes, G. D., Quantitative Modeling of the Role Of Surface Traps in Cdse/Cds/Zns Nanocrystal Photoluminescence Decay Dynamics. *Proc. Natl. Acad. Sci. U. S. A.* **2009,** *106*, 3011-3016.
(104) Palato, S.; Seiler, H.; McGovern, L.; Mack, T. G.; Jethi, L.; Kambhampati, P., Electron Dynamics at the Surface of Semiconductor Nanocrystals. *J. Phys. Chem. C* **2017,** *121*, 26519-26527.
(105) Mack, T. G.; Jethi, L.; Kambhampati, P., Temperature Dependence of Emission Line Widths from Semiconductor Nanocrystals Reveals Vibronic Contributions to Line Broadening Processes. *J. Phys. Chem. C* **2017,** *121*, 28537-28545.
(106) Veamatahau, A.; Jiang, B.; Seifert, T.; Makuta, S.; Latham, K.; Kanehara, M.; Teranishi, T.; Tachibana, Y., Origin of Surface Trap States in CdS Quantum Dots: Relationship Between Size Dependent Photoluminescence and Sulfur Vacancy Trap States. *Phys. Chem. Chem. Phys.* **2015,** *17*, 2850-2858.
(107) O'Neil, M.; Marohn, J.; McLendon, G., Picosecond Measurements of Exciton Trapping in Semiconductor Clusters. *Chem. Phys. Lett.* **1990,** *168*, 208-210.
(108) Hewitt, J. T.; Concepcion, J. J.; Damrauer, N. H., Inverse Kinetic Isotope Effect in the Excited-State Relaxation of a Ru(II)–Aquo Complex: Revealing the Impact of Hydrogen-Bond Dynamics on Nonradiative Decay. *J. Am. Chem. Soc.* **2013,** *135*, 12500-12503.
(109) Wasylenko, D. J.; Ganesamoorthy, C.; Henderson, M. A.; Koivisto, B. D.; Osthoff, H. D.; Berlinguette, C. P., Electronic Modification of the $[Ru^{II}(tpy)(bpy)(OH_2)]^{2+}$ Scaffold: Effects on Catalytic Water Oxidation. *J. Am. Chem. Soc.* **2010,** *132*, 16094-16106.
(110) Wu, K.; Zhu, H.; Liu, Z.; Rodríguez-Córdoba, W.; Lian, T., Ultrafast Charge Separation and Long-Lived Charge Separated State in Photocatalytic CdS–Pt Nanorod Heterostructures. *J. Am. Chem. Soc.* **2012,** *134*, 10337-10340.

(111) Connelly, N. G.; Geiger, W. E., Chemical Redox Agents for Organometallic Chemistry. *Chem. Rev.* **1996,** *96*, 877-910.
(112) Kilina, S.; Cui, P.; Fischer, S. A.; Tretiak, S., Conditions for Directional Charge Transfer in CdSe Quantum Dots Functionalized by Ru(II) Polypyridine Complexes. *J. Phys. Chem. Lett.* **2014,** *5*, 3565-3576.
(113) Beauvilliers, E. E.; Meyer, G. J., Evidence for Cation-Controlled Excited-State Localization in a Ruthenium Polypyridyl Compound. *Inorg. Chem.* **2016,** *55*, 7517-7526.
(114) Anderson, N. C.; Hendricks, M. P.; Choi, J. J.; Owen, J. S., Ligand Exchange and the Stoichiometry of Metal Chalcogenide Nanocrystals: Spectroscopic Observation of Facile Metal-Carboxylate Displacement and Binding. *J. Am. Chem. Soc.* **2013,** *135*, 18536-18548.
(115) Cline, R. P.; Utterback, J. K.; Strong, S. E.; Dukovic, G.; Eaves, J. D., On the Nature of Trapped-Hole States in CdS Nanocrystals and the Mechanism of Their Diffusion. *J. Phys. Chem. Lett.* **2018,** *9*, 3532-3537.
(116) Redner, S., *A Guide to First-Passage Processes*. Cambridge University Press: 2001.
(117) Liu, C.; Qiu, F.; Peterson, J. J.; Krauss, T. D., Aqueous Photogeneration of H_2 with CdSe Nanocrystals and Nickel Catalysts: Electron Transfer Dynamics. *J. Phys. Chem. B* **2015,** *119*, 7349-7357.
(118) Ye, Y.; Wang, X.; Ye, S.; Xu, Y.; Feng, Z.; Li, C., Charge-Transfer Dynamics Promoted by Hole Trap States in CdSe Quantum Dots–Ni^{2+} Photocatalytic System. *J. Phys. Chem. C* **2017,** *121*, 17112-17120.
(119) Wang, Y.; Suna, A.; McHugh, J.; Hilinski, E. F.; Lucas, P. A.; Johnson, R. D., Optical Transient Bleaching of Quantum-Confined Cds Clusters: The Effects of Surface-Trapped Electron–Hole Pairs. *J. Chem. Phys.* **1990,** *92*, 6927-6939.
(120) Logunov, S.; Green, T.; Marguet, S.; El-Sayed, M. A., Interfacial Carriers Dynamics of CdS Nanoparticles. *J. Phys. Chem. A* **1998,** *102*, 5652-5658.
(121) Frederick, M. T.; Weiss, E. A., Relaxation of Exciton Confinement in CdSe Quantum Dots by Modification with a Conjugated Dithiocarbamate Ligand. *ACS Nano* **2010,** *4*, 3195-3200.
(122) Knowles, K. E.; Malicki, M.; Weiss, E. A., Dual-Time Scale Photoinduced Electron Transfer from PbS Quantum Dots to a Molecular Acceptor. *J. Am. Chem. Soc.* **2012,** *134*, 12470-12473.
(123) Hens, Z.; Martins, J. C., A Solution NMR Toolbox for Characterizing the Surface Chemistry of Colloidal Nanocrystals. *Chem. Mater.* **2013,** *25*, 1211-1221.
(124) Knauf, R. R.; Lennox, J. C.; Dempsey, J. L., Quantifying Ligand Exchange Reactions at CdSe Nanocrystal Surfaces. *Chem. Mater.* **2016,** *28*, 4762-4770.
(125) Anderson, N. C.; Owen, J. S., Soluble, Chloride-Terminated CdSe Nanocrystals: Ligand Exchange Monitored by ^{1}H and ^{31}P NMR Spectroscopy. *Chem. Mater.* **2013,** *25*, 69-76.
(126) Kaveevivitchai, N.; Zong, R.; Tseng, H.-W.; Chitta, R.; Thummel, R. P., Further Observations on Water Oxidation Catalyzed by Mononuclear Ru(II) Complexes. *Inorg. Chem.* **2012,** *51*, 2930-2939.
(127) Robert, M. S.; Francis, X. W.; David, J. K., *Spectrometric Identification of Organic Compounds*. 7th ed.; Wiley: 2005; p 106.
(128) Bloembergen, N.; Purcell, E. M.; Pound, R. V., Relaxation Effects in Nuclear Magnetic Resonance Absorption. *Phys. Rev.* **1948,** *73*, 679-712.

(129) Petrov, E. P.; Cichos, F.; Zenkevich, E.; Starukhin, D.; von Borczyskowski, C., Time Resolved Photoluminescence Anisotropy of CdSe/ZnS Nanoparticles in Toluene at 300 K. *Chem. Phys. Lett.* **2005,** *402*, 233-238.
(130) Carr, H. Y.; Purcell, E. M., Effects of Diffusion on Free Precession in Nuclear Magnetic Resonance Experiments. *Phys. Rev.* **1954,** *94*, 630-638.
(131) De Roo, J.; Yazdani, N.; Drijvers, E.; Lauria, A.; Maes, J.; Owen, J. S.; Van Driessche, I.; Niederberger, M.; Wood, V.; Martins, J. C., Probing Solvent–Ligand Interactions in Colloidal Nanocrystals by the NMR Line Broadening. *Chem. Mater.* **2018,** *30*, 5485-5492.
(132) Duan, L.; Araujo, C. M.; Ahlquist, M. S. G.; Sun, L., Highly Efficient and Robust Molecular Ruthenium Catalysts for Water Oxidation. *Proc. Natl. Acad. Sci. U. S. A.* **2012,** *109*, 15584-15588.